

**Sandra Pötz**

**HIGH CAPACITY ELECTRODES FOR LITHIUM-  
ION BATTERIES**

**Doctoral Thesis**

Submitted in fulfilment of requirements for the degree of  
Doctor of Technical Sciences  
at the

**Graz University of Technology**  
**Institute for Chemistry and Technology of Materials (ICTM)**

**In Cooperation with VARTA Micro Innovation GmbH**

This work has been carried out under the supervision of  
**Univ.-Prof. Dipl.-Ing. Dr. techn. Franz Stelzer**

**2014**

Deutsche Fassung:

Beschluss der Curricula-Kommission für Bachelor-, Master- und Diplomstudien vom 10.11.2008

Genehmigung des Senates am 1.12.2008

## EIDESSTATTLICHE ERKLÄRUNG

Ich erkläre an Eides statt, dass ich die vorliegende Arbeit selbstständig verfasst, andere als die angegebenen Quellen/Hilfsmittel nicht benutzt, und die den benutzten Quellen wörtlich und inhaltlich entnommenen Stellen als solche kenntlich gemacht habe.

Graz, am ..... (Unterschrift)

Englische Fassung:

## STATUTORY DECLARATION

I declare that I have authored this thesis independently, that I have not used other than the declared sources / resources, and that I have explicitly marked all material which has been quoted either literally or by content from the used sources.

.....  
date

.....  
(signature)

## ACKNOWLEDGEMENT

I would like to express my utmost gratitude to my supervisor, Prof. Dipl.-Ing. Dr. techn. Franz Stelzer, head of the Institute for Chemistry and Technology of Materials, for giving me the opportunity to perform this PhD thesis under his guidance.

Furthermore I'd like to express my greatest appreciation to my financial supporter, the company VARTA Micro Innovation GmbH and Dr. Stefan Koller, the CEO of the company for his guidance, his encouragement to pursue my investigations and for offering all research facilities to carry out this doctoral thesis. In this context I owe my deepest gratitude to Dr. Bernd Fuchsbichler, my project manager, for the fruitful discussions during the last three years and for his support the whole way of my thesis.

My warmest gratitude is dedicated to all of my colleagues for their continuous optimism, encouragement and support during this study. I'd like to start with my office mates Dr. Michaela Scharfegger, Stephania Toulis and Christian Baumann for giving me useful and constructive advices and helping me during this thesis. I would like to extend my thanks to Dipl.-Ing. Patricia Handel, Dipl.-Ing. Katharina Gruber, Katja Kapper and Dipl.-Ing. Gisela Fauler for various encouraging discussions, their great efforts and for becoming real friends during the last years.

Additionally, I wish to acknowledge Dr. Christoph Stangl, Dr. Colin God and Dr. Martin Schmuck for their theoretical support on this doctoral thesis and publications. I would also like to thank Dr. Harald Kren, Andrea Droisner and MSc Pierre Baumann.

Last but not least I would like to express my very great appreciation to my family, especially my mother as well as Dr. Ulrike Holzer, Dr. Peter Holzer, Elfriede Pötz, and all of my friends, for giving me their unequivocal support throughout, as always, for which my mere expression of thanks likewise does not suffice.

## **ABSTRACT**

Environmental concerns, limitation of resources and the guarantee of prospective energy supply are among the main issues that currently attract great public attention. Therefore, technological improvements in rechargeable electrochemical power sources are driven by an ever-increasing demand of energy associated with rapid population growth. Lithium-ion battery technology has become very attractive and is the technology of choice for most of today's portable devices, such as laptops, digital cameras and cell phones. Furthermore, they attract great attention as power source for electric vehicle applications due to high energy density, high power density as well as prolonged life time. Nevertheless, state of the art lithium-ion batteries do not have sufficient energy density to compete with the performance of internal combustion engines. Approaches to enhance the energy density of these batteries are, among others, the development of high voltage cathode materials and high capacity anode materials. Moreover, the refinement of the cell design, focussing on reducing weight of the battery, is a potential approach to further increase the energy density of the final device.

This doctoral thesis deals with two topics: (i) the improvement of the battery cell design to enhance the capacity of the cathode and/or reduce the weight of the battery and (ii) the development of high capacity silicon/graphite composite anode materials.

## KURZFASSUNG

Klimawandel, Ressourcenknappheit und Sicherstellung der zukünftigen Energieversorgung zählen zu den zentralen Themen, die vermehrt im Brennpunkt der Öffentlichkeit stehen. Auf Grund des rapiden Bevölkerungswachstums strebt man, aus technologischer Sicht, unter anderem eine Verbesserung von wiederaufladbaren elektrochemischen Energiequellen an. Lithium-Ionen Batterien dienen bereits als Energiequelle für die meisten portablen Geräte wie Laptops, Digitalkameras oder Handys, nichts desto trotz ist das Potential dieser Technologie noch lange nicht ausgeschöpft. Die Elektromobilität zählt zu einem zukunftssträchtigen Anwendungsbereich, der den Marktanteil von Lithium-Ionen Batterien zu weiterem Wachstum verhelfen kann. Der Vorteil der Lithium-Ionen Batterie gegenüber anderen Batterietechnologien liegt in der hohen Energie- sowie Leistungsdichte und der langen Lebensdauer. Um aber auch nur annähernd mit dem Verbrennungsmotor konkurrieren zu können ist eine Verbesserung in Hinblick auf eine erhöhte Energiedichte von essentieller Bedeutung. Zu den Konzepten zur Erhöhung der Energiedichte von Lithium-Ionen Batterien zählen vor allem die Entwicklung von neuen Kathodenmaterialien die eine größere Spannung ermöglichen bzw. die Entwicklung von neuen Anodenmaterialien mit höherer Kapazität und die Verbesserung bereits bekannter hochkapazitiver Anodenmaterialien. Zudem wird auch eine Verbesserung des Zelldesigns zur Reduktion der Masse der Einzelzelle angestrebt, um eine erhöhte Energiedichte der Batterie zu gewährleisten.

In dieser Doktorarbeit werden zwei Ziele verfolgt: (i) eine Verbesserung des Zelldesigns um die Kapazität der Kathode zu erhöhen bzw. das Gewicht der Zelle zu reduzieren und (ii) die Entwicklung eines Silicium/Kohlenstoff Komposit als Anodenmaterial mit erhöhter Kapazität.

## TABLE OF CONTENT

<b>1.</b>	<b>INTRODUCTION</b> .....	1
<b>2.</b>	<b>ELECTROCHEMICAL SYSTEMS</b> .....	3
	<b>2.1. HISTORY &amp; GENERAL ASPECTS OF ELECTROCHEMISTRY</b> .....	3
	<b>2.2. IMPORTANT FEATURES OF A BATTERY</b> .....	9
	<b>2.3. DEPOSITION OF METALS</b> .....	12
	<b>2.3.1. Electroless deposition of metals</b> .....	12
	<b>2.3.2. Electrodeposition of metals</b> .....	13
	<b>2.3.3. Aluminium electrodeposition from non-aqueous solutions</b> .....	17
<b>3.</b>	<b>LITHIUM-ION-BATTERIES</b> .....	19
	<b>3.1. PRINCIPLE BEHIND LITHIUM-ION BATTERIES</b> .....	20
	<b>3.2. MATERIALS FOR THE CATHODE</b> .....	23
	<b>3.2.1. Layered oxide cathodes</b> .....	25
	<b>3.2.2. Spinel oxide cathodes</b> .....	26
	<b>3.2.3. Oxide cathodes with polyanions</b> .....	27
	<b>3.3. MATERIALS FOR THE NEGATIVE ELECTRODE</b> .....	27
	<b>3.3.1. Carbon as insertion material for the negative electrode</b> .....	28
	<b>3.3.2. Lithium alloys as negative insertion electrode material</b> .....	30
	<b>3.3.2.1. Silicon for lithium alloying</b> .....	30
	<b>3.3.3. Other intercalation compounds for the anode</b> .....	32
	<b>3.4. CURRENT COLLECTORS IN LITHIUM-ION BATTERIES</b> .....	33
	<b>3.5. COMMON ELECTROLYTES</b> .....	34
	<b>3.6. ELECTRODE/ELECTROLYTE INTERFACES – SOLID ELECTROLYTE INTERPHASE (SEI)</b> .....	37
<b>4.</b>	<b>EXPERIMENTAL</b> .....	42
	<b>4.1. MEASUREMENT METHODS AND SETUPS</b> .....	42
	<b>4.2. IMPLEMENTATION OF A 3D CURRENT COLLECTOR FOR THE POSITIVE ELECTRODE OF LIBS</b> .....	44
	<b>4.2.1. Preparation of the 3D current collector</b> .....	44
	<b>4.2.2. First generation non-woven polymer coated with Ni or Cu by electroless deposition and Al by electroplating</b> .....	45
	<b>4.2.3. Evaluation of the corrosion resistance of the new 3D current collector</b> .....	54
	<b>4.2.4. Determination of electrochemical and thermal decomposition products of EMImCl*1.5 AlCl<sub>3</sub> during Al electrodeposition</b> .....	61

4.2.4.1.	NMR analysis .....	63
4.2.4.2.	Py-GC/MS and headspace GC/MS analysis.....	63
4.2.5.	Comparison of mass, conductivity and contact surface area of different current collectors .....	67
4.2.6.	Electrode preparation and electrochemical characterisation .....	68
4.2.6.1.	Electrodes with 1. generation current collector .....	68
4.2.6.2.	Electrodes with 1. generation current collector after PVD of Al (300 nm).....	71
4.2.6.3.	Electrodes with 2. generation current collector .....	75
4.2.6.4.	Full cell assembling with electrodes composed of 3D current collectors.....	79
4.2.7.	Conclusion.....	82
<b>4.3.</b>	<b>SYNTHESIS OF AN ACTIVE MATERIAL FOR THE NEGATIVE ELECTRODE BASED ON SILICON AND DECOMPOSABLE POLYMERS.....</b>	<b>83</b>
4.3.1.	PolyHIPE as decomposable polymer for preparation of Si/C composites .....	84
4.3.2.	Polydicyclopentadiene as decomposable polymer for preparation of Si/C composites	87
4.3.2.1.	Active material with a silicon:graphite ratio of 20:80 and silicon particle size of 50-70 nm.....	91
4.3.2.2.	Active materials with a silicon:graphite:C ratio of 20:80:0 and 20:70:10 and silicon particle size of 30-50 nm.....	94
4.3.2.3.	Active materials with a silicon/graphite/carbon ratio of 30:70:0 and 30:60:10.....	97
4.3.3.	Polymethyl methacrylate/polyethyleneglycol dimethacrylate as decomposable polymer for preparation of Si/C composites.....	100
4.3.3.1.	Active material with a silicon/graphite ratio of 20:80 and 50-70 nm silicon particle size .....	103
4.3.3.2.	Active material with silicon/graphite ratio of 30:70 and 50-70 nm silicon particle size .....	106
4.3.3.3.	Active materials with a silicon/graphite ratio of 20:80 and silicon particle size of 30-50 nm.....	108
4.3.3.4.	Active materials with a silicon/graphite ratio of 30:70 and silicon particle size of 30-50 nm.....	111
4.3.4.	Conclusion.....	114
<b>5.</b>	<b>APPENDIX .....</b>	<b>115</b>
<b>5.1.</b>	<b>LIST OF CHEMICALS.....</b>	<b>115</b>
<b>5.2.</b>	<b>LIST OF DEVICES.....</b>	<b>116</b>
<b>5.4.</b>	<b>LIST OF FIGURES.....</b>	<b>118</b>
<b>5.5.</b>	<b>LIST OF TABLES.....</b>	<b>123</b>
<b>5.6.</b>	<b>LITERATURE.....</b>	<b>125</b>

# 1. INTRODUCTION

Lithium-ion batteries (LIBs) are a fast-growing technology being applied in portable electronics such as cell phones and laptops, due to their light weight and high power. Because of environmental concerns, they are believed to be a major power source for future electrical vehicle applications and energy storage [1] [2]. Examples for applications of lithium-ion batteries in dependence of their capacity as function of battery power are shown in figure 1.

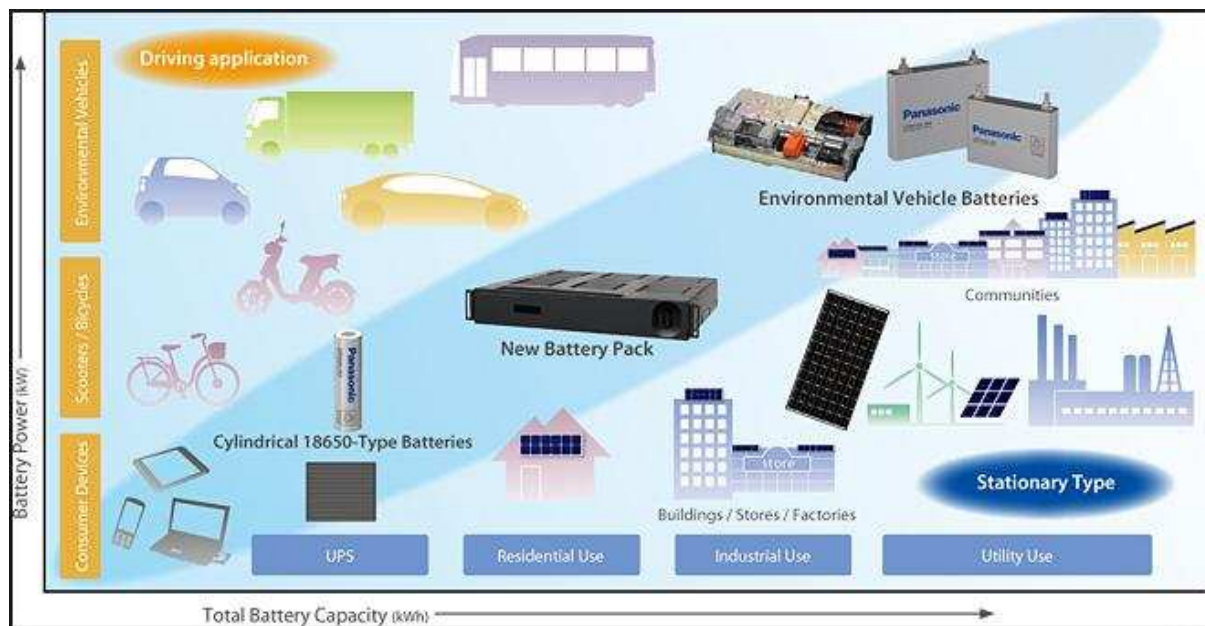


Figure 1: Lithium-ion battery application in dependence of the total battery capacity as function of the battery power [125]

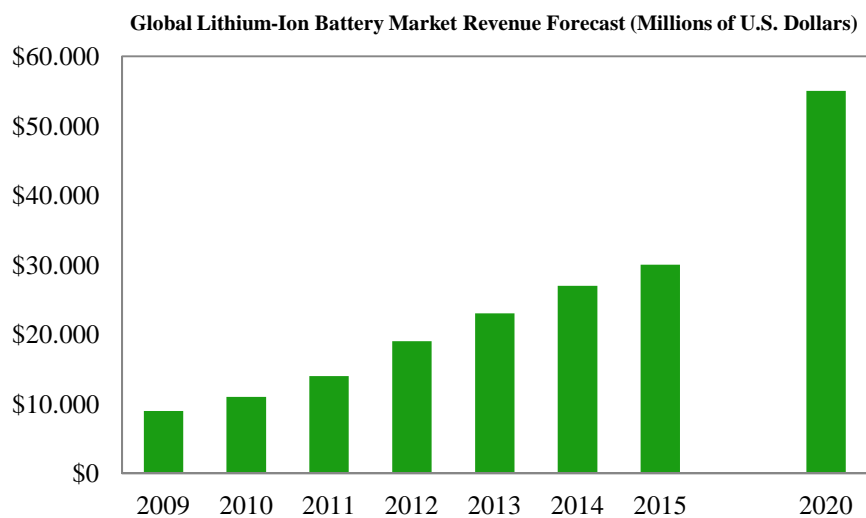


Figure 2: Global lithium-ion battery market revenue forecast (redrawn from [130])



As mentioned before, lithium-ion batteries already find wide usage in mobile electronic products (e.g. cell phones or lap tops) and usage in cars will fuel the bulk of sales growth (figure 2). In automotive application, required batteries should store energies of 5-60 kWh for electric cars and up to 100 kWh for electric buses [3] [4]. Therefore, it is necessary to reduce the size, volume and cost of lithium-ion batteries and simultaneously, to improve their energy density.

One approach is to look for new cathode and anode materials with higher capacities, but there is also a need to improve the battery cell design to maximize energy density [1] [2]. A reduction of inactive components could be achieved by increasing the mass load of the electrodes. In return there is the common practice to reduce layer thickness to enhance cell power density, which however comes at the expense of energy density, because of an unfavourable mass ratio of active to inactive components [5]. However, the traditional architecture of battery electrode materials on flat metal current collectors does not allow higher mass loadings due to a few difficulties, like delamination of electrode material from the flat current collector or electrolyte penetration through a thick electrode, which causes a loss of energy efficiency [6]. These problems could be overcome by the development of a 3D current collector. Examples of 3D current collectors include nanotubes grown on metal foils [7], porous conductive textiles [6], carbon and metal foams [8] [9] and metal meshes [10].

This work focuses on the development of a 3D current collector for the positive electrode in lithium-ion batteries, based on a non-woven polymer, which is plated with a thin layer of nickel by chemical reduction followed by electrodeposition of an aluminium layer from ionic liquid. Alternatively, the non-woven polymer was aluminised by physical vapour deposition. Electrodes were produced with the metallised non-woven polymers and these electrodes were electrochemically characterised in half cells. Finally, electrodes with 3D current collectors were successfully implemented in full cells, where both electrodes cathode as well as anode, contained aluminium respectively copper plated non-woven polymers.

On the other hand, synthesis of active materials for the negative electrode with higher capacities, based on nano-silicon, coated by different decomposable polymers, was carried out in the scope of this doctoral thesis. Electrodes with these active materials were electrochemically characterised in half cells and an improvement in cycleability, compared to common silicon-graphite composite electrodes, could be observed.

## 2. ELECTROCHEMICAL SYSTEMS

### 2.1. HISTORY & GENERAL ASPECTS OF ELECTROCHEMISTRY

The electrochemical scientific community pays attention to chemical reactions at the solution/electrode interface, where an electron transfer is involved. A battery is a chemical device for the storage of electricity, since batteries convert chemical energy into electrical energy.

The smallest conceivable unit of a battery is called the electrochemical cell. Depending on desired voltage and capacity, a battery consists of a certain amount of these electrochemical cells. Batteries could be classified into two broad categories: (i) primary batteries, which could be discharged just once and (ii) secondary batteries, which may be recharged until the secondary battery deteriorates and its storage capacity fades below a practical level [11].

The first battery was invented in 1800 by Alessandro Volta, which consisted of a stack of galvanic cells, where each cell was composed of two electrodes, one made of copper and the other made of zinc. These electrodes were separated by a textile, soaked in acidic solution [12]. Another important step in development of batteries was the invention of the Daniell cell by John Daniell in 1836. It consisted of a copper vessel, filled with copper sulphate solution, where he immersed a gullet of an ox. This tube contained a solution of sulphuric acid and a vertical zinc rod. During discharge, this cell gave a voltage of 1.1 V, where the zinc electrode was dissolved and copper was deposited at the positive electrode [11].

In 1866 the French chemist George Leclanchè developed a primary cell, which bears his name. The Leclanchè cell was composed of a zinc rod as negative electrode and a carbon rod as positive electrode, both immersed in a solution of ammonium chloride. All components were packed in a glass jar and this cell gave a voltage of 1.5 V. A further advantage took place in the 19<sup>th</sup> century, where the glass jar was replaced by a zinc can, used as both, container and electrode [11].

In battery science and technology major advances have been made in the 20<sup>th</sup> century. The invention of alkaline batteries significantly improved the primary Leclanchè cell while advances in materials technology and cell design revolutionized the performance of lead-acid batteries. Furthermore, several secondary batteries have been developed and commercialized, including the nickel-metalhydride battery and the lithium-ion battery [11].

Every electrochemical cell consists of three major components [13]:

- *Negative electrode or anode:* is oxidized during the electrochemical reaction; gives up electrons to the external circuit
- *Positive electrode or cathode:* is reduced during the electrochemical reaction; accepts electrons from the external circuit
- *Electrolyte:* ionic conductor; could be liquid (water or other solvents with dissolved salts, acids or alkalis), solid or a gel-type polymer. The electrolyte must not be electrically conductive but should provide good ionic conductivity. Both electrodes are usually isolated by a separator. The separator is electronically insulating but permeable for the electrolyte to ensure ionic conductivity.

The operation principle of a battery should be demonstrated on the basis of the Leclanchè cell (figure 3).

During discharge, when the cell is connected to an external circuit, the electrons move from the negative electrode (anode) to the positive (cathode). The anode, which consists of zinc in this case, is oxidized by meaning that zinc will be dissolved and donates electrons for the reduction of  $\text{MnO}_2$ . The cathode of this cell is made of graphite [13].

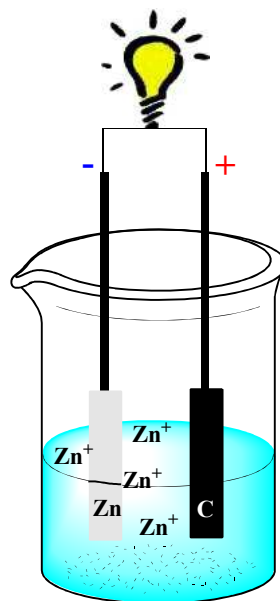
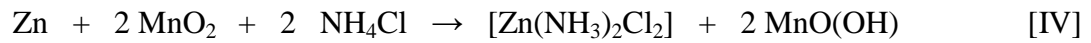
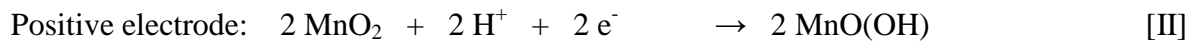


Figure 3: Schematic representation of a Leclanchè cell



In principle, during recharge the current flow is reversed. Oxidation takes place at the positive electrode and reduction at the negative electrode. Due to the definition that the anode is the electrode, at which oxidation takes place and the cathode the one, where reduction occurs, the positive electrode is now the anode and the negative electrode the cathode [13].

As mentioned before, the Leclanchè cell is a primary battery, which couldn't be recharged again. Examples for rechargeable batteries (secondary batteries) are the nickel-metal hydride battery or the lithium-ion battery (LIB). The LIB will be discussed more in detail in chapter 3.

The standard potential of a cell is determined by the type of active materials combined in the cell. Whenever a reaction occurs, the Gibbs free energy ( $\Delta G$  [J mol<sup>-1</sup>]) of the system will be changed, from which the potential will be derived [12]:

$$\Delta G^\circ = -nFE^\circ \quad \text{(Eq. 1)}$$

F.....Faraday constant [ $\approx 96500$  C]

n.....number of electrons involved

$E^\circ$ .....standard potential [V]

For spontaneous reactions the change in free energy will be negative ( $\Delta G^0 < 0$ ) and therefore the standard electrode potential will be positive ( $E^0 > 0$ ).

A fundamental mathematical expression for describing the voltage in correlation of concentration for all cell reactions is the Nernst equation [12]:

$$E = E^{\circ} + \frac{RT}{nF} \ln \frac{[Ox]}{[Red]} \quad (\text{Eq. 2})$$

$E^{\circ}$  .....standard potential [V]

$R$ .....Universal gas constant (8.314472 [J K<sup>-1</sup> mol<sup>-1</sup>])

$T$ .....temperature [K]

$F$ .....Faraday constant [ $\approx 96500$  C]

Ox.....concentration of oxidized species [mol L<sup>-1</sup>]

Red.....concentration of reduced species [mol L<sup>-1</sup>]

The Nernst equation is only legal in reactions without mass transport and current flow.

Table 1: Standardpotential of some metals against NHE (V) [14]

Electrode		Electrode reaction	$E^{\circ}/V$
Au	Gold	$\text{Au}^{3+} + 3 e^{-} \leftrightarrow \text{Au}$	+ 1,43
Ag	Silver	$\text{Ag}^{+} + e^{-} \leftrightarrow \text{Ag}$	+ 0,80
Cu	Copper	$\text{Cu}^{2+} + 2 e^{-} \leftrightarrow \text{Cu}$	+ 0,34
H	Hydrogen	$\text{H}^{+} + e^{-} \leftrightarrow \text{H}$	0
Pb	Lead	$\text{Pb}^{2+} + 2 e^{-} \leftrightarrow \text{Pb}$	- 0,13
Sn	Tin	$\text{Sn}^{2+} + 2 e^{-} \leftrightarrow \text{Sn}$	- 0,14
Ni	Nickel	$\text{Ni}^{2+} + 2 e^{-} \leftrightarrow \text{Ni}$	- 0,25
Cd	Cadmium	$\text{Cd}^{2+} + 2 e^{-} \leftrightarrow \text{Cd}$	- 0,40
Fe	Iron	$\text{Fe}^{2+} + 2 e^{-} \leftrightarrow \text{Fe}$	- 0,44
Zn	Zinc	$\text{Zn}^{2+} + 2 e^{-} \leftrightarrow \text{Zn}$	- 0,76
Ti	Titanium	$\text{Ti}^{2+} + 2 e^{-} \leftrightarrow \text{Ti}$	- 1,63
Al	Aluminium	$\text{Al}^{3+} + 3 e^{-} \leftrightarrow \text{Al}$	- 1,66
Mg	Magnesium	$\text{Mg}^{2+} + 2 e^{-} \leftrightarrow \text{Mg}$	- 2,37
Na	Sodium	$\text{Na}^{+} + e^{-} \leftrightarrow \text{Na}$	- 2,71
K	Potassium	$\text{K}^{+} + e^{-} \leftrightarrow \text{K}$	- 2,93
Li	Lithium	$\text{Li}^{+} + e^{-} \leftrightarrow \text{Li}$	- 3,05

Some selected electrode reduction potentials under standard conditions are listed in table 1. Each half cell reaction has a specific standard potential reported as the reduction potential vs. the normal hydrogen electrode (NHE). The standard potential of the NHE is arbitrary set to zero.

The standard potential of a cell could be calculated from the standard electrode potentials using following equation [12]:

$$E^{\circ}_{(cell)} = E^{\circ}_{(cathode)} - E^{\circ}_{(anode)} \tag{Eq. 3}$$

If the current in anodic and cathodic direction is equal (net current is zero), the galvanic cell is in equilibrium. In that case the electrode potentials can be evaluated according to the Nernst equation (eq. 2). The current related to an electrode area is called current density or exchange current density  $j_0$  [A cm<sup>-2</sup>] [15].

When a system is charged with current, a shift in the potential of the single half-cell is measured, called over-potential  $\eta$  [16]:

$$\Delta\varepsilon_{(real)} = \Delta\varepsilon_{(0)} - \sum|\eta| \tag{Eq. 4}$$

A system in nonequilibrium conditions, such as current flow resulting from electrode polarization (overvoltage), shows an exponential relation between the applied overpotential and the current that passes through the circuit and can be described by the Tafel equation [12], [15]:

$$\eta = \frac{RT}{\alpha F} \ln j_0 - \frac{RT}{\alpha F} \log j \tag{Eq. 5}$$

- $\eta$ .....overpotential [V]
- $j$ .....current density [A cm<sup>-2</sup>]
- $j_0$ .....exchange current density [A cm<sup>-2</sup>]
- $\alpha$ .....transfer coefficient

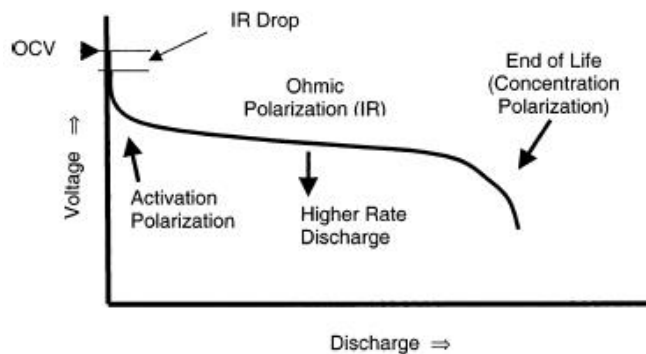


Figure 4: Discharge characteristic of a battery [17]

A typical discharge characteristic of a battery is shown in figure 4. The shape of such a curve results from the various resistances, which occur as a result of different overpotentials.

The sum of the overpotentials of a system should be kept as low as possible and one can distinguish between different types, depending on their origin:

### (1) Charge-transfer overpotential

This type of overpotential is caused by a limitation on the velocity of charge transfer through the electrode/electrolyte interface. It depends on the reacting substances, the electrolyte and the characteristics of the electrode. The current density at an electrode in terms of the overpotential can be described by the Butler-Volmer equation [16]:

$$j = j_0 \left[ \exp \frac{(1-\alpha)F\eta}{RT} - \exp \frac{-\alpha F}{RT} \right] \quad (\text{Eq. 6})$$

$j_0$ .....exchange current density [A cm<sup>-2</sup>]  
 $\eta$ .....overpotential [V]  
 $\alpha$ .....transfer coefficient

### (2) Diffusion overpotential

In the case of an impoverishment of electro-active species at the electrode surface (Nernst diffusion layer) the reaction kinetics is only determined by diffusion processes through this region. The diffusion overpotential that occurs can be expressed by the following formula [16]:

$$\eta_{(diff)} = \left| \frac{RT}{zF} \ln \left( 1 - \frac{j_0}{j_{(limit)}} \right) \right| \quad (\text{Eq. 7})$$

$j_0$ .....exchange current density [A cm<sup>-2</sup>]  
 $j_{(limit)}$ .....maximum current density [A cm<sup>-2</sup>]

### (3) Reaction overpotential

This type of overpotential occurs, when adsorption- and desorption processes are the speed limiting factors [16].

#### (4) Crystallization overpotential

The crystallisation is an elementary step in the overall electrode reaction. Crystallisation overpotential is caused by surface diffusion of the atom, which is adsorbed onto the surface, and the incorporation into the crystal lattice [18].

## 2.2. IMPORTANT FEATURES OF A BATTERY

For characterisation and comparison of different battery systems some important key parameters have to be defined.

The **open circuit voltage (OCV)** is the potential of a working electrode relative to a counter- or reference electrode, when no current is applied to the cell or the voltage released in a battery at zero net current flow. The **terminal voltage U** between two electrodes is measured during charging and discharging of the cell [16]. The terminal voltage of a cell is fixed by the active materials used in the battery and depends on the so called cell chemistry.

The **cycle life** of a secondary cell is another important parameter for describing a rechargeable battery. It indicates the achievable number of charging- and discharging cycles until a lower limit of the capacity of the battery is reached.

The **capacity** is described as the amount of electric charge, that could be stored or delivered by a battery and is quoted in Ah.

The resulting diagram of the application of the terminal voltage U as function of the discharge current is called **current-voltage characteristic**. The **electric power P** [W] or the power density [W L<sup>-1</sup>], delivered by a battery at a given time can be calculated by the following formula [16]:

$$P = I * U \quad (\text{Eq. 8})$$

The **energy** [m<sup>2</sup> kg s<sup>-2</sup>] or the **energy density** [Wh L<sup>-1</sup>] can be calculated according to the following equation:

$$W = \int_{t_1}^{t_2} U(t) * I(t) * dt \quad (\text{Eq. 9})$$



Generally, the required charge ( $Q_{\text{charge}}$ ) to load a secondary cell is always higher than the charge ( $Q_{\text{discharge}}$ ), which could be delivered during discharging the battery. The **coulometric efficiency** of a secondary battery can be explained by parasitic side reactions like SEI formation and irreversible lithium-ion trapping. The **energy efficiency** depends on a few parameters like the applied current density, temperature, thickness and porosity of the separator and conversion of electric energy into heat [16].

Coulometric efficiency: 
$$q_{Ah} = \frac{Q_{\text{discharge}}}{Q_{\text{charge}}} \quad (\text{Eq. 10})$$

Energy efficiency: 
$$q_{Wh} = q_{Ah} * \frac{U_{\text{discharge}}}{U_{\text{charge}}} \quad (\text{Eq. 11})$$

$U_{\text{discharge/charge}}$ .....average terminal voltages during discharge and charge

Usually, the coulometric efficiency is higher than the energy efficiency. The reason for this phenomenon is the fact that the discharge voltage is normally lower than the charge voltage, due to the internal resistance and overpotential [16].

Another important criterion for the assessment of a battery system is the **discharge characteristic**. Such a curve can be obtained by plotting the terminal voltage against the discharge capacity (figure 5). For velocity of charging and discharging the c-rate is defined by the charge- and discharge current and the nominal capacity of the accumulator [16]:

$$C = \frac{\text{discharge current}}{\text{nominal capacity}} \quad (\text{Eq. 12})$$

The obtainable capacity of a battery depends on the c-rate during discharging. The higher the c- rate, the lower is the achievable capacity (figure 5) [16].

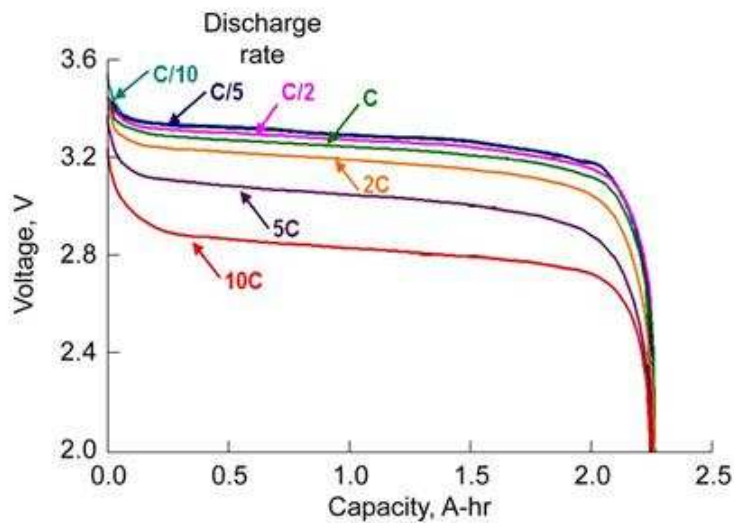


Figure 5: Discharge characteristic of a LIB with different c-rates [19]

The resulting chart after plotting energy density [ $\text{Wh kg}^{-1}$ ] vs. power density [ $\text{W kg}^{-1}$ ] is called **Ragone plot** (figure 6). It is used to compare the characteristics of different energy storage devices. It shows that capacitors can deliver very high power density accompanied by a low energy storage capacity, whereas fuel cells are able to store large amounts of energy but with a relatively low power output. Combustion engines combine both properties: high energy density and high power density [20].

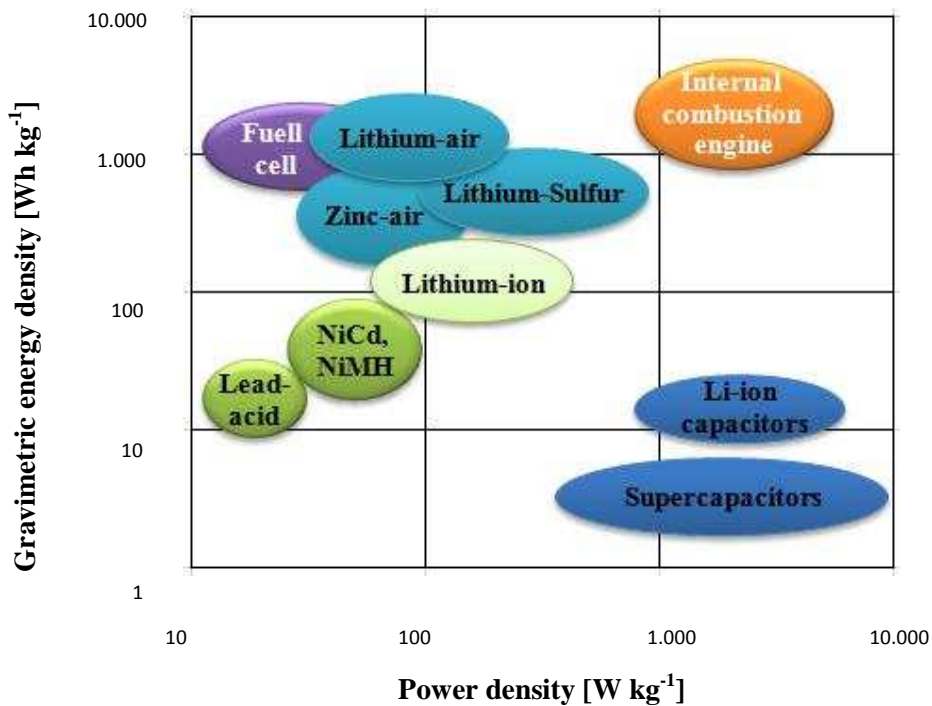


Figure 6: Ragone plot with current and next-generation energy storage technologies [21]

## 2.3. DEPOSITION OF METALS

Metal coatings of surfaces are of major technological and economic importance. Surface finishing processes are used in many fields like mechanical engineering, aircraft and spacecraft or automotive and medical technology. Functional coatings can modify the properties of different surfaces, for example their hardness, ductility and chemical or corrosion resistance. The protection against corrosion, wear and tear of surfaces is of special importance [22].

There are several methods available for achieving metal coatings on substrates, like the reduction of metal ions from electrolytes through electrochemical or chemical reduction, metal deposition from the gas phase (physical or chemical vapour deposition) or coatings from melts of the desired metal (hot dipping) [23].

Deposition of metals refers to a continuous growth of a metallic film on a substrate by reduction of metal ions from a solution, containing the desired metal ions (electrolyte). The reduction of metal ions can be achieved either by chemical or by electrochemical reduction. Aqueous solvents are often used for the deposition of metal ions, however, metals with a very negative standard potential (electrochemical series, table 1) couldn't be reduced from aqueous solution due to water decomposition. In this case, molten salts, ionic liquids or organic solutions can be used as electrolytes [24].

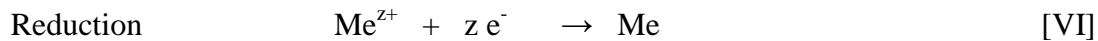
### 2.3.1. Electroless deposition of metals

Electroless metal deposition is a tool for making surfaces (e.g. insulating polymers) conductive. Autocatalytic metal deposition baths have the capacity to reduce metal ions without an external supply of electrons. Usually such a plating bath comprises of a solution of the desired metal ions, a reducing agent, capable to reduce these metal ions, a complexing agent for the metal ions and a pH regulator [25].

To achieve a well adherent metal layer on a non-conductive surface, this surface has to be pretreated with an etching- and an activating solution to form crystallisation nuclei on the substrate (e.g. an acidic solution of PdCl<sub>2</sub>) [25]:



Two half reactions are taking place during electroless metal deposition: first, the reducing agent is going to lose electrons and is being oxidized, whereas the metal ions receive these electrons and therefore will be reduced on the surface of the substrate [26].



### 2.3.2. Electrodeposition of metals

Electrodeposition or electroplating refers to a process, where metal ions are reduced on a substrate, which works as electrode and is therefore connected to an external power source. Either an inert electrode like platinum is used, where the oxidation reaction takes place, or a sacrificial anode is used as source for metal ions, which consists of the metal to be plated. Both electrodes, anode and cathode, are immersed in an electrolyte and when a current is applied, the anode works as source for electrons and/or metal ions and is oxidized, whereas the metal ions receive electrons at the surface of the cathode (substrate to be coated) and are deposited there [24].

An important theory for calculating the amount of metal, which is deposited during electrolysis or the calculation of the time of electrolysis to achieve a desired thickness is the Faraday's law [24]. It correlates the total charge  $Q$  [C], passed through a cell to the amount of product [12]:

$$Q = nFN \quad (\text{Eq. 13})$$

$$m = \frac{QA}{nF} \quad (\text{Eq. 14})$$

$Q$ .....net charge passed through the circuit [C]

$n$ .....number of transferred electrons

$N$ .....Avogadro constant

$F$ .....Faraday constant  $\approx 96500 \text{ C mol}^{-1}$

$m$ .....deposited mass of metal [g]

$A$ .....atomic weight of the metal [ $\text{g mol}^{-1}$ ]

Faraday's first law of electrolysis says, that the changes of the mass of a substance at an electrode during electrolysis is direct proportional to the quantity of electricity transferred through the electrode. The second law says, that for a given electric charge the mass of an elemental material altered at an electrode is directly proportional to its equivalent weight (eq. 14) [27].

Without an applied external current, equilibrium between the electrode and its metal ions is prevailing and the resulting current is equal to the exchange current density  $j_0$ :



An applied external current will disturb this equilibrium, resulting in acceleration or hindrance of the reaction. The current density [ $\text{A cm}^{-2}$ ] regulates the rate of the deposition process. At thermodynamic equilibrium, the current density is zero and the associated electrode potential is called equilibrium potential  $E_{\text{eq}}$  of this process. This potential is directly linked to the activity of the electro-active species in solution and can be described by the Nernst equation (eq. 2). To deposit a metal at a finite rate, it is necessary to polarize the electrode potential in negative (cathodic) direction. Therefore, the reduction processes will be accelerated, whereas a more positive polarization of the anode will speed up anodic processes (oxidation). The value of these potential shifts is called over-potential  $\eta$  (eq. 4). The over-potential, that has to be applied, depends on the metal and has a significant influence on the microstructure and morphology of the deposits. Metals with high exchange current density values correspond to low over-potentials and vice versa [24].

Usually it is assumed, that the current density is uniform across the surface. However, at substrates with complex geometries metal deposition at edges and corners is highly preferred due to an inhomogeneous current distribution, called bone effect (figure 7) [24].

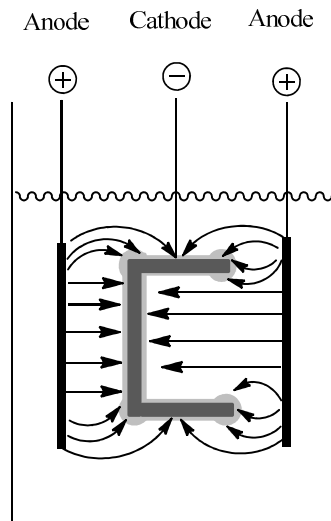


Figure 7: Schematic representation of the bone effect in following inhomogeneous current distribution [28]

In most practical processes side reactions may occur during electroplating in order to consume current (charge). Examples for these side reactions are hydrogen evolution as result of water decomposition, co-deposition of another metal, partial reduction of metal ions or reduction of surface oxide layers.

When side reactions proceed, the determination of the current efficiency [%] is of interest. The current efficiency is defined as the ratio of the partial current of the metal deposition process and the overall current [24].

For practical determination of the current efficiency, the mass of the substrate will be determined before and after metal deposition and the current efficiency can be calculated according to Faraday's law (eq. 14). In addition to current density and electrode potential many parameters like temperature of the electrolyte, pH value, substrate, concentration of electro-active ions or parasitic processes like water decomposition may influence electroplating processes, microstructure and morphology of the deposit [24].

The electrodeposition of metals occurs between the interphase of the electrode surface and the electrolyte solution, a region with finite thickness, called double layer. In general, charge separation occurs within this region as result of different charged species; on one hand, electrons in the solid state of the electrode and on the other hand ions in the solution. The simplest model assumes that counter ions bind electrostatically to a charged surface and neutralize the surface charges. This model was developed by Helmholtz and is therefore called **Helmholtz double layer**.

Here, the electric potential falls from the surface value to zero in the bulk solution over the thickness of the layer of counter ions [29]. A further development of this model was made by **Gouy and Chapman**. They assumed that ions are subject of thermal movement and would not be immobilized in a rigid layer on the electrode surface. They suggest that the ions which neutralize the surface charge are bound in a more diffuse double layer, than mentioned by Helmholtz. According to this theory, the surface potential falls more slowly to the bulk solution, describing an exponential function. The **model of Stern** combines these two models and suggested a model, where ions are bound on the surface to neutralize parts of the charge (Helmholtz layer) but the remaining charge would be neutralized by ions in a diffuse layer extended to the solution (figure 8) [30].

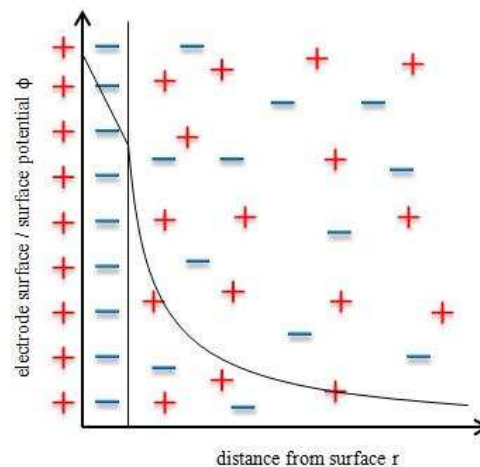


Figure 8: Stern model of the electric double layer [30]

### 2.3.3. Aluminium electrodeposition from non-aqueous solutions

Electrodeposition from conventional aqueous solutions is not possible for all metals, due to the evolution of hydrogen gas during electrolysis and the narrow electrochemical stability window. Aluminium is an example for a metal, which can't be deposited from aqueous solution because of the rather negative standard potential (electrochemical series, table 1, figure 9). Therefore, the electrolytes must be aprotic [23] [31].

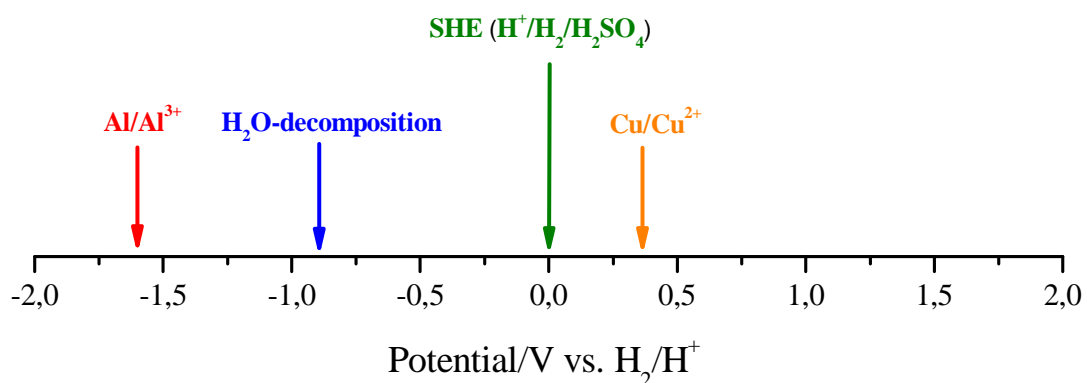


Figure 9: Some standard potentials of metal ions and water decomposition vs. NHE

The electrolyte for Al electrodeposition has to fulfil a few requirements [23]:

- The solvent should act as Lewis base and the solute should act as Lewis acid, so that co-ordination and dissolution of the solute can take place.
- The solute should be highly soluble in the solvent and a stable complex must be formed in the plating bath. The co-ordination centres of the solute should be weak enough that Al could be released during electroplating.
- The solvent should exhibit a wide electrochemical window to prevent decomposition of the solvent during Al deposition.
- The formed Al complex must release aluminium at a less negative potential than that of possible electrode reactions involving the solvent.

The first developed aluminium plating bath, which worked on industrial scale was the so called NBS-bath (National Bureau of Standards). It consists of dissolved AlCl<sub>3</sub>/LiH or LiAlH<sub>4</sub> in diethyl ether. Due to a few drawbacks like the low boiling point, volatility and low flashpoint of the solvent, diethyl ether was displaced by THF (tetrahydrofuran). Furthermore, AlCl<sub>3</sub> was added for improvement of the plating bath (REAL-process) [23] [32].



Electrodeposition of Al is also possible from so called bromide baths ( $\text{AlBr}_3 + \text{MBr}$  and  $\text{R}_4\text{NBr}$  in aromatic solvents) and from organoaluminium compounds dissolved in toluene ( $\text{AlEt}_3 + \text{Al}(\text{i-Bu})_3/\text{KF}$ ) called the “SIGAL-process” (Siemens galvanoaluminium) [23] [33].

Since the discovering of room temperature ionic liquids (RTIL), this class of electrolytes have become very important for aluminium electroplating. Ionic liquids are salts having comparative low melting points, resulting in a liquid aggregate state at room temperature. The first generation of ionic liquids are based on  $\text{AlCl}_3$ , having a hygroscopic nature, so they have to be prepared and handled under an inert-gas atmosphere. The most important IL for electrodeposition of aluminium is  $\text{EMImCl} \cdot 1.5 \text{ AlCl}_3$  (1-ethyl-3-methyl-imidazolium chloride). Beside this a variety of ILs were developed and implemented for aluminium plating [31] [34].

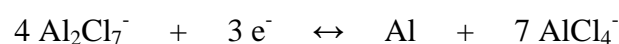
The greatest advantages of ionic liquids are [31]:

- non-volatility and inflammability
- good solubility for both organic and inorganic compounds
- high thermal stability
- wide electrochemical stability window

But ionic liquids have also a few drawbacks:

- low conductivity and high viscosity compared to aqueous electrolytes
- expensive



Depending on the ratios of  $\text{AlCl}_3$  dissolved in  $\text{EMImCl}$  three different melts can be distinguished: acidic ionic liquids with more than 50 mol%  $\text{AlCl}_3$ , basic melts with less than 50 mol%  $\text{AlCl}_3$  and neutral ones with a molar ratio of 1 for  $\text{EMImCl}/\text{AlCl}_3$ . The only reducible aluminium species within the electrochemical potential window is  $\text{Al}_2\text{Cl}_7^-$ , which occurs only in acidic melt. Therefore, electrodeposition of aluminium is carried out in melts with a ratio of more than 50 mol%  $\text{AlCl}_3$  [35]:



### 3. LITHIUM-ION-BATTERIES

One of the most important challenges of modern electrochemistry is the development of advanced rechargeable Li-ion batteries. These batteries show a great promise as power sources that can lead to the electric vehicle (EV) revolution. Due to their high energy density and enhanced rate capability they power most of today`s portable devices and seems to have the best properties for more demanding applications, such as EV (see also the Ragone plot – figure 6).

Table 2: Advantages and disadvantages of LIBs compared to other rechargeable battery systems [36]

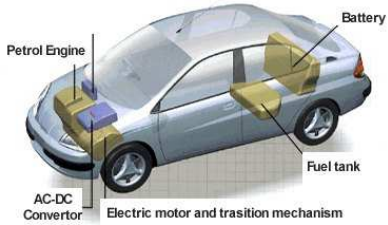
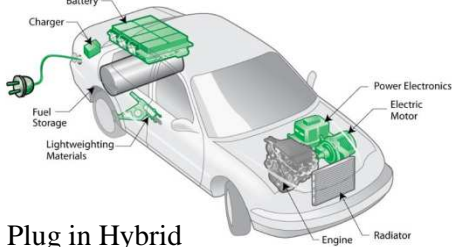

 Advantages of LIBs	 Disadvantages of LIBs
- high energy	- high charging times
- lightest weight	- thermal runaway concerns
- good cycle life	- expensive
- no memory effect	- prevention of overcharge and over discharge
- high energy efficiency	- limited resources of cobalt
- good high rate capability	

The working principle of a rechargeable lithium-ion battery is based on the movement of lithium ions through the electrolyte and electrons through the outer electrical circuit. The ions move from the negative electrode (anode) to the positive electrode (cathode) during discharge, and back while charging. Since the metallic lithium anode was displaced by intercalation materials for safety reasons the working mechanism is often related to that of a rocking chair, because the lithium ions swing between negative and positive electrode through a liquid organic electrolyte. In the 1970s, Whittingham was the first who proposed the “rocking chair concept” when he discovered the principle of the intercalation reaction. The first, who patented LiCoO<sub>2</sub> as intercalation cathode was Goodenough in 1980 and Ikeda of Sanyo was the first to patent an intercalation material, such as graphite, in an organic solvent in 1981. The success story of lithium-ion cells began with the commercial production in 1991 by Sony. During the last 20 years LIBs replaced many other commercial battery systems and dominated the market by powering modern portable electronics [36]. The electric vehicle revolution strongly depends on the development of new generation LIBs that can meet the new challenges like higher energy density, prolonged cycle life and sufficient safety features.

However, state-of-the-art LIBs with a specific energy of  $\sim 200 \text{ Wh kg}^{-1}$  can't compete with the performance of internal combustion engines (Ragone plot, figure 6), which makes a further development of different compounds of Li-ion batteries necessary [1] [37] [38].

Three main options for electric vehicle operation with associated properties of the battery system are listed in table 3.

Table 3: Characterisation of the main three types of EVs in terms of performance and battery properties [4] [37]

Modes of operation	Battery capacity needed [kWh]	Energy density [Wh kg <sup>-1</sup> ]	Weight of battery [kg]	Speed [km h <sup>-1</sup> ]	Distance on one charge [km]
 <p>Hybrid</p>	<3	40-50 (Ni-MH)	60 (Ni-MH)	100+	15
 <p>Plug in Hybrid</p>	5.6-18	90-100 (Li-ion)	60-200 (Li-ion)	100+	10-60
 <p>Full EV</p>	35-57	90-100 (Li-ion)	450 (Li-ion)	>100	150-200

### 3.1. PRINCIPLE BEHIND LITHIUM-ION BATTERIES

The main components of a typical lithium-ion cell are a negative electrode (anode) and a positive electrode (cathode), which are separated by a porous polymer (separator). The separator is soaked in an electrolyte, which usually consists of  $\text{LiPF}_6$ , dissolved in a mixture of organic solvents such as ethylene carbonate (EC) and diethyl carbonate (DEC).

The anode is usually composed of a thin layer of powdered graphite, coated on a copper foil, although there are several other active materials for the negative electrode available (e.g. soft carbons, hard carbons, LTO, etc.). Possible active materials for the cathode are  $\text{LiCoO}_2$ ,  $\text{LiFePO}_4$ ,  $\text{LiMn}_2\text{O}_4$  and many more, coated on aluminium foil [36] (figure 10).

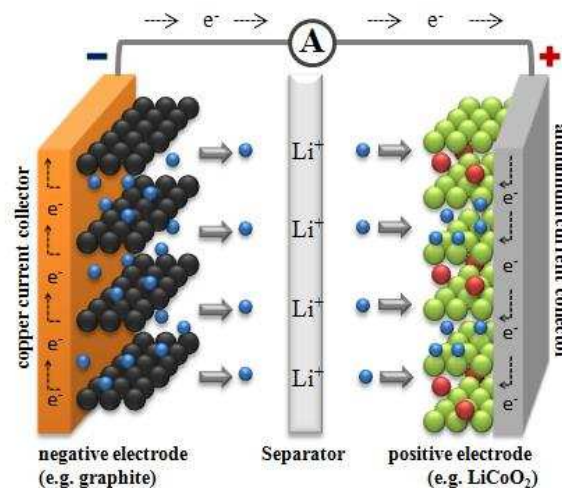


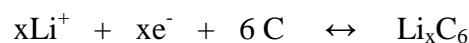
Figure 10: Schematic representation of a lithium-ion battery

Both electrode materials have the ability to intercalate and deintercalate lithium ions reversibly. During discharge, electrons pass from the anode to the cathode through an external electric circuit. Lithium ions are extracted from the negative electrode, move through the electrolyte and intercalate in the lattice of the cathode material. The reverse happens during charging, in which lithium ions deintercalate from the positive electrode and get intercalated into the negative electrode [36] [39].

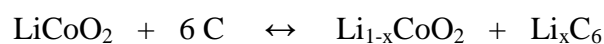
The positive electrode half-reaction can be represented as:



The negative electrode half reaction (in the case of graphite) is:



The overall reaction can be represented as:



After assembling, a lithium-ion battery is always in the discharged state and therefore it has to be charged before it can be used.

For the successful implementation in LIBs, an active material has to fulfil several criteria. The mentioned points below are valid for materials for the cathode as well as for the anode [40]:

- For maximization of the cell capacity, the lithium insertion compound should allow insertion/extraction of a large amount of lithium ions. A combination of high capacity and cell voltage can maximize the energy density, which is given by the product of capacity and voltage.
- The host material should have good conductivity for electrons as well as for lithium-ions to minimize polarization losses during the charge/discharge process and to support a high current density and power density.
- In case of a cathode material, the transition metal  $M^{n+}$ , in the insertion compound  $Li_xM_yX_z$  should have a high oxidation state for a high lithium chemical potential (maximization of the cell voltage). If used as anode, the transition metal should have a low oxidation state (low lithium chemical potential).
- To provide a good cycle life for the cell, the insertion compound should have good structural stability in order to keep the structural changes during the insertion/extraction process to a minimum. The lithium insertion/extraction process should also be reversible.
- The host material should be chemically and electrochemically stable over the entire range of lithium insertion and extraction. It should also be inexpensive, environmental benign and lightweight.

For achieving a reasonable energy density, anode and cathode materials should be chosen in order to maintain a cell voltage of more than 3 V. Therefore, to maximize the cell voltage, the anode and cathode insertion materials should have the lowest and highest voltages versus metallic lithium, respectively [40]. Figure 11 provides an overview of possible electrode materials and the operating potential of these materials is plotted versus the theoretical capacity.

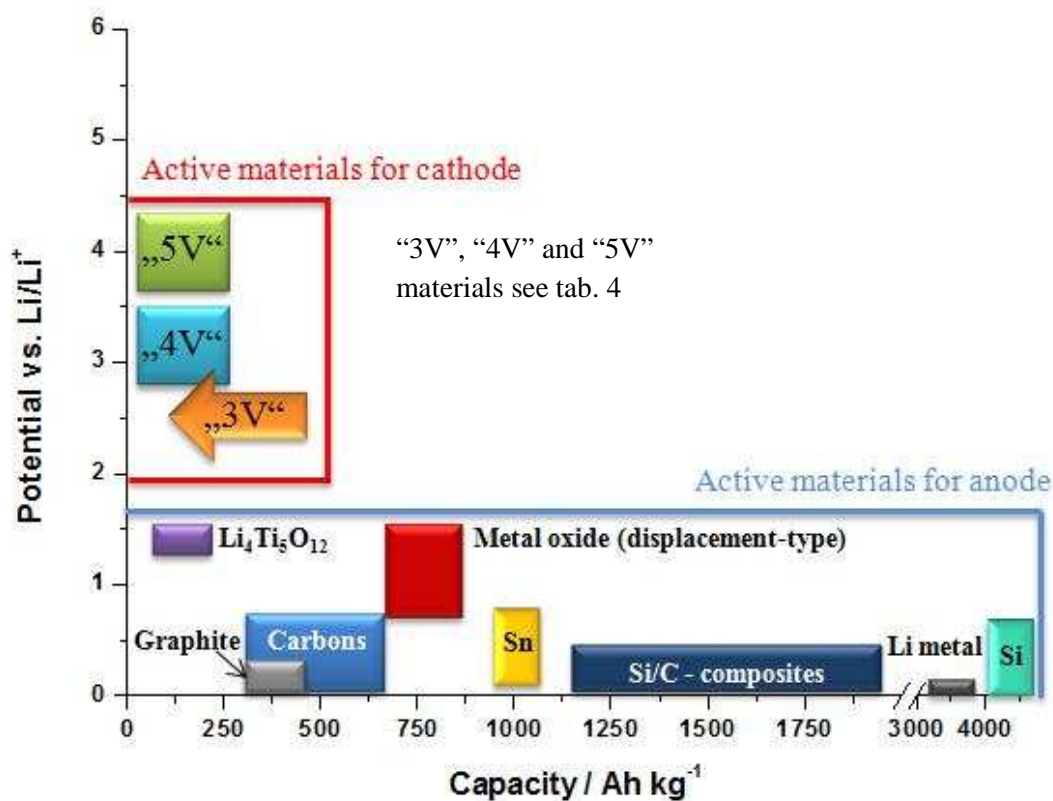


Figure 11: Comparison of the energy densities of different active materials for cathodes and anodes in LIBs [41]

### 3.2. MATERIALS FOR THE CATHODE

Cathode materials could be assigned to three possible categories according to their insertion mechanism (figure 12) [42]:

- 1 D (olivine type materials)
- 2 D (layered materials)
- 3 D (spinel materials)

Most cathode materials used in lithium-ion batteries are layered materials, which enables a two-dimensional diffusion of lithium ions. Three-dimensional diffusion is allowed by spinel materials. They have the advantage that they are more stable and that lithium-ion diffusion is clearly faster in the 3D framework compared to the two-dimensional cathode materials (figure 12).

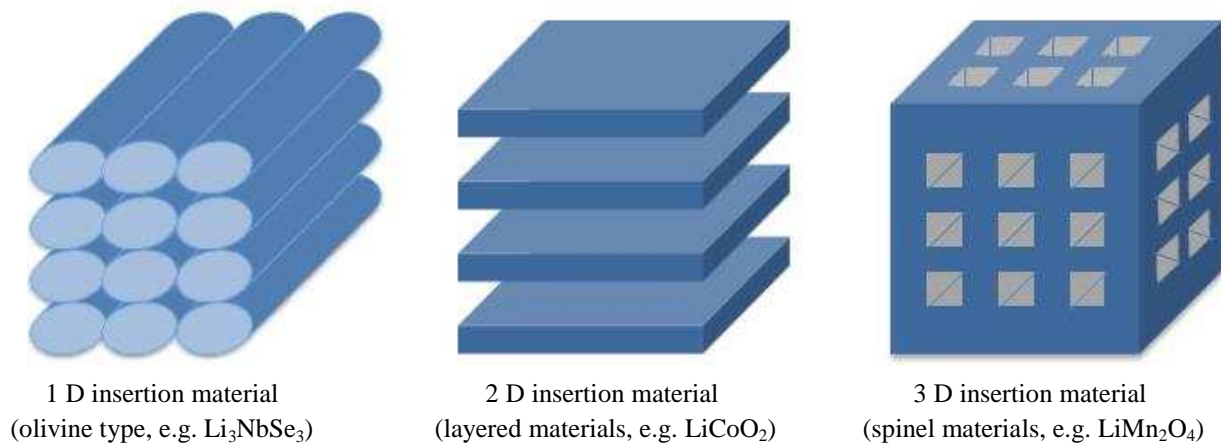


Figure 12: Different types of insertion materials for the positive electrode of lithium-ion batteries [43]

A further possibility for dividing cathode materials is according to their working potential range:

Table 4: Overview over possible active materials for the positive electrode [43]

<b>“5 – Volt”</b>	$x\text{Li}_2\text{MnO}_3/(1-x \text{LiMO}_2)$	layered composite
	(M = Mn, Ni, Co, Cr)	mixed insertion-/displacement type
	$\text{LiMnPO}_4, \text{LiCoPO}_4$	3D olivine-type, insertion-type
	$\text{Li}_2\text{M}_x\text{Mn}_{4-x}\text{O}_8$ (M = Fe, Co)	3D spinel, insertion-type
<b>“4 – Volt”</b>	$\text{LiCoO}_2$	2D layered, insertion-type
	$\text{LiNiO}_2$	2D layered, insertion-type
	$\text{LiMn}_2\text{O}_4$	3D spinel, insertion-type
	$\text{LiNi}_{0.33}\text{Mn}_{0.33}\text{Co}_{0.33}\text{O}_2$	2D layered, insertion-type
	$\text{LiFePO}_4$	3D olivine, insertion-type
<b>“3 – Volt”</b>	$\text{V}_2\text{O}_5$	2D layered, insertion-type
	$\text{MnO}_2$	3D composites, insertion-type

Subsequently, the most common active materials for the cathode should be discussed briefly.

### 3.2.1. Layered oxide cathodes

One of the most dominant cathode materials at this time is  $\text{LiCoO}_2$ , although there is limited availability of cobalt. Goodenough recognized the layered structure of  $\text{LiCoO}_2$  and that lithium ions could be removed electrochemically in a reversible manner. The oxygen atoms are arranged in a close-packed cubic structure and when lithium ions are removed, the oxygen layers rearrange themselves to give hexagonal close packing in  $\text{CoO}_2$ .

The theoretical capacity of  $\text{LiCoO}_2$  is  $274 \text{ mAh g}^{-1}$ , but practically this capacity could not be achieved due to irreversible structural changes of the material. Therefore, the cut-off voltage is limited to  $4.2 \text{ V vs. Li/Li}^+$  to give a capacity of about  $135 \text{ mAh g}^{-1}$ . The advantages of  $\text{LiCoO}_2$  as active material for the cathode are good cycling stability, high energy density and low self discharge. The disadvantages are safety issues (oxygen release), costs and low abundance of cobalt [41] [43] [44].

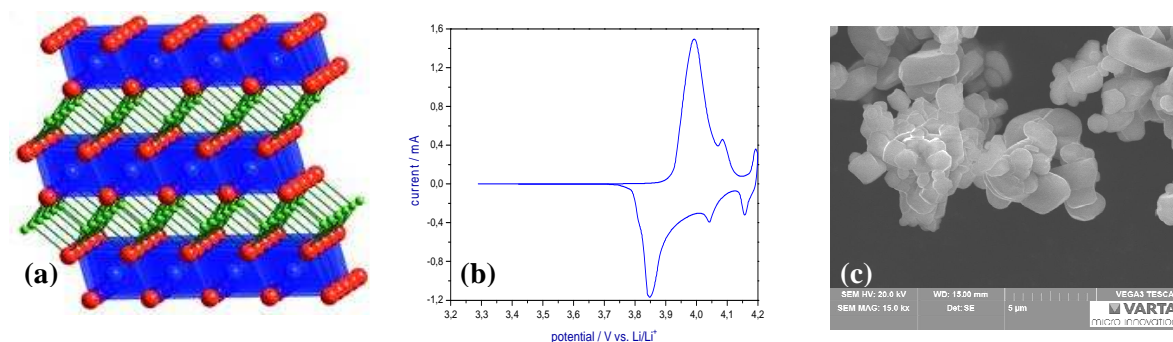


Figure 13: Two-dimensional crystal structure of  $\text{LiCoO}_2$  (a) [45], cyclic voltammogram of a  $\text{LiCoO}_2$  electrode (b) and SEM image of  $\text{LiCoO}_2$  powder (c)

It's possible to replace cobalt by other transition metals to form a layered structure of  $\text{LiNi}_{1/3}\text{Mn}_{1/3}\text{Co}_{1/3}\text{O}_2$ . This material has almost the same theoretical capacity as  $\text{LiCoO}_2$  and can be charged to  $4.5 - 4.6 \text{ V}$ . Cobalt stabilizes the structure in a strictly two-dimensional fashion and the reason for addition of manganese is reduction of costs. The advantages of this material compared to  $\text{LiCoO}_2$  are higher capacities, better overcharge resistance (safety concerns) and lower cobalt content. Among the disadvantages are the poor rate capability and the increasing nickel price [41] [44].



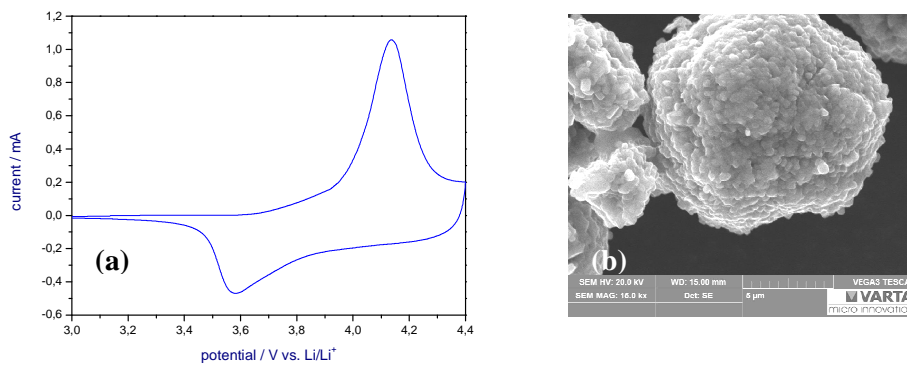


Figure 14: Cyclic voltammogram of a  $\text{LiNi}_{1/3}\text{Mn}_{1/3}\text{Co}_{1/3}\text{O}_2$  electrode (a) and SEM image of  $\text{LiNi}_{1/3}\text{Mn}_{1/3}\text{Co}_{1/3}\text{O}_2$  powder (b)

### 3.2.2. Spinel oxide cathodes

Spinel oxide cathodes are associated with three-dimensional host materials, which have cross-linked channels, allowing ion insertion. This structure has the advantage, that co-insertion of bulky species, such as solvent molecules, could be avoided because of steric reasons. It is subject to a smaller degree of expansion/contraction during lithium-ion storage and extraction. Manganese oxides are the most prominent 3D insertion material for the cathode [43].

$\text{LiMn}_2\text{O}_4$  works reversible in the +4 V vs.  $\text{Li/Li}^+$  potential range and could reach a limited practical capacity of  $120 \text{ mAh g}^{-1}$ . At lower potentials (3 V range),  $\text{LiMn}_2\text{O}_4$  undergoes irreversible structural changes and exhibits rapid capacity fade. But even with a limited capacity,  $\text{LiMn}_2\text{O}_4$  tend to be subject of capacity fade in the 4 V region at elevated temperatures ( $>40^\circ\text{C}$ ). Some disadvantages of this material are Jahn-Teller distortion under non-equilibrium cycling conditions or the dissolution of manganese. These effects are suggested to be source of capacity fade [40] [41] [43].

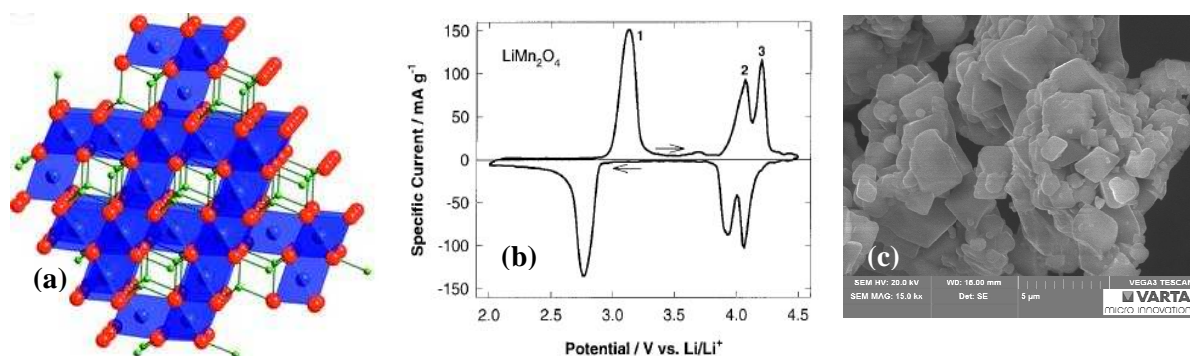


Figure 15: Crystal structure of spinel oxide [45] (a), cyclic voltammogram of a  $\text{LiMn}_2\text{O}_4$  electrode [43] (b) and SEM image of  $\text{LiMn}_2\text{O}_4$  powder (c)

### 3.2.3. Oxide cathodes with polyanions

Among these types of cathode materials for LIBs,  $\text{LiFePO}_4$  is a promising candidate. It crystallizes in the olivine structure and exhibits a flat discharge voltage of around 3.3 V vs.  $\text{Li/Li}^+$ . However, this material has several advantages compared to the previous described cathode materials. No oxygen release occurs during discharge, the charge cut-off potential is well below electrolyte oxidation and it shows excellent cycle- and calendar life. Additionally, iron is inexpensive, non-toxic and environmentally benign. Unfortunately, it has also disadvantages like its low conductivity, low cell voltage and low energy density [40] [41].

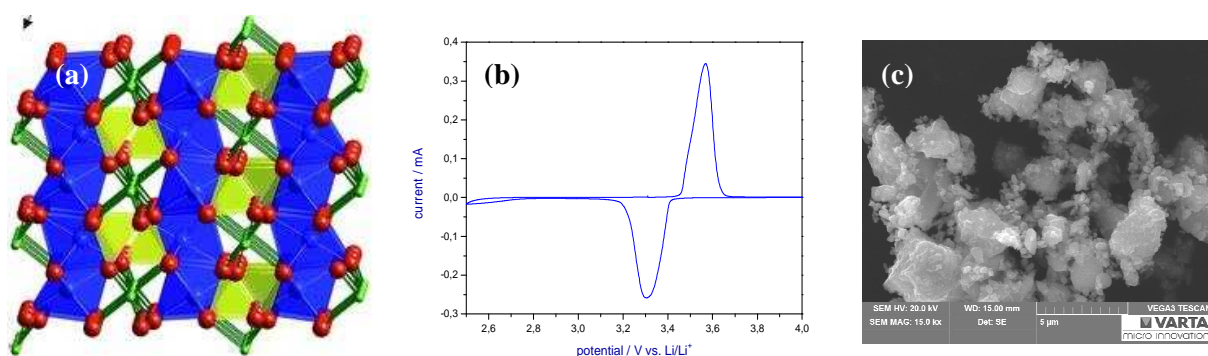


Figure 16: Crystal structure of  $\text{LiFePO}_4$  (a) [45], cyclic voltammogram of a  $\text{LiFePO}_4$  electrode (b) and SEM image of the powder (c)

### 3.3. MATERIALS FOR THE NEGATIVE ELECTRODE

Due to its high energy density and low atomic weight, lithium metal is one of the most suitable anodes for lithium batteries. However, the dendritic deposition of lithium during cycling results in a continuously increasing and highly reactive surface area of the lithium electrode. When the dendrites reach the positive electrode, safety problems occur, leading to internal short-circuit and cell failure. This problem could be solved by implementation of insertion compounds for the negative electrode. Since these batteries contain no metallic lithium, they are much safer than lithium batteries [46].

### 3.3.1. Carbon as insertion material for the negative electrode

The most prominent material for the negative electrode in LIBs is carbon in various modifications. The mechanism behind lithium insertion into graphite is well understood. Carbon based anodes exhibit higher specific charges and more negative redox potentials than most metal oxides. They show better dimensional stability and therefore better cycling performances compared to lithium alloys. Other advantages are the relatively low costs of carbon, the excellent reversibility for lithium insertion and the formation of a protective surface film with many electrolyte solutions [43] [46].

The reversible intercalation of lithium into carbon proceeds according to the following reaction equation, where the maximum uptake is one lithium ion per six carbon atoms ( $\text{LiC}_6$ ):



Within carbon materials, a distinction can be made between graphitic and non-graphitic carbons. Graphitic carbons possess a layered structure with disordered domains, where non-graphitic carbons are highly disordered. Non-graphitic carbons are often produced by pyrolysis of polymers or hydrocarbon precursors at temperatures below 1500°C. Among these precursors two types can be distinguished: graphitizing carbons and non-graphitic carbons. Graphitizing carbons, also called “soft carbons”, develop the graphite structure during heat processes above 1500°C. It has movable carbon layers and at high temperatures, graphite-like crystallites are formed. The other type of non-graphitic carbon is called “hard carbon”. Here, the carbon layers are immobilized by crosslinking and they are not able to develop the graphitic structure even at very high temperatures (up to 3000°C) [43].

The intercalation of lithium ions between the graphene layers is a stepwise process, called stage formation. This means that at low lithium ion concentration a periodic array of unoccupied layer gaps is formed stepwise. This thermodynamic phenomenon is a compromise between the energy required for expansion of the van der Waals gap between two graphene layers and repelling forces between two guest species with the same kind of charge. It was found, that there are existing five stages (figure 17) [43].

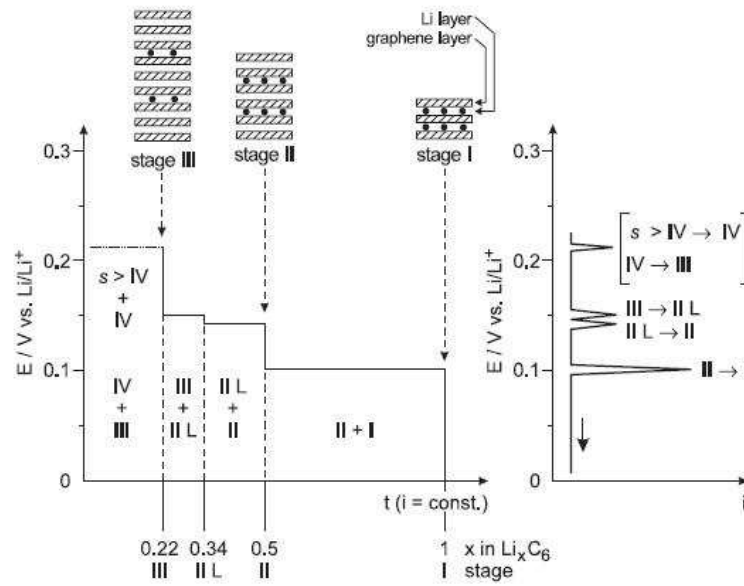


Figure 17: Representation of stage formation during electrochemical intercalation of lithium into graphite [43]

In general, lithium intercalation into graphite is reversible. Due to corrosion processes and formation of a protective film, called solid electrolyte interphase (SEI, see section 3.6.) lithium ions are irreversible consumed during the first charge – step [43] [47].

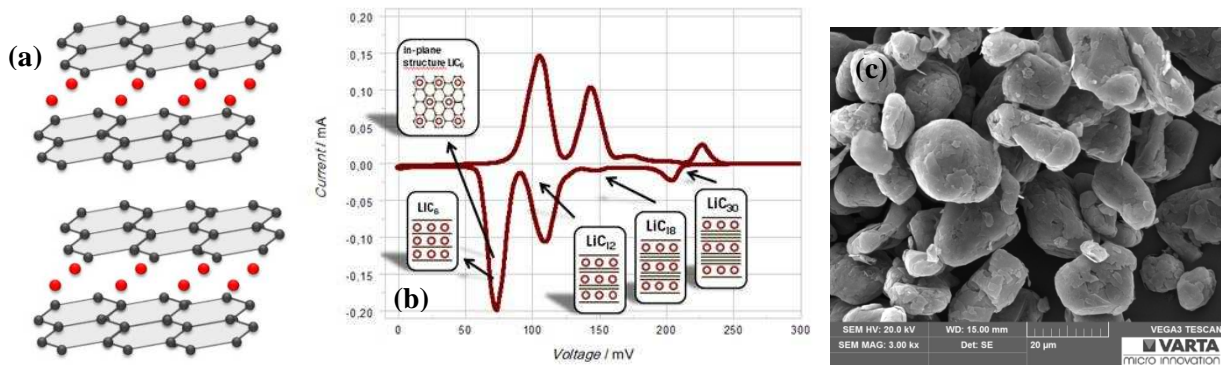
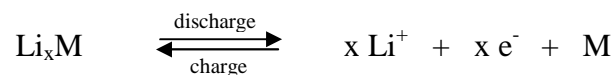


Figure 18: Schematic representation of lithium intercalation into graphene layers (redrawn from [43]) (a), cyclic voltammogram of a graphite electrode [48] (b) and SEM image of the powder (c)

### 3.3.2. Lithium alloys as negative insertion electrode material

To obtain a noticeable improvement in the specific capacity of lithium-ion batteries, carbonaceous anodes have to be replaced by anodes having capacity in the order of 1000-1200 mAh g<sup>-1</sup>. It was found that the total cell capacity of a LIB could be increased, until the capacity of the anode reaches 1200 mAh g<sup>-1</sup>. This is valid for batteries with the same cathode material. After reaching this capacity the improvement becomes negligible [49].

A class of promising anode materials are alloy anodes since they exhibit high capacities and good safety characteristics. Silicon and tin are known as the most promising elements, which are able to undergo reversible lithium alloying. They can be lithiated up to a stoichiometry of Li<sub>4.4</sub>Sn/Si with specific capacities of ~900 and ~4200 mAh g<sup>-1</sup> respectively [37] [50] [51].



A major drawback of lithium alloy anodes is their huge volume expansion of up to 300% during lithiation. This mechanical stress leads to deterioration of the integrity of the active mass followed by tremendous capacity fade. Additionally, surface films are formed, which are important for achieving passivation. But the volume expansion in every charge/discharge step allows no maintenance of a stable passivation layer, hence irreversible charge consumption proceeds with each cycle [37] [50] [51].

#### 3.3.2.1. Silicon for lithium alloying

Due to its abundance and huge lithiation capacity, Si is considered to be the most promising material for alloy anodes. The highest lithiated phase achievable is Li<sub>22</sub>Si<sub>5</sub> with a corresponding capacity of 4200 mAh g<sup>-1</sup>. However, Obravc et al. showed, that the highest lithiated silicon phase at ambient temperature is Li<sub>15</sub>Si<sub>4</sub> with an achievable capacity of 3579 mAh g<sup>-1</sup> [49] [52]. Beside this phase, a few other lithium-silicon alloys are known, which are listed in table 5. For practical use of silicon anodes, the capacity must be limited during cycling to avoid huge volume expansion, which can't be accommodated by conventional composite electrodes.

Limiting the lithiation of amorphous silicon above 50 mV, the silicon remains amorphous, whereas lithiation below 50 mV results in crystallization of the  $\text{Li}_{15}\text{Si}_4$  phase [52].

Table 5: Properties of different lithiated silicon phases [49] [53]

Compound	Crystal structure	Specific capacity [mAh g <sup>-1</sup> ]	Potential range [mV]	Volume per silicon atom Å <sup>3</sup>
Silicon	cubic			20.0
$\text{Li}_{12}\text{Si}_7$ ( $\text{Li}_{1.71}\text{Si}$ )	orthorhombic	1636	332-288	58.0
$\text{Li}_{13}\text{Si}_6$ ( $\text{Li}_{2.17}\text{Si}$ )	rhomboidal	2227	288-158	51.5
$\text{Li}_{13}\text{Si}_4$ ( $\text{Li}_{3.25}\text{Si}$ )	orthorhombic	3101	158-44	67.3
$\text{Li}_{22}\text{Si}_5$ ( $\text{Li}_{4.4}\text{Si}$ )	cubic	4199	44-2	82.4

Silicon alloy anodes show high initial irreversible capacities. The reasons are considered to be the following [50]:

1. The large volume change during lithiation and delithiation causes cracking and pulverization of active material and leads to loss of conductive pathways for lithium ions. The consequence is disconnection from the current collector and loss of active material. This leads to a sharp rise of internal resistance of the anode with uncompleted delithiation reaction.
2. Due to the constant volume changes, the formation of the solid electrolyte interphase (SEI, section 3.6.) is a dynamic process, which means loss of active material and electrolyte during every cycle. Therefore it contributes to capacity fade during cycling.
3. The irreversible trapping of lithium ions due to slow Li release kinetics or formation of highly stable lithiated compounds may result in irreversible capacity loss.

It was found, that nanostructured silicon could accommodate the volume change during lithiation in the best way. The choice of the right binder for electrode preparation is also of great importance as well as the addition of an active or inactive host matrix to mitigate the volume expansion [37] [51]. Such a host matrix must be conductive for electrons and lithium ions, it should support the structural stability of the whole electrode and it should help to reduce the agglomeration of active particles during cycling [50].

### 1. *Inactive host matrix*

This type of composite comprises of active material in an electrochemically inert matrix like Fe, Cu, Al<sub>2</sub>O<sub>3</sub>, TiN or SiC. It is expected, that the addition of an inactive host matrix could improve cycling stability and mechanical stability of the alloy anode at a price of reduced specific capacity. Another potential disadvantage is that the inactive matrix may block or slow down lithium diffusion kinetics or electron transfer [50].

### 2. *Active host matrix*

Here, both the active particles and the host matrix are able to become lithiated. A very promising approach is the development of carbon-based composites. They can be prepared by ball milling of silicon with graphite and/or carbon black or by pyrolysis of carbon precursors [49]. Silicon-carbon composite active materials exhibit better cycling performance compared to silicon without host matrix. This is attributed to the improved electronic and ionic conductivity of carbon and the buffering effect of carbon to accommodate the volume expansion to ensure mechanical stability of the electrode. But the embedding of silicon particles into a carbon host matrix comes at a price of reduced specific capacity [50].

### 3.3.3. **Other intercalation compounds for the anode**

Beside graphite, a few other transition metal oxides, phosphides or chalcogenides have been investigated as anode hosts. Typically, these materials show rather low specific charges and cell voltages, if combined with an oxidic positive electrode. Among them, Li<sub>4</sub>Ti<sub>5</sub>O<sub>12</sub> (LTO) is the most important intercalation compound of this anode types. The capacity of LTO is around 150 – 160 mAh g<sup>-1</sup> at a potential of 1.5 V vs. Li/Li<sup>+</sup>. Because of the low specific capacity and high voltage vs. Li, this material possesses a relatively low energy density compared to graphite. However, LTO is very fast and could be charged and discharged at high rates and there are no passivation phenomena and passivating films needed to ensure the structural stability of this anode host material. Other advantages of LTO are an excellent low temperature performance and a very prolonged cycle life. These properties open the door for load-leveling lithium-ion battery technologies based on intercalation materials [37], [40], [43].

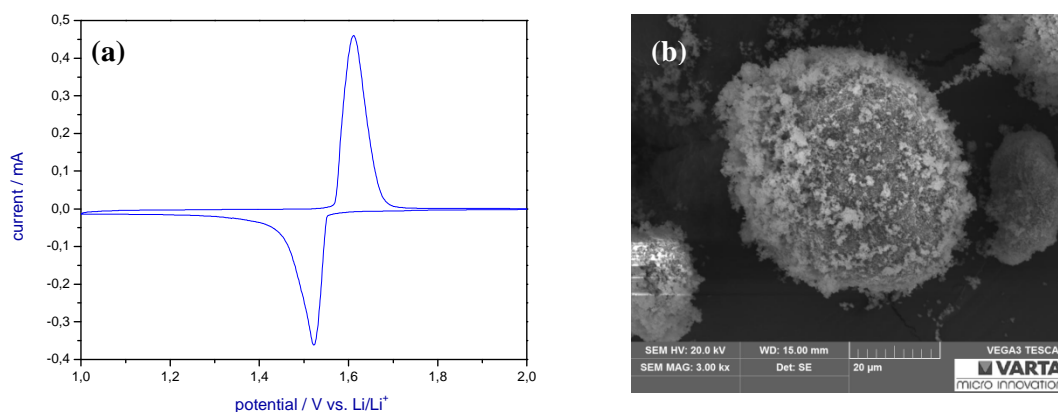


Figure 19: Cyclic voltammogram of a  $\text{Li}_4\text{Ti}_5\text{O}_{12}$  electrode (a) and SEM image of the powder (b)

### 3.4. CURRENT COLLECTORS IN LITHIUM-ION BATTERIES

Traditionally, electrodes are composed of a flat metal foil as current collector, which is loaded with active material through roll coating methods. Due to its low price, good electric conductivity and the ability to form a protective passive layer, aluminium is the metal of choice for high voltages ( $>3.5$  V vs.  $\text{Li}/\text{Li}^+$ ). The application of aluminium foil as current collector for the negative electrode is hindered because of the formation of  $\text{Li-Al}$  alloy at potentials close to 0 V vs.  $\text{Li}/\text{Li}^+$ . Therefore, a copper foil is established as current collector for the negative electrode [2].

Especially, for the application in electric vehicles it is necessary, to reduce cost, size and volume of lithium-ion batteries and to increase the total energy stored in the battery. This could be achieved through reduction of inactive components in LIBs and increased thickness of electrode coating. However, the traditional architecture of lithium-ion cells on flat current collectors does not allow an increased mass loading due to a few difficulties, like delamination of the coated material or the difficulty of electrolyte penetration through a thick electrode, which dramatically increases the cell impedance [5] [6].

This leads to the concept of three-dimensional battery architecture. Several examples for the development of 3D current collectors can be found in literature. Examples of 3D current collectors include the development of nanotube forests grown on metal current collectors [7], porous metal or carbon foams [5] [54] or conductive textiles [6] (figure 20).



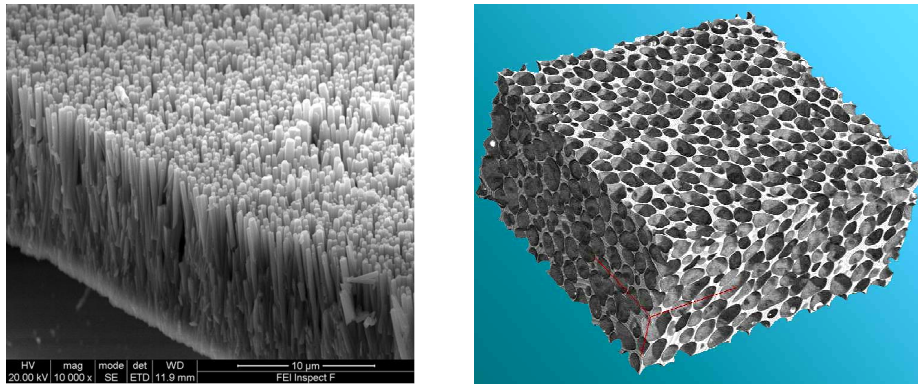


Figure 20: Forest of nanotubes grown on metal sheets (left) [55] and porous metal foam as current collector for LIBs (right) [56]

The advantages of 3D current collectors over traditional 2D current collectors are a reduced demand of metal (sustainability), possibility of higher mass loadings, weight diminution, improved mechanical stability and better rate capability of the electrode due to the higher surface area, which means higher contact area between active material and current collector.

### 3.5. COMMON ELECTROLYTES

Apart from the various characteristics of the insertion materials discussed previously, several other criteria are important in designing a lithium-ion cell that can offer high performance with long cycle life. The role of the electrolyte is to serve as a medium for ion transfer between a pair of electrodes.

In most cases the electrolyte is a solution, which consists of salts dissolved in an appropriate organic (nonaqueous) solvent [57].

An electrolyte should meet the following requirements [57]:

- good ionic conductivity but electronically insulating (to keep the self-discharge to a minimum)
- wide electrochemical window (electrolyte decomposition should not occur within the range of the working potentials of the electrodes)
- it should not react with other cell components like separators or electrode substrates
- it should be robust against electrical, mechanical or thermal stresses
- the components should be environmentally friendly

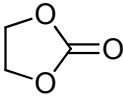
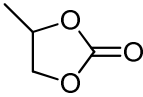
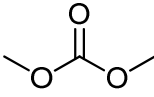
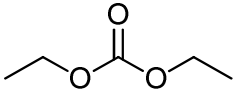
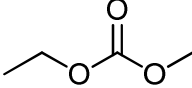
Electrolytes for lithium-ion batteries can be (a) solutions of one or more lithium salts in mixtures of one or more organic solvents with different properties, (b) solid polymer or gel polymer electrolytes or (c) ionic liquids. Since organic solvents are commonly used in LIBs, this type of electrolyte should be discussed here more in detail [57].

There are different demands on the electrolyte solvent for application in LIBs, which can hardly be met by just one component. Therefore, a mixture of different solvents and salts is normally used [57]:

- The electrolyte solvent should be able to dissolve salts in a sufficient concentration (solvent with a high dielectric constant  $\epsilon$ ).
- The viscosity should be low enough to ensure facile ion transport.
- The solvent should be inert to all cell components.
- The boiling point should be high and the melting point low because the solvent should remain liquid in a wide temperature range.

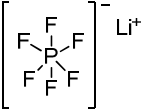
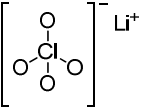
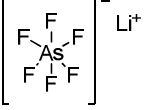
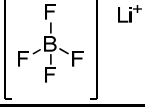
All these requirements can be met by the introduction of ethers and esters as electrolyte solvents. In general, linear carbonates possess lower viscosities, lower boiling points and lower dielectric constants compared to cyclic carbonates. The most common electrolyte solvents are depicted in table 6.

Table 6: Organic electrolyte solvents for LIBs and their properties [57]

Solvent	Structure	m. p. [°C]	b. p. [°C]	$\epsilon$ (20°C)	$\eta$ [cPa] (25°C)
<b>Cyclic carbonates</b>					
Ethylene carbonate (EC)		36	238	95	1.9
Propylene carbonate (PC)		-54	242	65	2.5
<b>Linear carbonates</b>					
Dimethyl carbonate (DMC)		3	90	3.1	0.59
Diethyl carbonate (DEC)		-43	127	2.8	0.75
Ethyl methyl carbonate (EMC)		-55	107	2.9	0.65

m.p....melting point, b.p....boiling point,  $\epsilon$ ...dielectric constant,  $\eta$ ...viscosity

Table 7: Common lithium salts for electrolytes in LIBs and some of their properties [57]

Salt	Structure	m. p. [°C]	$T_{\text{decomposition}}$ [°C]	$\sigma$ [mS cm <sup>-1</sup> ] (1 M, 25°C) in EC/DMC
LiPF <sub>6</sub>		200	80	10.7
LiClO <sub>4</sub>		236	> 100	8.4
LiAsF <sub>6</sub>		340	> 100	11.1
LiBF <sub>4</sub>		293	> 100	4.9

m.p....melting point,  $\sigma$ ....conductivity

The use of possible lithium salts is limited through a few requirements. They should be sufficiently soluble in the mixture of carbonates, they must not react with the nonaqueous solvents and they must not cause corrosion of other cell components, like separators or metallic packing materials. The used lithium salts should help to form a protective layer on the surface of the current collector, especially on the cathode side. Table 7 lists some examples of common lithium salts used as electrolytes. Among these salts,  $\text{LiPF}_6$  is applied in commercially available lithium-ion batteries due to its oxidation resistance up to 5.1 V, its ability to passivate aluminium current collector and its advantage to form a stable SEI [57].

### **3.6. ELECTRODE/ELECTROLYTE INTERFACES – SOLID ELECTROLYTE INTERPHASE (SEI)**

It was found that a protective film is formed on the negative electrode of lithium-ion batteries during the first charging through reductive decomposition of the electrolyte solution. When a certain thickness is reached, this film protects the surface of the electrode from further corrosion and the decomposition of electrolyte on the electrode's surface is stopped. This surface film is called "solid electrolyte interphase" (SEI) and this phenomenon occurs not only on lithium metal electrodes but also on negative lithium insertion electrodes [43] [58].

The composition of the SEI strongly depends on the electrolyte used and not every organic solvent is able to form stable, insoluble decomposition products. Some studies have shown that the choice of an appropriate mixture of solvents, additives and salts is critical to benefit from the advantages of the SEI [59]. This layer allows lithium ion diffusion but blocks electron transport or co-intercalation of solvent molecules in between the graphite layers and hinders the associated destruction of the negative intercalation electrode. In literature, it is suggested that the SEI layer consists of a mixture of several phases: an inner part with inorganic compounds such as  $\text{Li}_2\text{O}$ ,  $\text{LiF}$  or  $\text{Li}_2\text{CO}_3$  and an outer organic part, dominated by semicarbonates, polyolefins, lithium alkyl carbonates ( $\text{R-OCO}_2\text{Li}$ ) and lithium alkoxides ( $\text{R-OLi}$ ) [60] [61] [62] (figure 22). Ethylene carbonate (EC) is considered to play an important role during SEI formation. It is assumed that EC is reduced during the first cycle within the voltage range of 0.3 and 0.8 V vs.  $\text{Li/Li}^+$  at the graphite electrode leading to ethylene gas evolution at the surface of the electrode accompanied by  $\text{Li}_2\text{CO}_3$  formation [47].

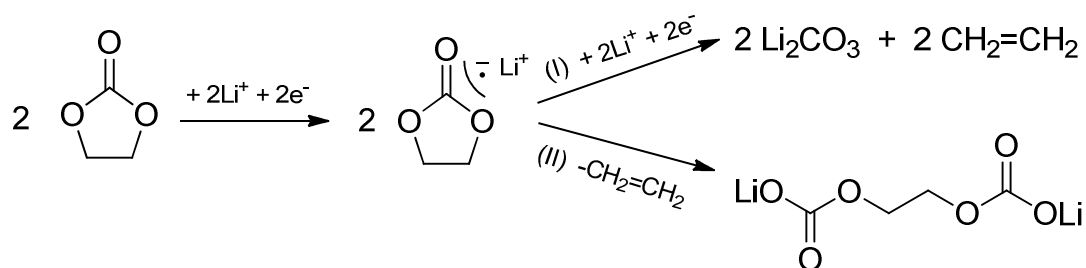


Figure 21: Mechanism of electrochemically induced reduction of EC [63]

Figure 21 shows possible mechanisms, which are present during SEI formation. Mechanism (I) leads to formation of more gaseous products and predominant generation of  $\text{Li}_2\text{CO}_3$  results in a less stable SEI. The products of mechanism (II) are almost insoluble in the electrolyte and here, less gaseous products are formed. Both mechanisms compete with each other and they are affected by the morphology and chemistry of graphite surface [63].

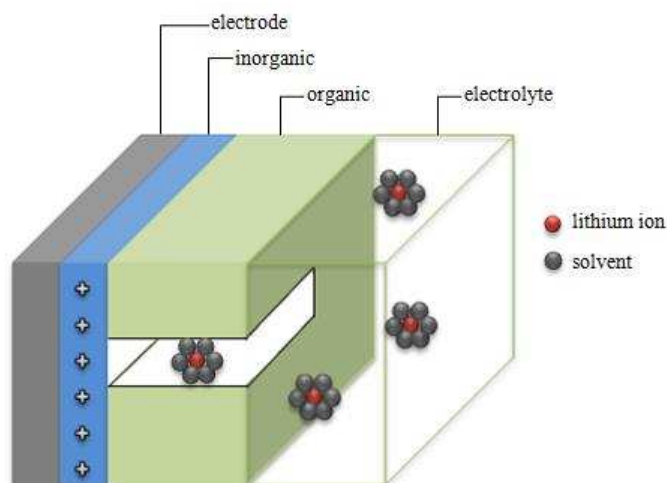


Figure 22: Schematic drawing of different films forming on an anode in organic electrolytes (SEI) (redrawn)

It is proposed that the SEI is neither ionic conductive nor electronic conductive and it is believed, that the ionic conduction in the SEI must originate from the movement of  $\text{Li}^+$ -ions through the micro-pores of the SEI. Therefore, the compactness and stability of the SEI can be determined through measurement of the ionic conductivity [64].

Electrolyte additives can influence the quality of the SEI and are able to significantly improve the cycleability and cycle life of LIBs. Usually, the amount of an additive in the electrolyte is not more than 5%. The purposes of electrolyte additives are [63]:

- enabling formation of solid electrolyte interphase on the surface of graphite
- reduction of irreversible capacity and gas formation and long term-cycling
- enhancement of the thermal stability of  $\text{LiPF}_6$
- protection of cathode material from dissolution and overcharge

Most additives with the purpose of improving the quality of the SEI have higher reductive potentials than the electrolyte solvents. During electrochemical reduction, the additives are preferably reduced to form insoluble solid products on the surface of the anode to deactivate catalytic activity, leading to less gas formation and an increased stability of the SEI. These additives can be divided in polymerisable monomers and reductive agents. The most prominent SEI forming additive is polymerisable vinylene carbonate (VC). Figure 23 shows a general equation of the mechanism of electrochemically induced polymerization [63]:

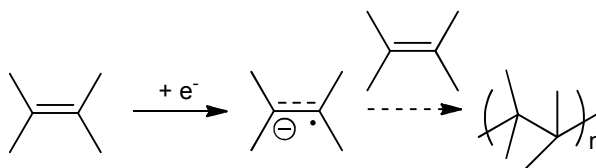


Figure 23: General equation of the mechanism of electrochemically induced polymerization of polymerisable monomer additives

Generally, the morphology, thickness and composition of the SEI depend on the composition of the electrolyte, type of electrode, temperature and applied current density. Because of its remarkable importance for stability of the negative electrode and consequently long cycle life, many efforts have been made to investigate the SEI.

Fourier transform infrared spectroscopy (FTIR), x-ray photoelectron spectroscopy (XPS), mass spectroscopy (e.g. TOF-SIMS) or atomic force microscopy (AFM) are some available techniques for studying composition and thickness of the SEI layer [62] [65].

Despite its great importance for the stability of the negative electrode, SEI formation is a predominant source of lithium ion loss in LIBs [66]. Beside this, several degradation mechanisms are known, which will adversely affect the durability of lithium-ion batteries. The various battery components can undergo different aging mechanisms like decomposition of binder and electrolyte, corrosion of current collector, structural disordering of the cathode or separator melting. Ageing effects like self-discharge or impedance rise occur during storage and will affect the calendar life, whereas ageing effects like mechanical degradation or lithium metal plating may occur during use, which will affect the cycle life of the battery [67] [68].

Especially carbonaceous anodes are susceptible to undergo a multitude of aging mechanisms that negatively affect the electrochemical performance of LIBs (figure 24) [67]:

➤ *Surface layer formation*

SEI formation as well as formation of other passivating surface layers will contribute to the irreversible loss of capacity during cycling. It is considered to be the main source of loss of mobile lithium, increase in charge transfer resistance and cell impedance [67].

➤ *Loss of lithium ions*

Beside SEI-formation and irreversible lithium-ion trapping in the host material, lithium-ion loss is attributed to side reactions of lithium with decomposed electrolyte compounds and traces of water in the electrolyte [67].

➤ *Metallic lithium plating*

Lithium plating on the surface of the anode will be initiated by several factors. For example it is supported by a high content of EC in the electrolyte. Also, a high cathode capacity compared to anode capacity promotes lithium plating as well as low operating temperatures (below -20°C) and high charge rates [67].

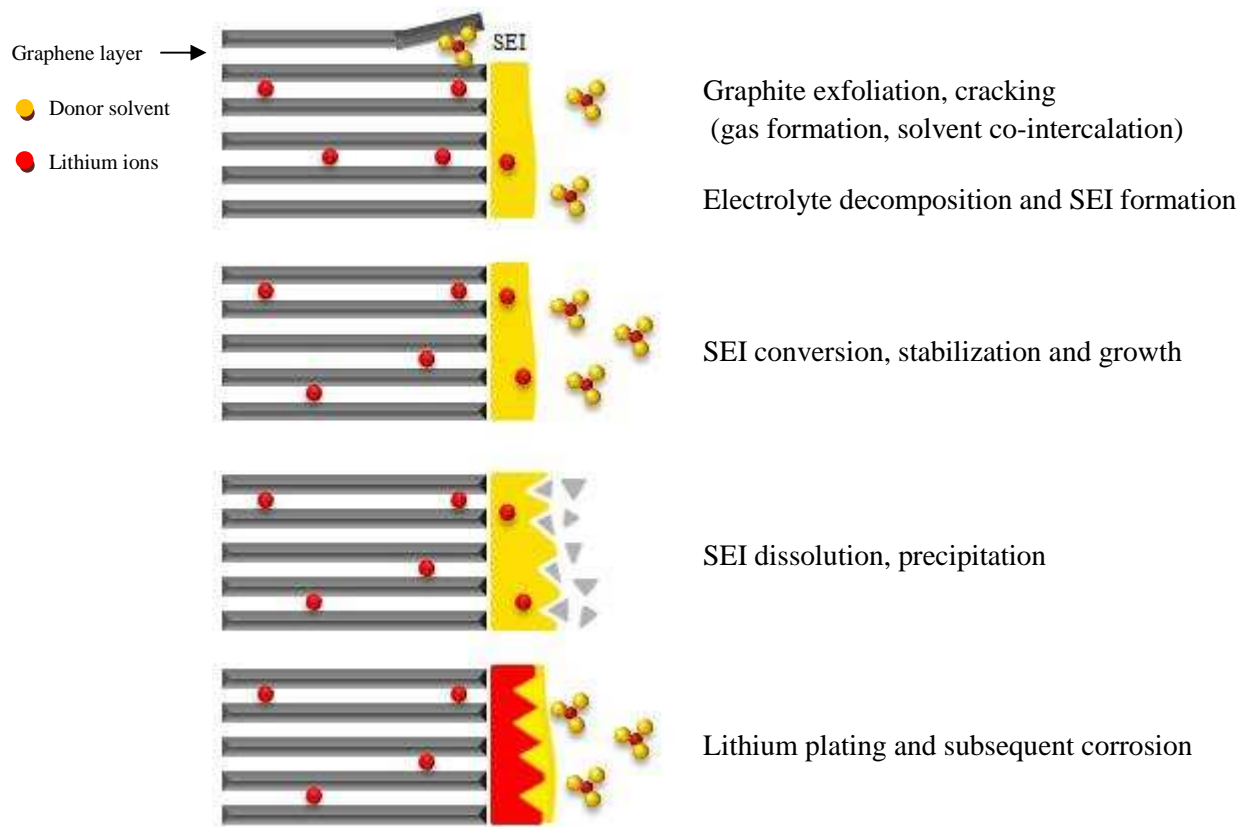


Figure 24: Changes at the anode/electrolyte interface / aging mechanisms (redrawn from [68])

In conclusion, many factors are responsible for power fading, cell impedance and capacity decay of batteries and these ageing mechanisms will be accelerated at high temperatures. Material parameters and surface chemistry as well as cycling and storage conditions are of great importance for the performance and life time of a lithium-ion battery [68] [69].



## 4. EXPERIMENTAL

### 4.1. MEASUREMENT METHODS AND SETUPS

This section should give a brief overview over several applied electrochemical and analytical techniques, used in this work for the characterisation of prepared cell compounds.

#### ➤ *Electrochemical characterisation*

The cyclic voltammetry experiments were performed with a potentiostat/galvanostat (Biologic MPG2) at 293 K and a scan rate of  $30 \mu\text{V s}^{-1}$ . The long term cycling tests and rate capability tests were performed with a MACCOR Series 4000 battery tester at 293 K.

All half-cell electrochemical experiments were performed in a 3 electrode Swagelok<sup>®</sup>-T-cell using metallic lithium as reference- and counter electrode (figure 25a) and full-cell experiments were performed using pouch bag cell design (figure 25b). A non-woven polypropylene separator (Freudenberg FS2226) was used to separate the working electrode from lithium counter- and reference electrode in Swagelok<sup>®</sup>-T-cells and a monolayer polypropylene membrane separator (Celgard<sup>®</sup> 2400) was used in pouch bag cells. As electrolyte a mixture of ethylene carbonate (EC) and diethyl carbonate (DEC) (EC/DEC 3:7 v/v) with 1 M LiPF<sub>6</sub> as conducting salt and 2 wt% vinylene carbonate (VC) as additive was used. All test cells were assembled in an argon-filled glove box.

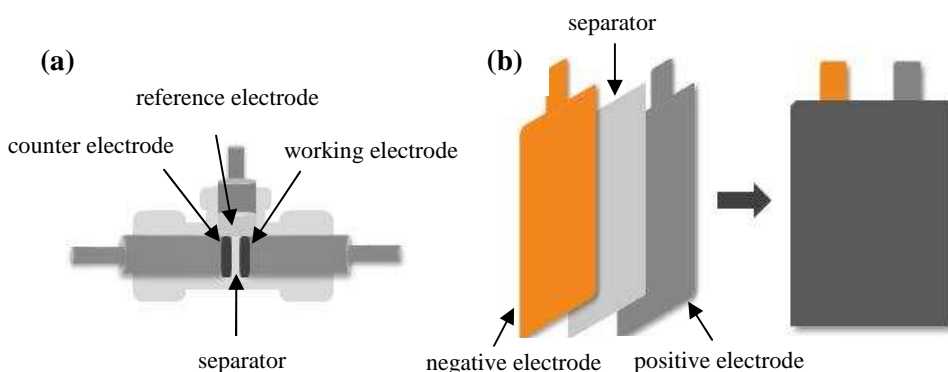


Figure 25: Schematic drawing of a Swagelok-T-cell (a) and a pouch bag cell (b)

The electrodeposition was performed using an Autolab PGSTAT 100 & 10 A Booster under inert gas conditions. The deposits were obtained operating in current controlled (galvanostatic) conditions at different temperatures, using pure aluminium rods (Goodfellow 99,999%) as counter and reference electrodes.

As substrates for electrodeposition, nickel plated non-woven polymer with dimensions of 20 mm x 20 mm x 0.15 mm was used. The determination of the electrochemical stability window of EMImCl\*1.5 AlCl<sub>3</sub> was performed using a Biologic Potentiostat VMP 3 under inert gas conditions at room temperature, using glassy carbon as working electrode (BAS Inc. Tokyo, 6.0 mm x 3.0 mm) and platinum as reference- and counter electrode (BAS Inc. Tokyo, 6.0 mm x 1.6 mm) with a scan rate of 50 mV s<sup>-1</sup>.

➤ *Scanning electron microscopy (SEM)*

Morphology analysis was performed using a Tescan Vega 3 scanning electron microscope (SEM) equipped with an energy dispersive X-ray detector (Oxford Instruments INCAx-act).

➤ *Head space gas chromatography – mass spectrometry (GC/MS) and Py-GC/MS*

A Frontier Laboratory PY2020iD pyrolyser was directly attached to the injection port of a gas chromatograph (GC, Agilent 7890 A) equipped with a metal capillary column and an Agilent 5975 C VLMSD mass spectrometer as detector. Helium was used as carrier gas. For identification of the decomposition products, the MS system was utilised in electron ionisation mode at 70 eV. The mass scan range was set between  $m/z$  15 and 300. About 10  $\mu$ L of the electrolyte for aluminium deposition was placed in a small sample cup and then inserted into the heated centre of the pyrolyser furnace at 368 K, and this temperature held for 1 h. Afterwards, the pyrolysis technique was switched into the evolved gas analysis (EGA) mode, heating the pyrolyser furnace to 853 K, the decomposition products were transferred into the mass spectrometer continuously. The flow rate was set to 1 mL min<sup>-1</sup>, the heat rate was 20 K min<sup>-1</sup> and the split ratio was 1:100. Headspace GC/MS analysis of the sample head space was carried out using a HP5-MS column (5% phenyl methyl silox Agilent) as stationary phase for separation. The inlet temperature was set to 523 K and the injection was performed manually (split ratio of 1:500). The temperature program started at 313 K, increased to 453 K with 10 K min<sup>-1</sup> held for 1 min. The mass scan range was set between  $m/z$  20 and 100.

➤ *Conductance measurement*

A Knick 703 conductivity meter was used for the determination. The conductivity of the samples was determined within a temperature range of 293 K to 368 K divided into 10 K steps. The cell constant was determined using aqueous 0.1 mol L<sup>-1</sup> NaCl solution. The temperature of the samples was controlled by a Julabo F32 thermostat. The cell for conductivity measurement was assembled in an argon filled glove box and then carefully sealed.

➤ *NMR studies*

The chloroaluminate molten salts were measured with a D<sub>2</sub>O capillary without any solvent and pure EMImCl was dissolved in CDCl<sub>3</sub>. The samples for NMR measurement were prepared in an argon-filled glove box. The <sup>1</sup>H and <sup>13</sup>C NMR spectra were recorded with a Varian Mercury 300 MHz spectrometer using tetramethylsilane as reference, at 300.224 MHz and 75.499 MHz respectively. All NMR spectra were recorded at 298 K.

## **4.2. IMPLEMENTATION OF A 3D CURRENT COLLECTOR FOR THE POSITIVE ELECTRODE OF LIBS**

### **4.2.1. Preparation of the 3D current collector**

For preparation of the 3 dimensional current collectors for the positive electrode of lithium-ion batteries non-woven polyester was used as template. Polyester is a non-conductive polymer and therefore, for successful implementation as current collector, it has to be metallised. There are several methods available for metal plating of non-conductive workpieces like electroless metal deposition, thermal spray coating, hot dipping or physical and chemical vapour deposition (PVD, CVD) [23] [70].

In this work non-woven polymer was coated with copper or nickel by electroless metal deposition followed by aluminium coating through electroplating. As alternative, non-woven polymers was coated with different aluminium layer thicknesses by physical vapour deposition (PVD).

Two generations of non-woven polymer were characterised (figure 26). The first generation refers to a template with less homogeneity compared to the second generation of non-woven polymer. The homogeneity of the current collector is of great importance for determination of the exact mass of the current collector and mass loading of the electrode. The knowledge about the exact mass of an electrode is of great importance for the calculation of the c-rate. The applied rate affects the cycling performance and received capacity of an electrode.

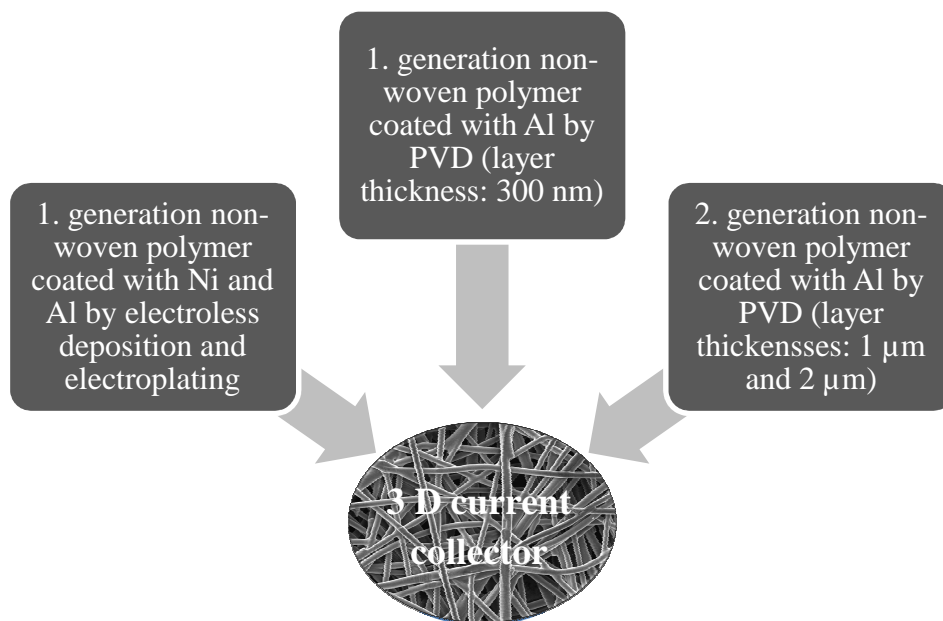


Figure 26: Different kinds of 3 dimensional current collectors – overview

#### 4.2.2. First generation non-woven polymer coated with Ni or Cu by electroless deposition and Al by electroplating

The Cu and Ni-P films were deposited on non-woven PE, with dimensions of 20 mm x 20 mm x 0.15 mm, pre-treated in a basic cleaning solution (Envision™ DPS 5625) at 338 K for 5 min, 30% HCl etching for 60 s at room temperature and PdCl<sub>2</sub> activation for 60 s at 313 K (UDIQUÉ™ 879 W). In between all steps, the substrates were rinsed with deionised water (table 8). Subsequently, Cu and Ni-P films were electroless deposited on the pretreated substrates. Copper films were deposited from baths containing 10 g L<sup>-1</sup> Cu<sup>2+</sup> ions and formaldehyde as reducing agent. The electrolyte for copper deposition was composed of CuSO<sub>4</sub>·5 H<sub>2</sub>O, NaOH and CH<sub>2</sub>O (ENPLATE Cu 872). Operating temperature of the bath was 328 K.

Nickel films were deposited from baths containing  $3.5 \text{ g L}^{-1} \text{ Ni}^{2+}$  ions and sodium hypophosphite as reducing agent. The electrolyte for Ni-P deposition was composed of  $\text{NiSO}_4 \cdot 6\text{H}_2\text{O}$ ,  $\text{NaH}_2\text{PO}_4 \cdot \text{H}_2\text{O}$  and  $\text{NH}_3$  (UDIQUÉ™ 891).

Operating temperature and pH of the baths were 338 K and 9, respectively. Table 8 summarises all single steps with temperature and duration, which are necessary for successful metal reduction on a non-conductive substrate. All baths were supplied by Enthone Cookson Electronics and were used as received without further purification.

Table 8: Steps of electroless metal deposition process with related temperature and time for each step

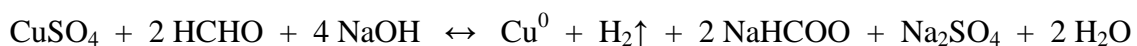
	Procedure	Duration [min]		Temperature [K]	
		Copper	Nickel	Copper	Nickel
1	Cleaner (Envision™ DPS 5625)	5	5	338	338
	Deionised water	1	1	rt	rt
2	Etching (30% HCl)	1	1	rt	rt
3	Activator (UDIQUÉ™ 879 W)	1	1	313	313
	Deionised water	1	1	rt	rt
4	Deposition	4.5	20*	328	338
5	Corrosion protection (for copper only)	1	-	333	-

\* reaction time depends on  $\text{Ni}^{2+}$ -concentration (reaction is faster when bath is freshly prepared)  
rt.....room temperature

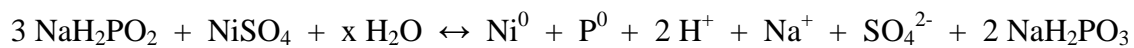
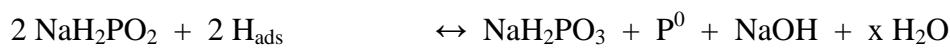
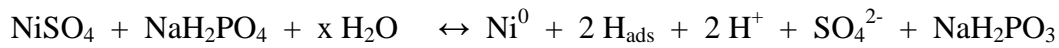
For achievement of a well adherent metal layer on the non-conductive substrate, pretreatment of the surface is essential. Therefore, grease was removed from the surface by treatment in basic solution followed by etching for better adhesion of the metal layer on the polymer. After that, nucleation sites were applied on substrates surface through treatment in acidic  $\text{PdCl}_2/\text{SnCl}_2$ -solution. Finely distributed colloidal palladium was deposited on the substrates surface, which initiated electroless metal deposition [71] [72]:



After activation, the surface is ready for electroless metal plating. Copper can be chemically reduced from basic solution. Formaldehyde delivers electrons for copper deposition and is therefore oxidized [73]:



In most commercially available nickel plating baths, nickel-phosphorous alloys are reduced from alkaline solution with sodium hypophosphite as reducing agent. Deposition of alloys with different phosphorous content is possible (2-14%), depending on the formulation of the plating solution. Reduction and oxidation takes place according to the following reaction equations [74]:



After reduction of both metals on non-woven polymer a dense and well adherent metal layer could be obtained for each metal (figure 27). The desired metal layer thickness could be received by adapting the reaction time.

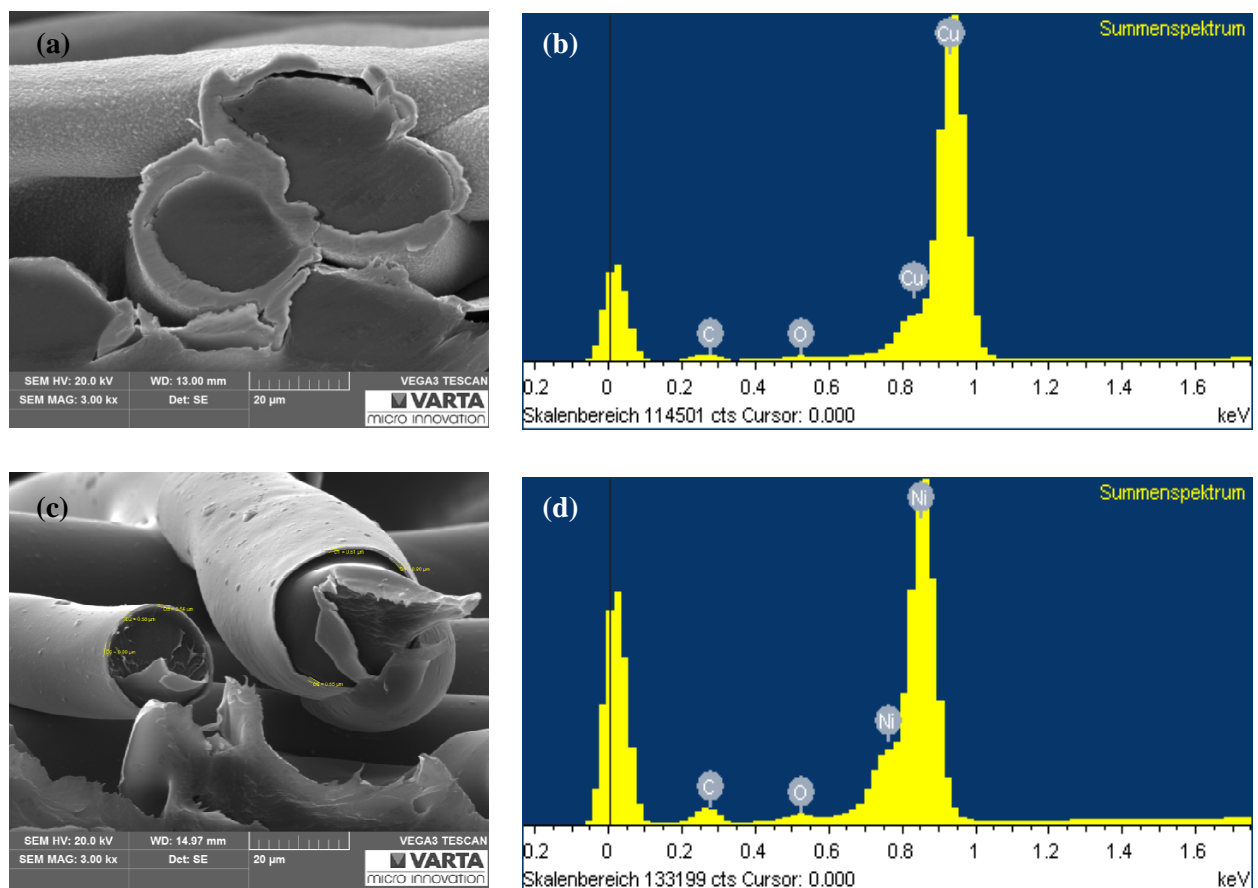


Figure 27: SEM images and EDX spectra of copper plated polymer non-woven (a, b) and of nickel-plated non-woven polymer (c, d)

For electrodeposition of aluminium, the bath was constituted of 1-ethyl-3-methylimidazolium chloride (EMImCl-AlCl<sub>3</sub> molar ratio 1-1.5), supplied by BASF (Basionics™ Al01 [75]), and used as received without further purification. All chemicals were handled under argon atmosphere in a glove box, in which the moisture and oxygen content was maintained below 0.1 ppm. The electrodeposition was performed in an electrochemical cell (100 mL) with three electrodes using an Autolab PGSTAT 100 & 10 A Booster under inert gas conditions. The deposits were obtained operating in current controlled (galvanostatic) conditions at 368 K, using pure aluminium rods (Goodfellow 99,999%) as counter and reference electrodes. As substrates for electrodeposition, the already prepared copper and nickel plated non-woven polymer were used.

Figure 28 illustrates the conductivities of untreated 1-ethyl-3-methyl-imidazolium chloride compared to thermally stressed and electrochemically aged ionic liquid. It was found, that conductivity increases with increasing temperature and reaches about 50 mS cm<sup>-1</sup> at 368 K (figure 28). This is a very low value compared to aqueous electrolytes with thousand-fold higher values. As shown in figure 28, thermal and electrochemical treatment seems to have no significant effect on the conductivity of the electrolyte. Aluminium deposition from EMImCl\*1.5 AlCl<sub>3</sub> at room temperature occurs only slowly and could be explained by the reduced conductivity of the electrolyte at room temperature compared to increased temperatures (figure 28). It should be noted that this behaviour could originate from slow kinetics of electrode reaction itself as well. The resulting aluminium layer and the current yield from electrodeposition at room temperature are very bad.

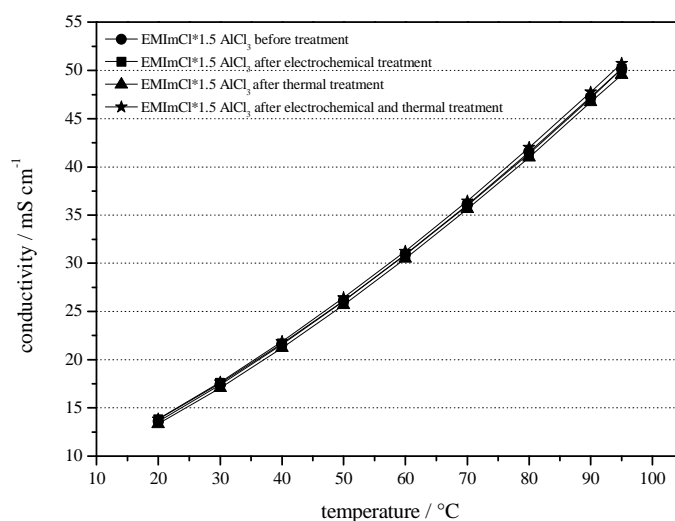


Figure 28: Conductivity measurement of EMImCl\*1.5 AlCl<sub>3</sub>

Another important property of an electrolyte is the electrochemical stability window. The electrochemical window is defined as the potential range between the reduction potential of the cation and the oxidation potential of the anion. Most ionic liquids possess a wide potential window at many electrodes, up to 4-6 V. That makes ILs to promising electrolytes for electrochemical applications [76] [77]. In comparison, the thermodynamic stability window of pure water has a value of only 1.23 V due to limitation through water decomposition [78]. The measurement was carried out using a platinum pseudo reference electrode. The complexed ionic liquid is electrochemically stable in the potential range between -1.75 V and + 1.00 V vs. Pt which means that the electrochemical window has a value of approximately 2.75 V (figure 29). Aluminium deposition occurs in the voltage range between -0.5 V and +0.4 V vs. Al/Al<sup>3+</sup> (figure 32 and figure 33).

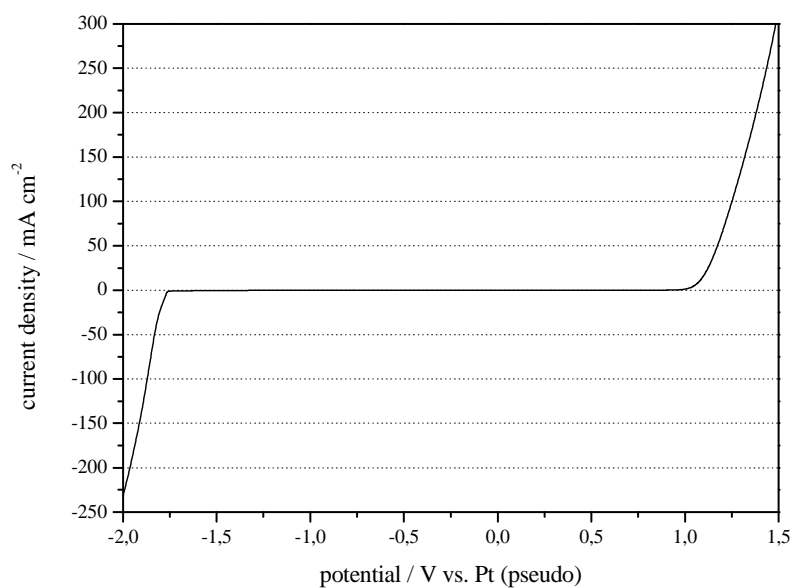


Figure 29: Electrochemical stability window of EMImCl\*1.5 AlCl<sub>3</sub> vs. Pt pseudo reference electrode

Aluminium electrodeposition was carried out at different temperatures (room temperature, 348 K and 368 K) and different current densities (20, 30 and 40 mA cm<sup>-2</sup>). The current yield was calculated according to eq. 14 and compared as function of reaction time (figure 30).



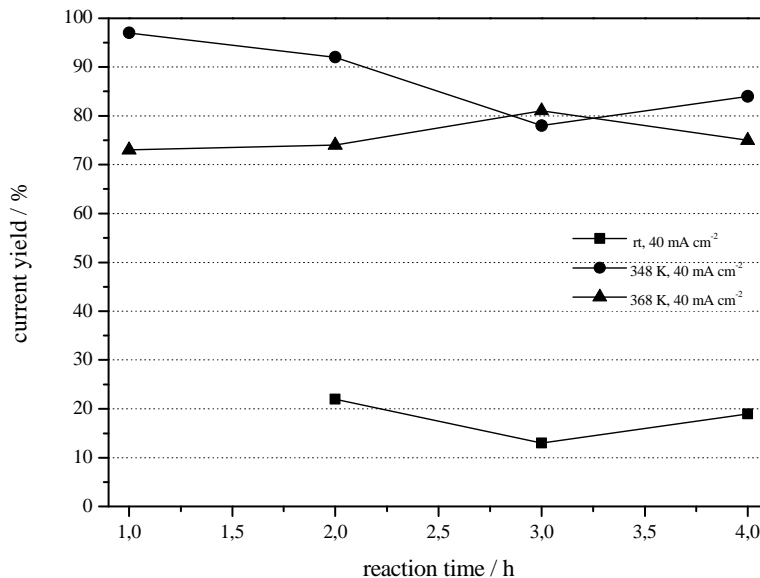


Figure 30: Current yield as function of reaction time for aluminium deposition at different reaction temperatures

The aluminium layers, deposited at room temperature and 348 K are very bad and inhomogeneous. The current yield for deposition at room temperature is very low ( $\leq 20\%$ ). Although the current yields at 348 K and 368 K are comparable, the appearance of the aluminium layer at a deposition temperature of 348 K is very bad. Therefore, further experiments were carried out with a temperature of 368 K.

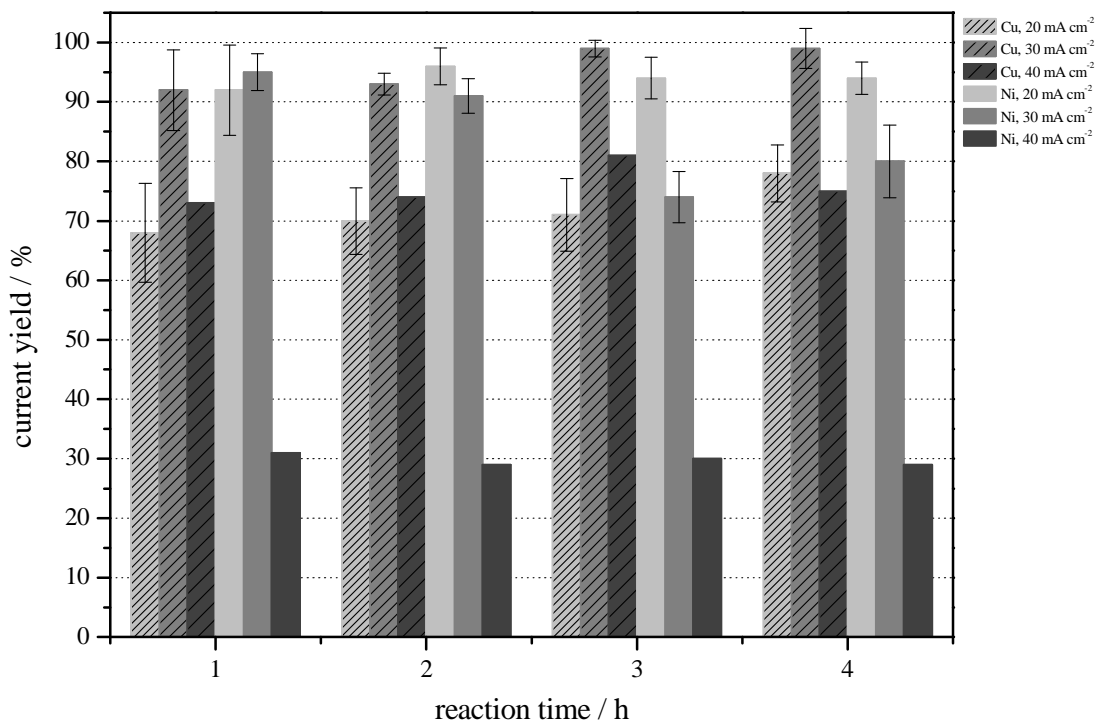


Figure 31: Current yield as function of reaction time for aluminium plating on copper and nickel plated non-woven polymer with different current densities

The results for investigation of the current yields for Al electrodeposition on copper and nickel plated non-woven polymer at 368 K are summarised in figure 31. The current yields on copper plated polymer are in general a bit higher compared to nickel plated polymer. The highest current yields could be reached on copper plated substrate with a current density of  $30 \text{ mA cm}^{-2}$ . However, the highest current yields with nickel plated polymer could be achieved with a current density of  $20 \text{ mA cm}^{-2}$ . The reason for this might be the lower conductivity of the nickel-phosphorous alloy compared to copper.

In general, the current yields for electrodeposition at a current density of  $40 \text{ mA cm}^{-2}$  are very low due to formation of aluminium dendrites. Aluminium dendrites show bad adhesion on the substrate and therefore, it is difficult to determine the exact current yield due to aluminium losses.

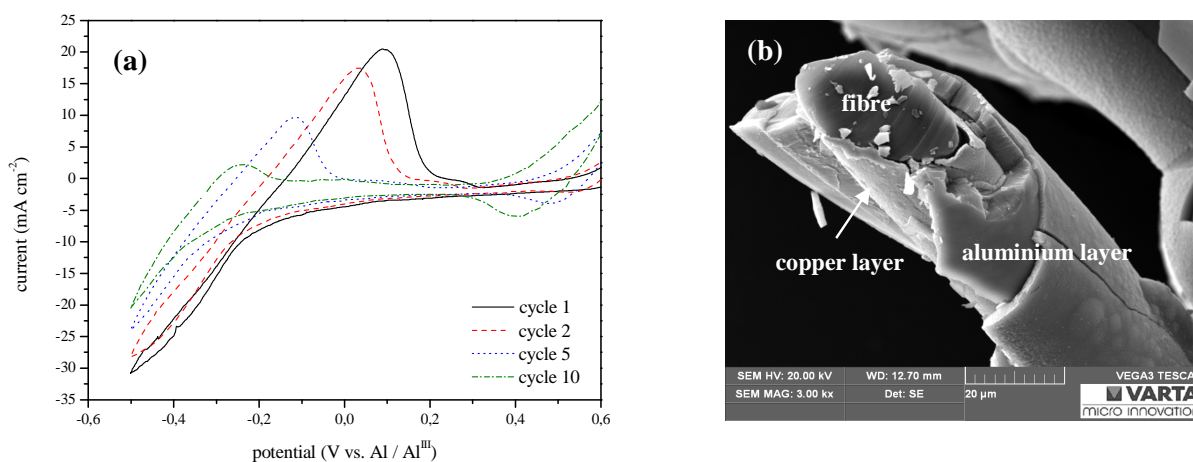


Figure 32: Cyclic voltammograms of aluminium electrodeposition on copper plated non-woven polymer from  $\text{EMImCl}^*1.5 \text{ AlCl}_3$  with a scan rate of  $10 \text{ mV s}^{-1}$  at 368 K (a) and SEM image of the cross section of a plated fibre (b)

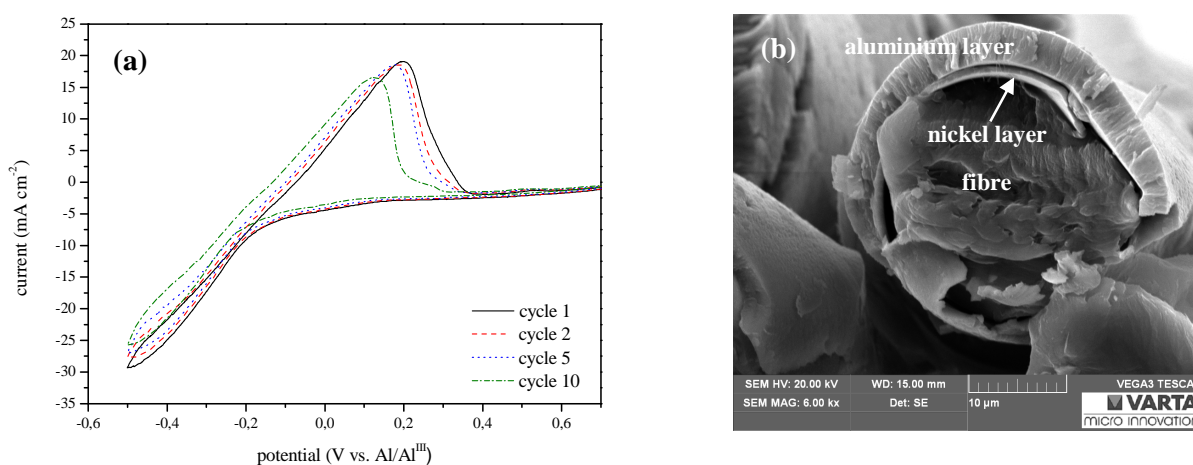


Figure 33: Cyclic voltammograms of aluminium electrodeposition on nickel plated non-woven polymer from  $\text{EMImCl}^*1.5 \text{ AlCl}_3$  with a scan rate of  $10 \text{ mV s}^{-1}$  at 368 K (a) and SEM image of the cross section of a plated fibre (b)

Typical cyclic voltammograms for deposition and stripping of aluminium from the complexed ionic liquid at 368 K are shown in figure 32 and figure 33. Figure 32 (a) shows deposition and stripping on copper plated non-woven polymer as working electrode. The cathodic and anodic peaks beginning at -0.2 V and +0.1 V vs. Al/Al<sup>3+</sup> respectively, can be attributed to the reversible deposition and dissolution of aluminium and correlates with already published data in literature [7] [79] [80] [81]. The cyclic voltammogram with the copper plated working electrode shows additional reduction and oxidation peaks at +0.4 V and +0.5 V vs. Al/Al<sup>3+</sup> respectively. They can be attributed to copper reduction and oxidation.

Interestingly, the reduction and oxidation potentials of Al<sub>2</sub>Cl<sub>7</sub><sup>-</sup> species slightly shift to more negative potentials with ongoing cycling.

Figure 33 shows the cyclic voltammogram of electrodeposition on nickel plated polymer as working electrode. Nickel seems to be more stable than copper. No additional peaks as indication for deposition and stripping of nickel can be observed within the chosen potential range. Also, the shift of Al stripping and reduction peaks toward more negative potentials is not that tremendous compared to the cyclic voltammogram, using copper plated non-woven polymer as working electrode.

Morphology, thickness and quality of the deposited metal layer can be adjusted by controlling experimental parameters. Beside reaction temperatures, applied current densities or bath additives strongly influence the appearance of deposit.

In this work it was found, that rough surfaces could be achieved with low current densities and the higher the applied current density, the smoother the surface of the deposited metal layer becomes (figure 34). The EDX spectrum after aluminium electrodeposition on nickel plated substrate (figure 35) shows a pure aluminium layer. The detected oxygen could be attributed to passivation of aluminium on air during the transfer of the sample to the vacuum chamber of the SEM. The nickel peak derives from the substrate itself.

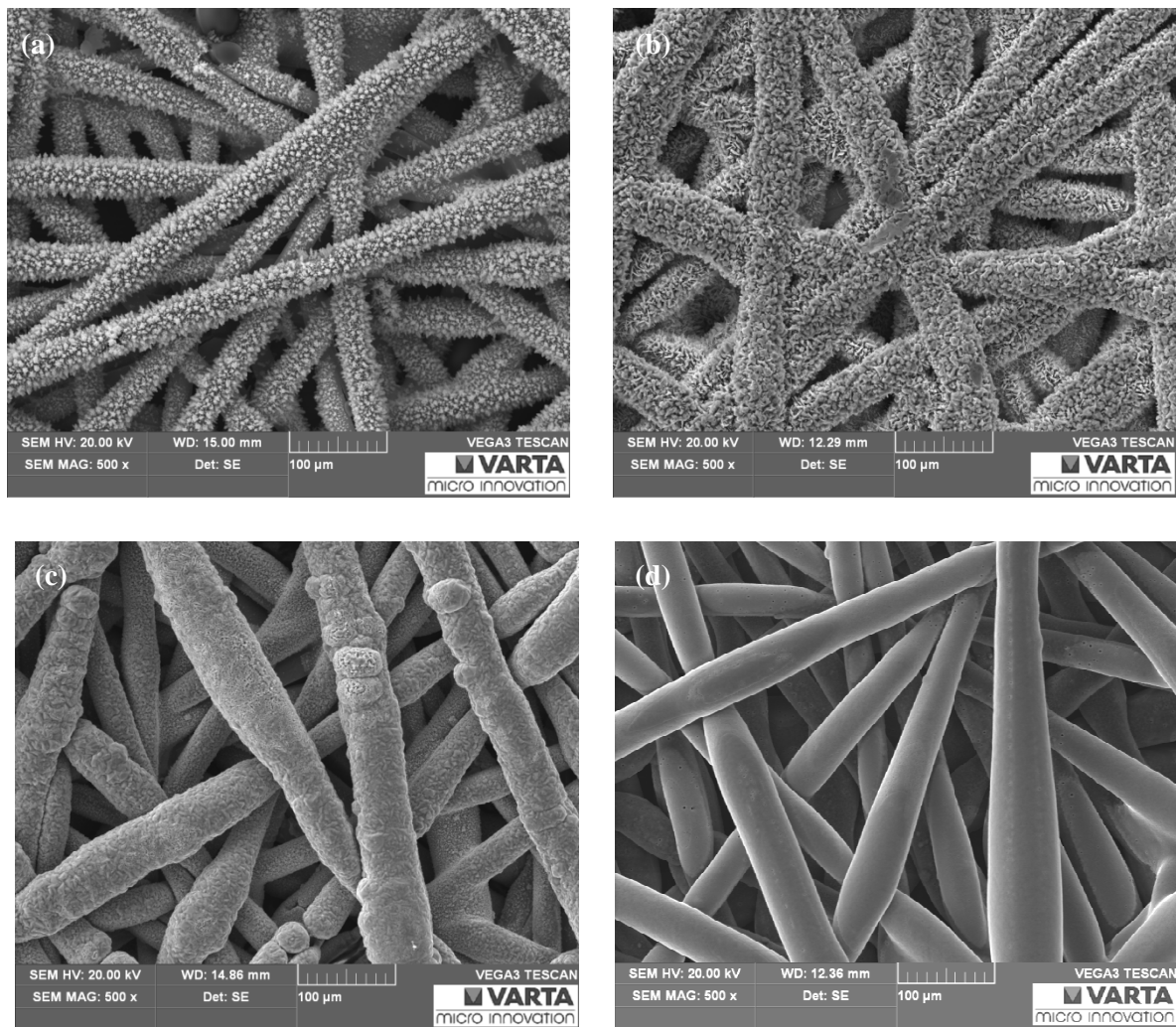


Figure 34: SEM images of deposited aluminium layers from  $\text{EMImCl} \cdot 1.5 \text{ AlCl}_3$  at 368 K with different current densities ( $10 \text{ mA cm}^{-2}$  (a),  $20 \text{ mA cm}^{-2}$  (b),  $30 \text{ mA cm}^{-2}$  (c) and  $40 \text{ mA cm}^{-2}$  (d))

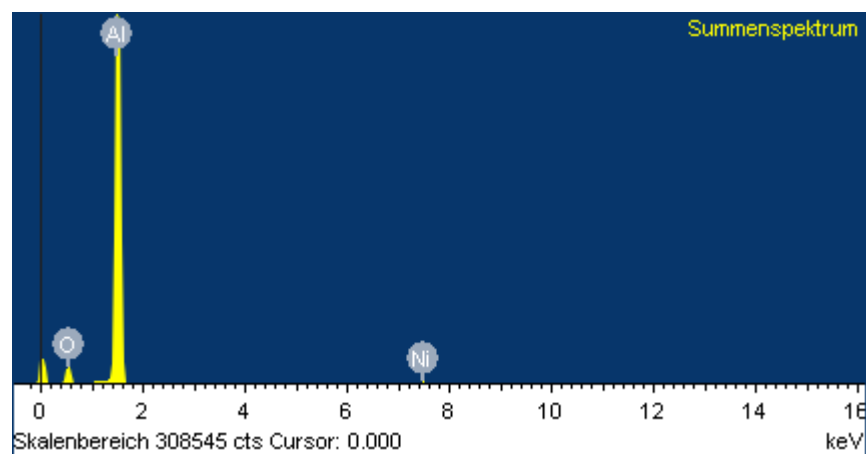


Figure 35: EDX spectrum of electrodeposited Al on Ni plated non-woven polymer from IL

### 4.2.3. Evaluation of the corrosion resistance of the new 3D current collector

For successful implementation of the new 3D current collector in lithium-ion batteries the electrochemically stability is extremely important. This means, no reduction or oxidation reactions concerning the current collector should take place within the operating potential window of the electrodes active material.

Due to its ability to form a protective surface layer (passivation), aluminium is known for its superior corrosion resistance at high voltages ( $>3.5$  V vs.  $\text{Li/Li}^+$ ). In the case of the present current collector, the metal layer beneath the aluminium layer must be shielded from electrochemical attack. If this metal layer is oxidised, a deterioration of the mechanical stability takes place.

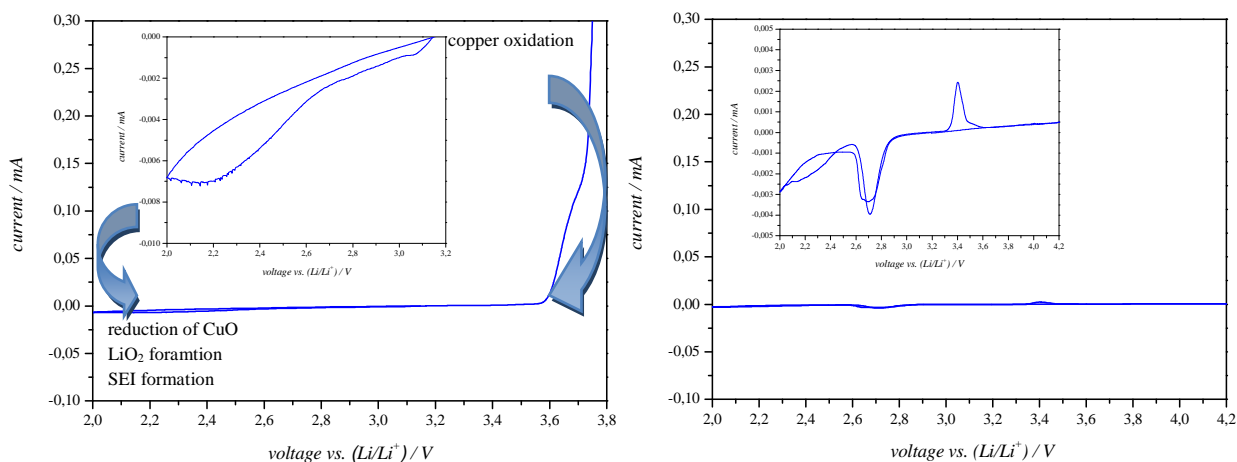


Figure 36: Cyclic voltammograms of copper metal (left) and nickel metal (right) at room temperature; scan rate:  $10 \mu\text{V s}^{-1}$

First of all, cyclic voltammograms of pure copper and nickel were recorded. Electrodes of these metals with 12 mm diameter were prepared, dried under vacuum at 393 K and assembled in 3 electrode Swagelok<sup>®</sup>-T-cell using metallic lithium as reference- and counter electrode. As electrolyte, the standard electrolyte (section 4.1.) was used. The left image in figure 36 shows a cyclic voltammogram of copper metal in a voltage range between 2.0-4.0 V vs.  $\text{Li/Li}^+$ . At 2.0-2.5 V vs.  $\text{Li/Li}^+$  a small cathodic current is observed, which could derive from  $\text{CuO}$  reduction,  $\text{LiO}_2$  building and formation of a SEI-like layer [82]. The polarisation in anodic direction results in an increase in current at 3.6 V vs.  $\text{Li/Li}^+$  and is primarily the result of copper dissolution into the electrolyte.

As suggested in literature, copper metal is stable at lower potentials vs.  $\text{Li/Li}^+$  and is therefore applied as current collector for the negative electrode [82].

Figure 36 (right image) shows a cyclic voltammogram of nickel metal in a voltage range between 2.0-4.5 V vs.  $\text{Li/Li}^+$ . Here, negligible anodic and cathodic currents with very small oxidation and reduction peaks are observed. Although it is not expected, metallic nickel is electrochemically stable in the desired potential range vs.  $\text{Li/Li}^+$ . As suggested in literature, the anodic limit of nickel is 4.5 V vs.  $\text{Li/Li}^+$  in the presence of  $\text{LiPF}_6$  [83] [84].

For further corrosion experiments, aluminium foil was coated with copper or nickel followed by electrodeposition of aluminium. The substrates were heat treated at 573 K before they were assembled in a 2 electrode glass cell using lithium metal as counter electrode and the standard electrolyte. A constant voltage of 4.3 V vs.  $\text{Li/Li}^+$  was applied for one week, before the electrodes were washed in ethylene carbonate and examined by SEM and EDX.

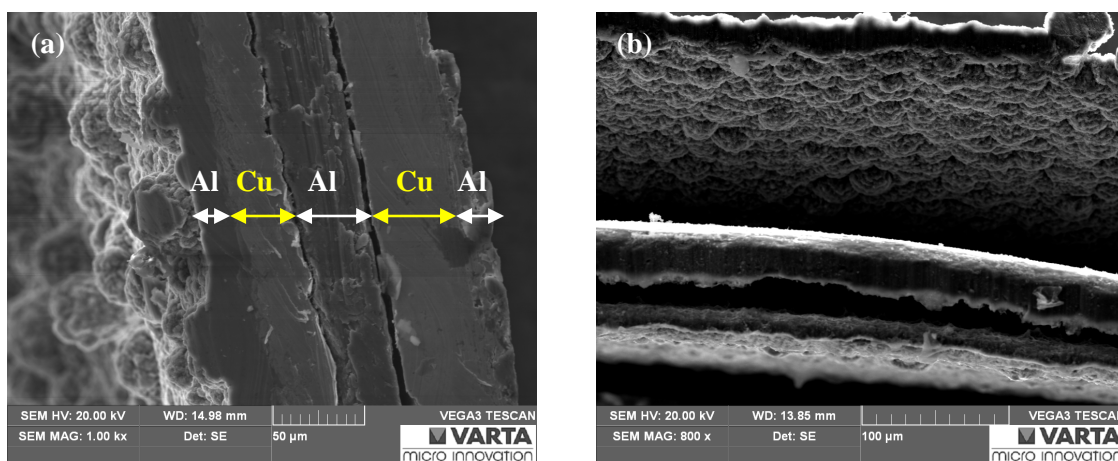


Figure 37: SEM images of copper plated working electrode before (a) and after (b) one week at constant voltage of 4.3 V vs.  $\text{Li/Li}^+$

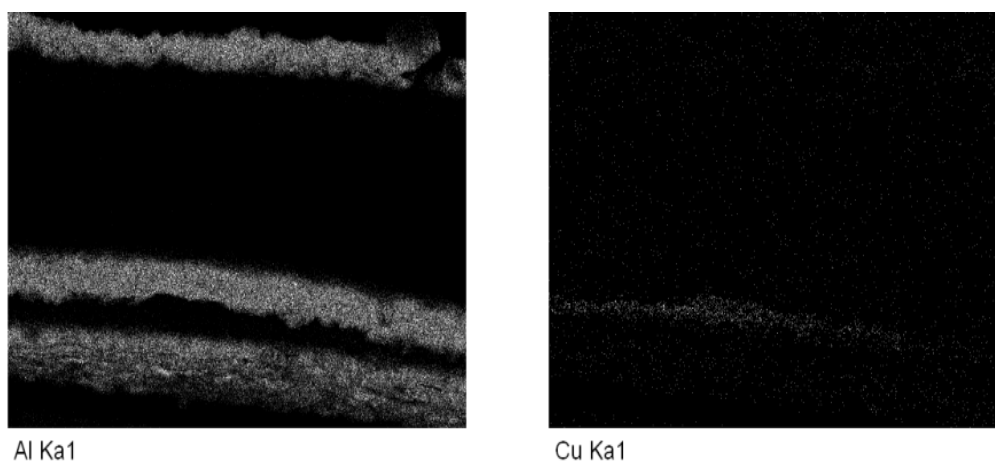


Figure 38: EDX elemental mapping of Al (a) and Cu (b) of the copper plated working electrode after one week at constant voltage of 4.3 V vs.  $\text{Li/Li}^+$

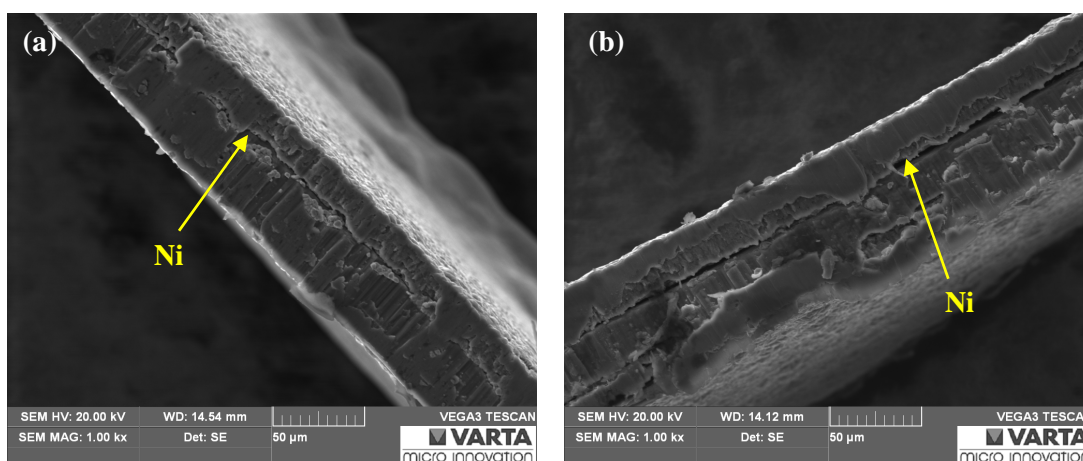


Figure 39: SEM images of nickel plated working electrode before (a) and after (b) one week at constant voltage of 4.3 V vs.  $\text{Li/Li}^+$

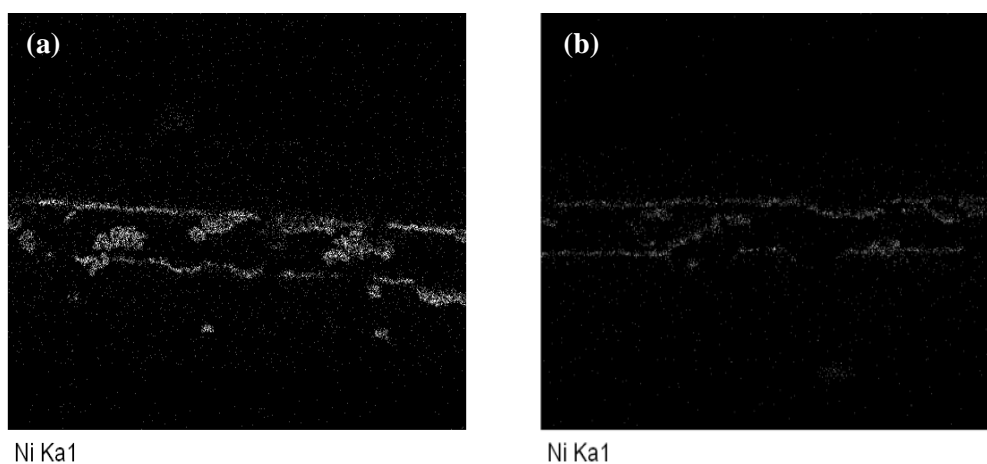


Figure 40: EDX elemental mapping of Ni before (a) and after (b) one week at constant voltage of 4.3 V vs.  $\text{Li/Li}^+$

Copper will be oxidised within the working potential range of active materials for the positive electrode and is therefore only used for negative electrodes in LIBs. Although, the copper layer is covered by a protective aluminium layer, copper is exposed to electrolyte at the cutting edges of the electrode. Figure 37b shows, that copper will be oxidised completely when the electrode is exposed to higher voltages and the current collector loses its mechanical integrity. No stable alloy is formed during heat treatment at 573 K. The elemental distribution imaging from EDX mapping shows, that nearly no copper is detectable at the working electrode after exposure to 4.3 V vs.  $\text{Li/Li}^+$  for one week (figure 38b).

In contrast, nickel seems to be much more resistant against oxidation during long time exposure at 4.3 V vs.  $\text{Li/Li}^+$ . As shown from SEM images in figure 39, there is no obvious difference between the working electrode before and after electrochemical treatment. Nickel could also be detected after the corrosion experiment with EDX spectroscopy (figure 40).

Therefore, further experiments were carried out using nickel plated non-woven polymer, covered with a layer of aluminium by electroplating.

Electrodes of nickel plated non-woven polymer were used for cyclic voltammetric experiments. They were placed as working electrode in a 3 electrode Swagelok<sup>®</sup>-T-cell using metallic lithium as reference- and counter electrode. As electrolyte, a mixture of ethylene carbonate (EC) and diethyl carbonate (DEC) (EC/DEC 3:7 v/v) with 1 M  $\text{LiPF}_6$  as conducting salt and 2 wt% vinylene carbonate (VC) as additive was used. In a voltage range from 2.5 to 4.2 V vs.  $\text{Li/Li}^+$  100 cycles were recorded with a scan rate of  $1.0 \text{ mV s}^{-1}$  (figure 41a). The same experiment was carried out using working electrodes of non-woven polymer coated with nickel under a layer of aluminium (figure 42a).

Chronoamperometric measurement was performed in a 3 electrode Swagelok<sup>®</sup>-T-cell, using metallic lithium as reference- and counter electrode and nickel plated non-woven polymer or nickel- and aluminium plated non-woven polymer as working electrode and the electrolyte as described before. A constant voltage of 4.2 V vs.  $\text{Li/Li}^+$  was applied for 240 hours and changes in current over time was recorded (figure 41b and figure 42b). The current flow of an electrochemical cell without working electrode (reference) was recorded and subtracted.



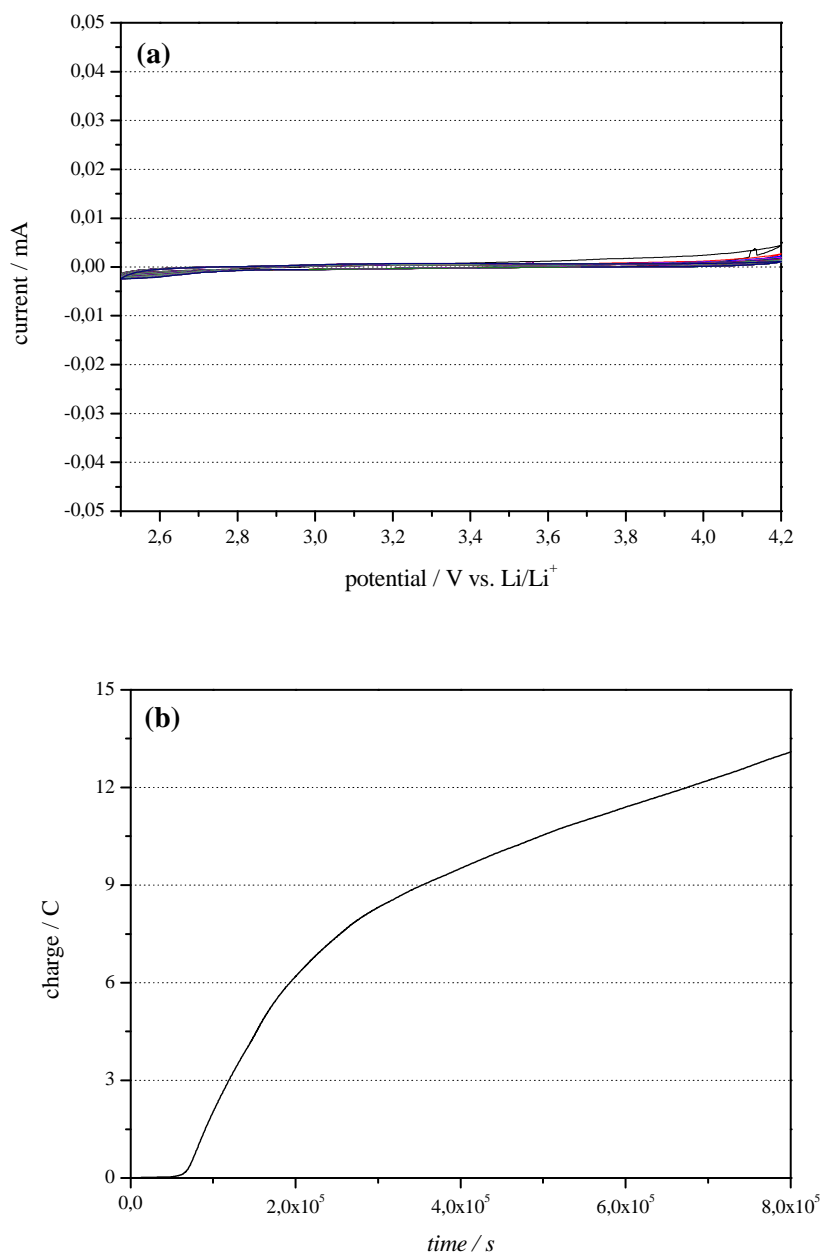


Figure 41: Cyclic voltammogram of nickel plated non-woven polymer at room temperature; scan rate: 1 mV s<sup>-1</sup> (a) and charge as function of time (b)

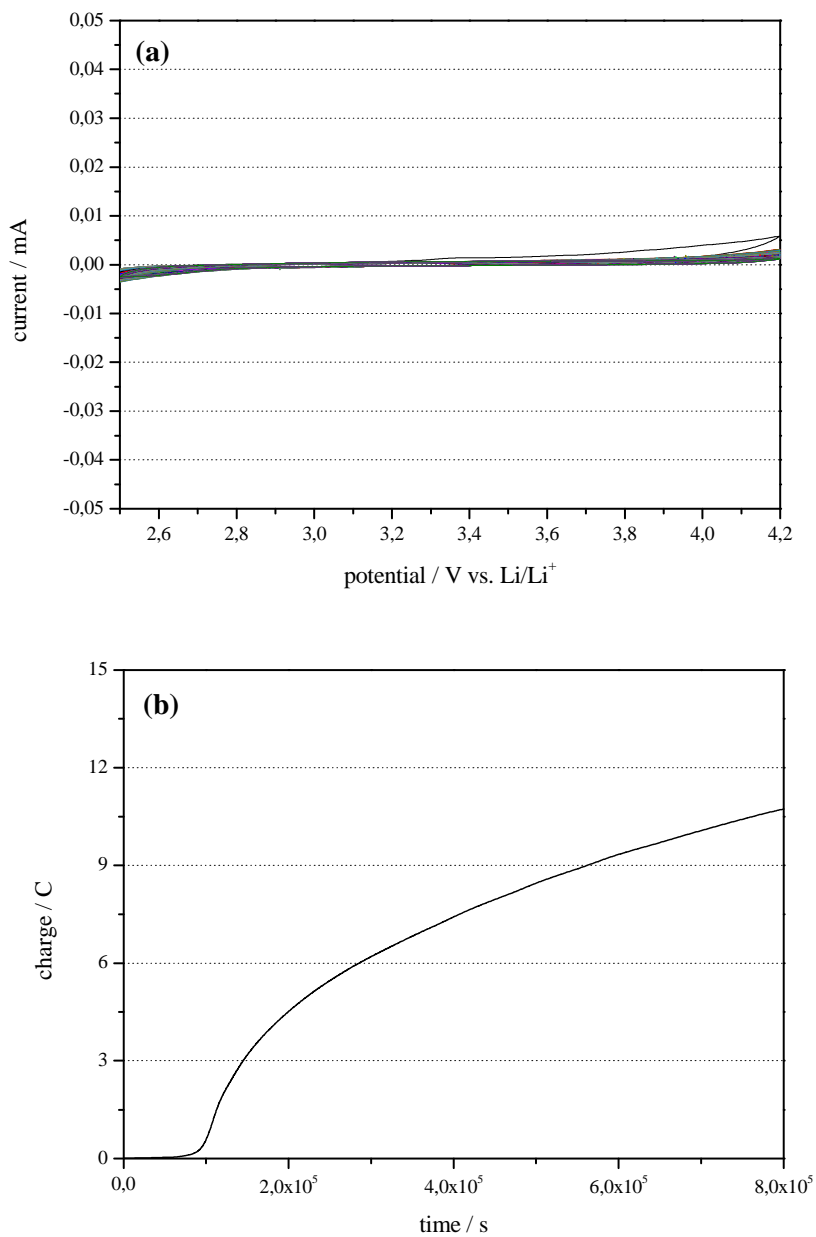
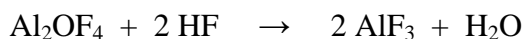
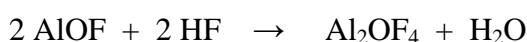
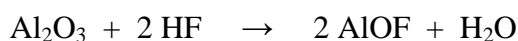


Figure 42: Cyclic voltammogram of nickel and aluminium plated non-woven polymer at room temperature; scan rate:  $1 \text{ mV s}^{-1}$  (a) and charge as function of time (b)

Table 9: Average values of the charge flow of different 3D current collectors during chronoamperometric measurement (for 240 hours)

sample	average value [C*s]	standard deviation
galv. aluminised PET	7000000	± 1100000
nickel plated PET	6800000	± 630000
PVD aluminised PET	37000	± 4000
aluminium foil	18000	± 3000

The cyclic voltammograms show, that the current flow resulting from reduction or oxidation reactions involving the current collector, is negligible within the potential range between 2.5-4.2 V vs. Li/Li<sup>+</sup> (figure 41a and figure 42a). The flow of charge during the chronoamperometric experiment at a constant voltage of 4.2 V vs. Li/Li<sup>+</sup> for 240 hours derives from different reactions like oxidation of impurities, electrolyte decomposition, the test cell itself or passivation reactions involving the current collector [82]:



The charge flow in test cells with substrates, produced by galvanic deposition of aluminium and chemical deposition of nickel, is significantly higher compared to substrate, prepared by PVD of aluminium and aluminium foil (table 9). However, this can be an indication for not completely removable impurities that derive from the plating baths. It is also possible, that oxidation of the non-woven polymer contributes to an increased flow of charge.

In conclusion it can be said, that nickel and aluminium plated non-woven polymer is electrochemically stable up to 4.2 V vs. Li/Li<sup>+</sup>. Therefore, it can be implemented as current collector for the positive electrode in LIBs.

#### 4.2.4. Determination of electrochemical and thermal decomposition products of EMImCl\*1.5 AlCl<sub>3</sub> during Al electrodeposition

Ionic liquids tend to decompose after being exposed to elevated temperatures, catalytically active molecules or the influence of an electric field [85] [86]. Beside the continuous loss of ionic liquid the resulting decomposition products can change the desired physico-chemical properties and may impact the plating process as well.

Figure 43 illustrates the thermal degradation pathways of EMImCl based on literature [85]. The most abundant decomposition products during thermal treatment of the ionic liquid are imidazole derivatives and alkylated anions as can be seen in reaction (1). Either one alkyl chain can be abstracted or even both [86]. Other considerable decomposition products are diethyl- or dimethyl imidazole, which will be formed during re-alkylation of a dealkylated cation, or by direct exchange of the alkyl chains of two cations (2) [85] [87]. A further possibility for decomposition reaction is the deprotonation of the C2-atom by strong nucleophiles, which results in the formation of carbenes (3). Carbenes are reactive components that can react with other molecules of the ionic liquid or any dissolved decomposition products present [88] [89].

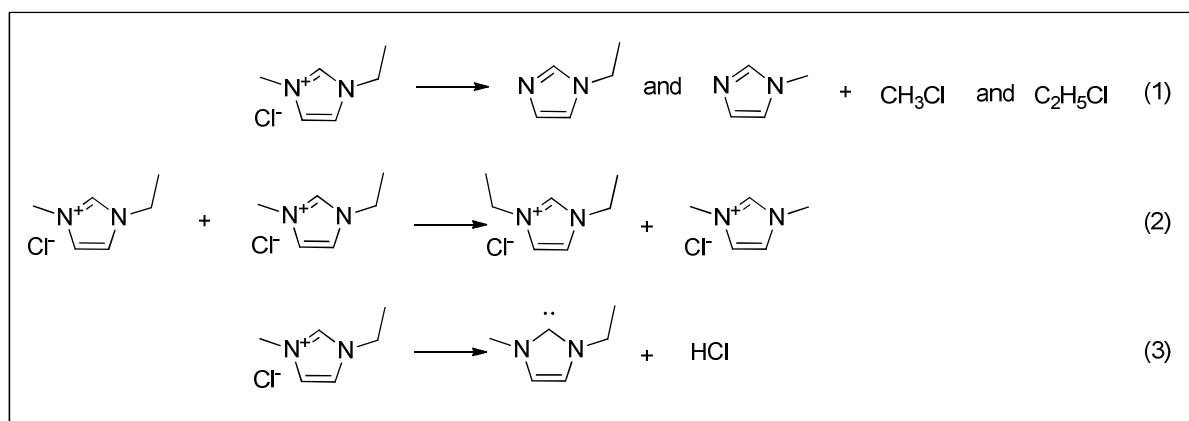


Figure 43: Possible thermal decomposition path of 1-ethyl-3-methylimidazolium chloride [85]

Possible electrochemical decomposition products of 1-ethyl-3-methylimidazolium chloride are shown in figure 44. In electrochemical processes, 1,3-dialkylimidazolium radicals are formed in analogy to carbenes. These radicals can react with each other to form neutral molecules (radical-radical coupling) [90].

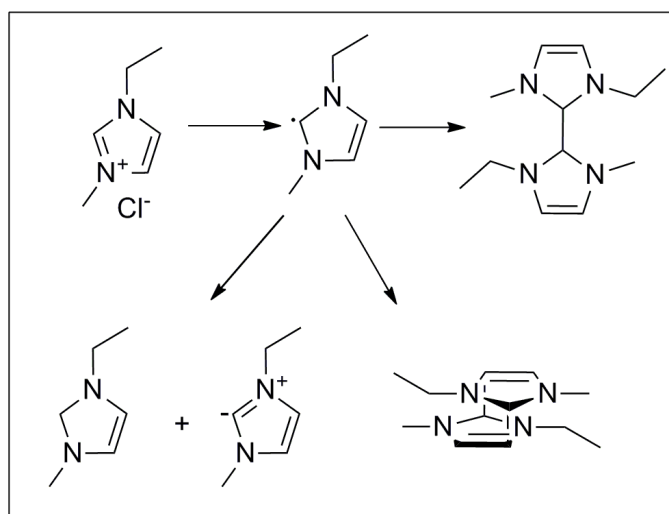


Figure 44: Possible electrochemical decomposition mechanism of EMImCl [90]

It is also very important to mention that humidity-sensitive species like  $\text{AlCl}_3$ , will undergo hydrolysis in contact with even traces of water.

Halogenaluminates show strong exothermic reactions with water and decompose to aluminium oxides and aluminium hydroxides releasing HX [91].

In this work, a methodic approach was developed to identify decomposition products of 1-ethyl-3-methylimidazolium chloride in combination with  $\text{AlCl}_3$ , using head space gas chromatography-mass spectrometry, pyrolysis gas chromatography-mass spectrometry analysis [92] and NMR studies. Samples of the complexed ionic liquid were treated thermally and electrochemically respectively.

An electrochemical cell was filled with a certain amount of electrolyte and nickel-plated polymer as working electrode as well as aluminium wires as counter- and reference electrodes were mounted. The cell was assembled and sealed under argon atmosphere. For thermal stress only, EMImCl\*1.5  $\text{AlCl}_3$  was heated to 368 K and the temperature was held for 100 hours. For electrochemical treatment, the aluminium deposition was carried out at constant voltage mode with -0.1 V vs.  $\text{Al}/\text{Al}^{3+}$  at 368 K up to 100 hours. These samples were prepared for NMR analysis in an argon-filled glove box.

#### 4.2.4.1. NMR analysis

For NMR studies, the samples were prepared in an argon-filled glove box without any solvent ( $D_2O$  capillaries) except for the measurement of thermally treated pure EMImCl, which was dissolved in  $CDCl_3$ .  $^1H$  and  $^{13}C$  NMR spectra of the fresh, untreated EMImCl\*1.5  $AlCl_3$  were also recorded (table 10).

Table 10:  $^1H$  NMR data (300 MHz,  $D_2O$ ) for EMImCl\*1.5  $AlCl_3$  and EMImCl (300 MHz,  $CDCl_3$ ) before and after electrochemical and/or thermal treatment [93] [94]

		t, 3H	s	s	s, 3H	q, 2H	s, 1H	s, 1H	s, 1H
1*	$\delta$ (ppm)	1.03	-	-	3.42	3.73	6.83	6.87	7.85
2*	$\delta$ (ppm)	0.91	2.12	-	3.30	3.62	6.71	6.76	7.73
3*	$\delta$ (ppm)	1.08	-	3.00	3.46	3.78	6.88	6.92	7.89
4*	$\delta$ (ppm)	1.01	2.30	2.91	3.39	3.71	6.81	6.85	7.82
5*	$\delta$ (ppm)	1.01	2.29	2.58	3.40	3.71	6.81	6.86	7.83
6*	$\delta$ (ppm)	1.30	-	-	3.82	4.13	7.44	7.44	10.16

\*1 = EMImCl\*1,5  $AlCl_3$  before treatment

\*2 = EMImCl\*1,5  $AlCl_3$  after thermal treatment at 368 K

\*3 = EMImCl\*1,5  $AlCl_3$  after electrochemical and thermal treatment at 368 K for 10 h

\*4 = EMImCl\*1,5  $AlCl_3$  after electrochemical and thermal treatment at 368 K for 50 h

\*5 = EMImCl\*1,5  $AlCl_3$  after electrochemical and thermal treatment at 368 K for 100 h

\*6 = EMImCl after thermal treatment at 368 K for 100 h

**EMImCl\*1.5  $AlCl_3$  (before treatment):**  $^{13}C$  NMR, ( $D_2O$ ):  $\delta$  14.81 (s,  $CH_3$ ), 36.53 (s,  $CH_3$ ), 45.11 (s,  $CH_2$ ), 121.84 (s, 1C), 123.53 (s, 1C), 134.11 (s, 1C) ppm.

#### 4.2.4.2. Pyrolysis-GC/MS and headspace GC/MS analysis

For determination of volatile decomposition products of the electrolyte, static headspace GC/MS analysis was carried out. Therefore, the EMImCl\*1.5  $AlCl_3$  was thermally aged at 368 K for 100 h in a glass vial fitted with a septum. Samples (4.0 mL) of the gaseous phase above the solution were taken using a 10 mL gas-tight syringe (Hamilton) and injected into the gas chromatograph system.

Chloromethane, dichloromethane and hydrochloric acid could be identified as volatile decomposition products after thermal treatment of EMImCl\*1.5  $AlCl_3$  at 368 K (figure 45).

The silicon containing compound with a retention time of 2.10 min. derives from the reaction

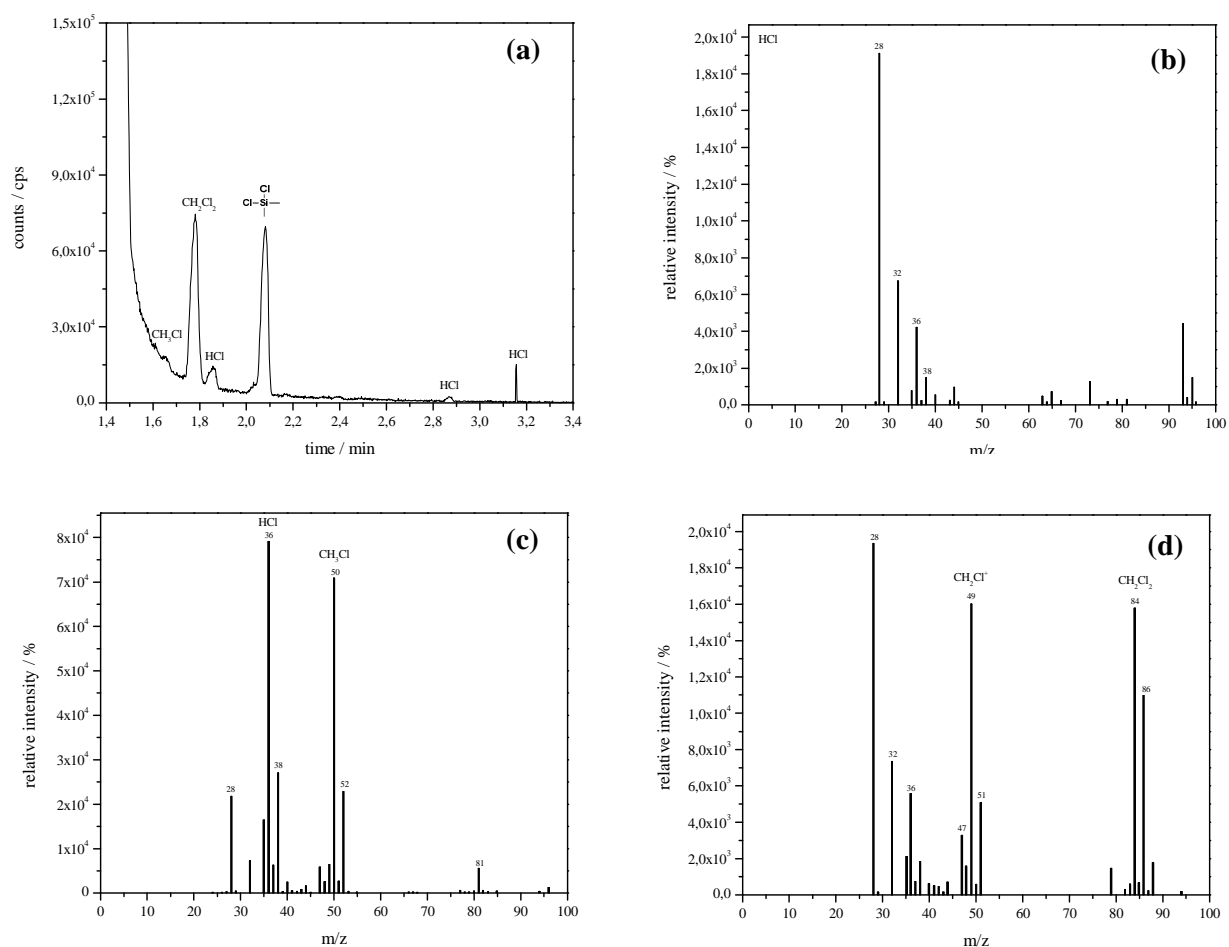


**Figure 45:** Chromatogram of volatile decomposition products of EMImCl\*1.5 AlCl<sub>3</sub> (a) and accompanied mass spectra of hydrochloric acid (b), chloromethane (c) and dichloromethane (d)

For Py-GC/MS analysis fresh EMImCl\*1.5 AlCl<sub>3</sub> was dropped into a small sized vertical furnace. The temperature was set to 368 K for one hour after which time the evolved gas was analysed. The results of Py-GC/MS indicate that chloromethane (figure 46a), hydrochloric acid (figure 46b), methylimidazole (figure 46c), ethylimidazole (figure 46d) and deprotonated ethyl-methylimidazole (figure 46e) are the main thermal decomposition products of the complexed ionic liquid. No products reflecting decomposition of the imidazole rings at this temperature could be found in the thermogram. Extracted ion thermograms are shown in figure 46. The mass spectra of the certain degradation products of the ionic liquid show typical fragmentation pattern of imidazole [95] [96] and could therefore be identified.

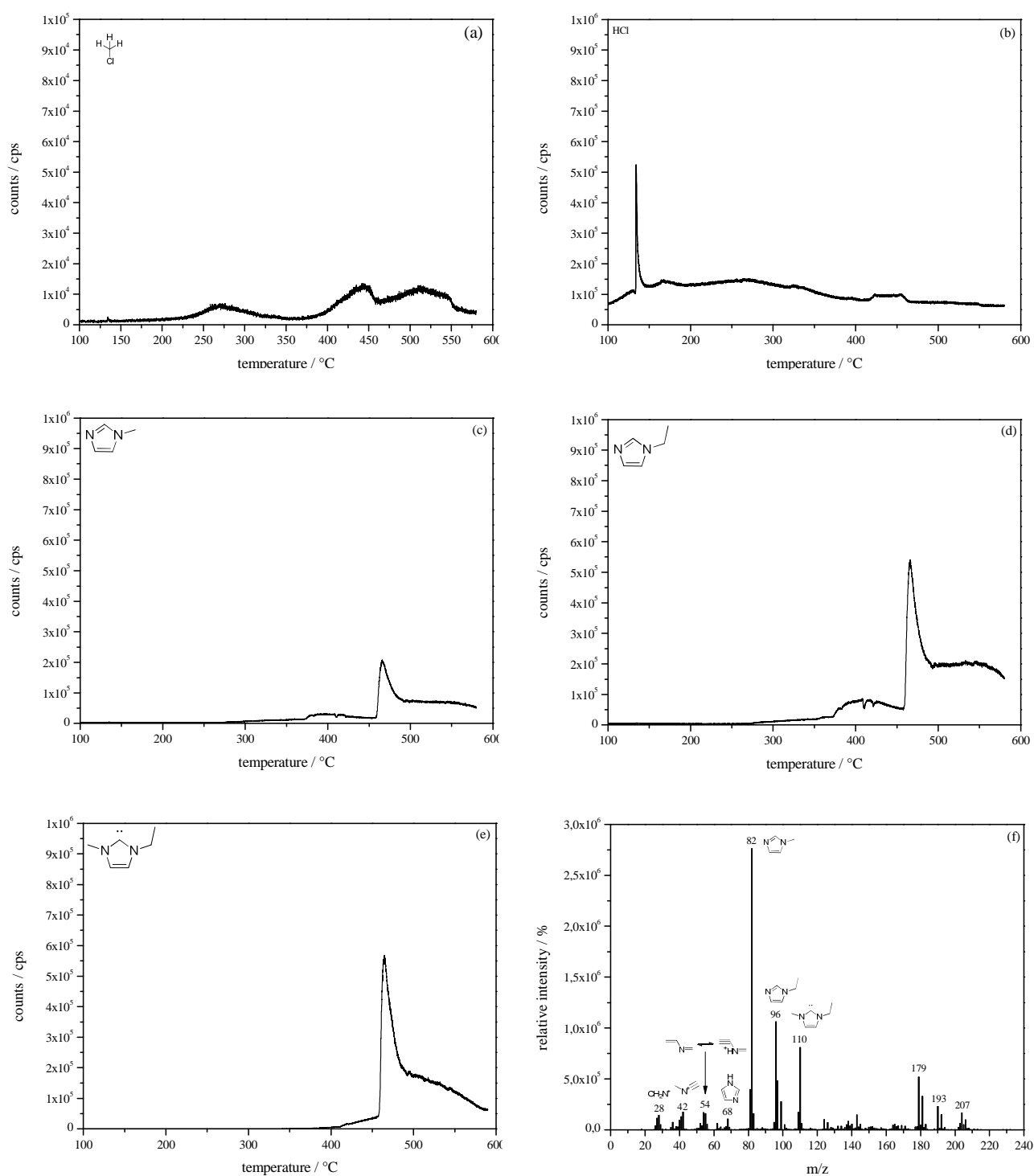


Figure 46: Extracted ion thermograms of chloromethane (a), hydrochloric acid (b), methylimidazole (c), ethylimidazole (d) and ethyl-methylimidazole (e) and the accompanied mass spectra (f)

The mass spectrum allocated to figure 46f includes peaks with high masses ( $m/z$  193 and  $m/z$  207) and could be assigned to injection liner bleeding due to massive HCl development during sample degradation. The origin of the peak with  $m/z$  179 couldn't be clarified until now.



It is also possible, that the peaks with the masses  $m/z$  179,  $m/z$  193 and  $m/z$  207 derive from dimerisation of reactive imidazolium intermediates (figure 44).

Although EMIm halides ( $\text{Cl}^-$ ,  $\text{Br}^-$  or  $\text{I}^-$ ) exhibit temperatures for onset decomposition between 553 K – 583 K [97], we have found additional peaks in the  $^1\text{H}$ -spectra of the thermally treated sample at 368 K. A possible explanation could be the thermal decomposition of the complexed ionic liquid indicating the presence of alkyl chlorides and HCl in the thermal stressed sample. On the other hand the  $^{13}\text{C}$ -NMR spectra don't show additional peaks, but this could be due to a less sensitiveness of the  $^{13}\text{C}$ -NMR compared to  $^1\text{H}$ -NMR or GC/MS analysis. According to literature, heating of EMImCl at 373 K does not increase the imidazole content in the sample which can be an indication for decomposition of alkylated imidazoles [87]. In our observations there are no additional peaks in the  $^1\text{H}$ -spectra of heat treated EMImCl without  $\text{AlCl}_3$  (table 10). It seems that  $\text{AlCl}_3$  initiates the decomposition of the IL and decreases this onset temperature dramatically.

On the other hand, in the electrochemically treated sample at room temperature, no additional peaks could be observed in the NMR spectra of the electrolyte. However, the electrochemically stressed samples at elevated temperatures (368 K) show these additional peaks too and are in agreement with this theory. In further consequence,  $\text{AlCl}_3$  can be deemed as the crucial factor for degradation of 1-ethyl-3-methyl-imidazolium chloride used for aluminium electrodeposition at elevated temperatures which would be optimised conditions in terms of electroplating [98].

#### 4.2.5. Comparison of mass, conductivity and contact surface area of different current collectors

The mass, conductivity and BET surface area of various 3D current collectors and Al foil are compared in table 11. The conductivity of the samples was determined according to the 4-point probe [99]. The conductivity of the metallised non-woven polymer is about 7-8 times lower compared to aluminium foil. It is believed that the reduced conductivity of the metal plated 3D current collector could derive from  $\text{Al}_2\text{O}_3$  formation on the aluminium surface in contact with air. Pure aluminium naturally forms a thin surface layer in contact with oxygen with a thickness of about  $0.1 \mu\text{m}$ - $0.5 \mu\text{m}$  [100]. The higher the surface area, the more  $\text{Al}_2\text{O}_3$  will be created on the surface of the working piece. Since aluminium oxide is an insulating material the conductivity will be reduced. Additionally, the template of the 3D current collector is an insulating material, and therefore, it will reduce the overall conductivity too. Also the complex geometry of the 3D current collector will affect the accuracy of calculation. As inferred from the BET surface area the used non-woven polymer increases the contact surface by five times compared to conventional aluminium foils. The unusual unit [ $\text{m}^2 \text{m}^{-2}$ ] derives from the calculation of the surface area of the current collector from the value of the BET surface [ $\text{m}^2 \text{g}^{-1}$ ].

The mass of Al foil is relatively high, which increases the mass of inactive components in LIBs and therefore reduces the energy density of the battery. The mass of first generation 3D current collector is slightly lower compared to Al foil. As can be seen from standard deviation, this non-woven polymer is very inhomogeneous (table 11). The homogeneity could be improved with the second generation non-woven polymer and also the mass of this current collector could be significantly reduced.

Table 11: Comparison of mass and conductivity of various current collectors

	Al foil	non-woven 0.3 $\mu\text{m}$ Al	non-woven 1 $\mu\text{m}$ Al	non-woven 2 $\mu\text{m}$ Al
mass [ $\text{mg cm}^{-2}$ ]	$7.54 \pm 0.03$	$6.97 \pm 0.53$	$3.31 \pm 0.09$	$3.93 \pm 0.22$
conductivity [ $\text{S cm}^{-1}$ ]	$380000 \pm 21000$	$25000 \pm 40$	$49000 \pm 3000$	$68000 \pm 7000$
thickness [ $\mu\text{m}$ ]	$33.07 \pm 0.93$	$149 \pm 7.46$	$97.38 \pm 2.29$	$100.25 \pm 1.20$
BET surface area [ $\text{m}^2 \text{m}^{-2}$ ]*	2.0	-	10.3	-

\* received from determination of the BET surface area [ $\text{m}^2 \text{g}^{-1}$ ]; the surface area of the current collector [ $\text{m}^{-2}$ ] was calculated from the BET surface [ $\text{m}^2 \text{g}^{-1}$ ]

## 4.2.6. Electrode preparation and electrochemical characterisation

### 4.2.6.1. Electrodes with 1. generation current collector

For implementation of the new 3D current collector in LIBs, 20 mm x 20 mm pieces of non-woven polymer were coated with nickel by chemical reduction according to the procedure described in section 4.2.2. (table 8). Afterwards, the nickel plated pieces were electroplated with aluminium from  $\text{EMImCl} \cdot 1.5 \text{ AlCl}_3$  [75] with a current density of  $10 \text{ mA cm}^{-2}$  at 368 K for 60 min. Due to apparatus limitations just small pieces of non-woven polymer could be plated with aluminium. The thicknesses of the deposited metal layers were determined using scanning electron microscopy (SEM). The deposited nickel film is almost uniform and has a thickness of about 700 nm. Due to variation of current density at the edges and planes (bone effect), the thickness of Al varies in the range between  $10 \mu\text{m}$  and  $20 \mu\text{m}$ . But electrodes ( $\varnothing 12 \text{ mm}$ ) were punched out just in the middle of the current collector and the variation in mass of Al is therefore not that tremendous. Afterwards, an electrode slurry was prepared (table 12) and the current collector was coated with by doctor blade method. As figure 47a indicates, a rough aluminium deposit could be achieved using a current density of  $10 \text{ mA cm}^{-2}$ .

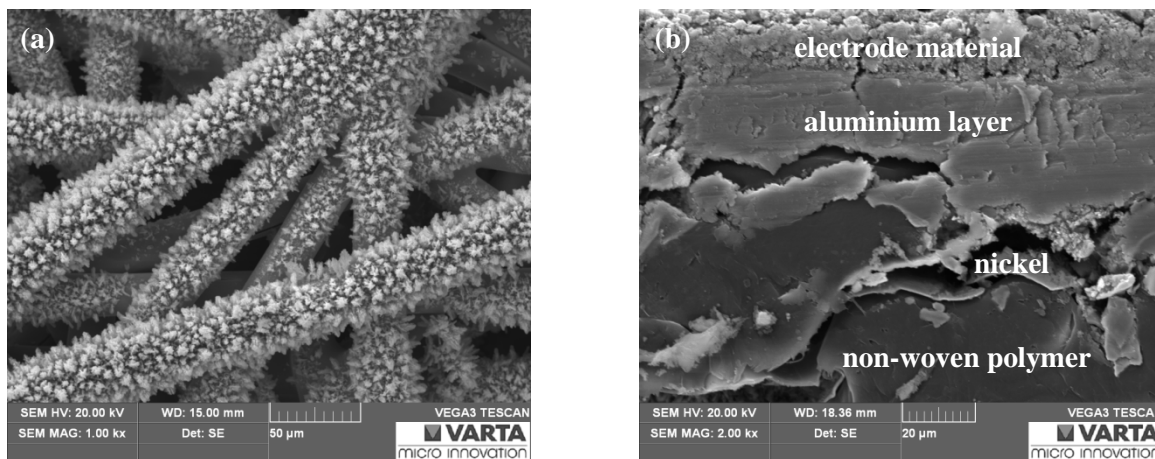


Figure 47: Surface of current collector (a) and cross section of a  $\text{LiFePO}_4$ -electrode (b)

Table 12: Electrode slurry composition

	components	composition [%]
<b>active material</b>	lithium iron phosphate ( $\text{LiFePO}_4$ )	87
<b>binder</b>	polyvinylidene fluoride (PVDF)	8
<b>conducting additive</b>	carbon black (Super P)	5
<b>solvent</b>	n-methyl-2-pyrrolidon	

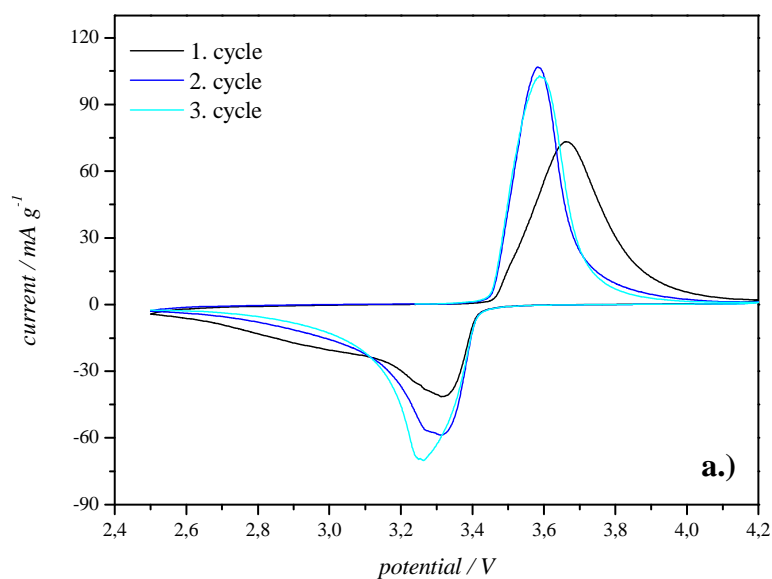


Table 13: Corresponding lithiation and delithiation capacities of CV measurement (fig. 48 above)

sp56_k18_LFP_6		mass active material/ mg	6.73
cycle	delith. capacity/mAh g <sup>-1</sup>	lith. capacity/mAh g <sup>-1</sup>	rev./%
1	169.9	177.4	95.8
2	172.8	170.1	101.6
3	171.3	171.5	99.9

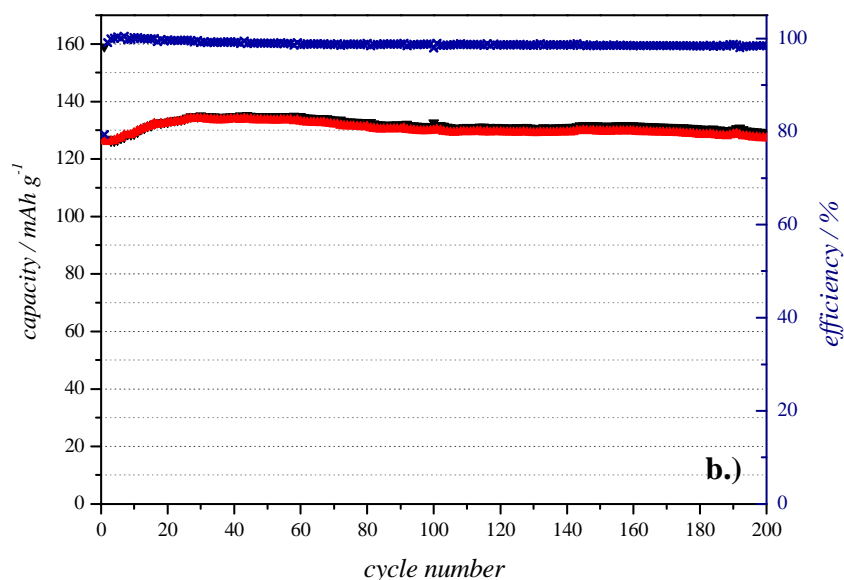


Figure 48: Cyclic voltammogram ((a), scan rate: 30  $\mu\text{V s}^{-1}$ ) and constant current cycling ((b), rate: 1 C) of LFP with 3D current collector

The same electrode was used for both measurements. After the CV experiment, the same test cell was subsequently used for constant current cycling. It was not possible to determine the mass of the current collector due to inhomogeneity of the non-woven polymer. Therefore, the mass of active material of the electrode is calculated from the second lithiation capacity, obtained from CV measurement, according to the following equation:

$$m = \frac{(c_{lith} * 1000)}{spec. cap_{LiFePO_4}} \quad (\text{Eq. 15})$$

m.....mass of active material [g]

$c_{lith}$ .....lithiation capacity [mAh]

spec. cap.  $LiFePO_4$ .....specific capacity of  $LiFePO_4$ ;  $\sim 170 \text{ mAh g}^{-1}$

For this kind of capacity determination it should be noted, that a slow scan rate has to be chosen or that the kinetics of the material is sufficient fast. Otherwise the obtained capacity is not accurate. The cyclic voltammogram (figure 48a) shows significant oxidation and reduction peaks of LFP. Delithiation and lithiation of this material occurs at 3.6 V and 3.3 V vs.  $Li/Li^+$ , respectively. According to this equation, the electrode was loaded with 5.92 mg of active material (total mass load: 6.81 mg or  $6.02 \text{ mg cm}^{-2}$ ). With electrodes prepared in this manner, the theoretical capacity of  $LiFePO_4$  of  $170 \text{ mAh g}^{-1}$  could be reached only in the first few cycles of CV measurement. During constant current cycling the electrode could reach a relative stable capacity of about  $130 \text{ mAh g}^{-1}$  over 200 cycles.

One possible reason for the reduced utilisation of the capacity of  $LiFePO_4$  could be that the chosen c-rate was too high. This active material has a relatively slow lithium ion diffusion rate at room temperature that makes it not possible to utilise the whole active material at higher rates [101]. Because of the lavish production of these electrodes, no further experiments with lower rates were carried out.

Another reason for not fully exploited capacity could origin from reduced conductivity of the current collector due to  $Al_2O_3$  formation during electrodeposition.

#### 4.2.6.2. Electrodes with 1. generation current collector (PVD of Al (300 nm))

The non-woven polymer was plated with aluminium by physical vapour deposition (PVD). The diameter of the fibres is about 20  $\mu\text{m}$  and the thickness of the non-woven polymer comes to 150  $\mu\text{m}$ . Figure 49 shows a SEM image (left) and an EDX spectrum (right) of Al plated polymer. The detected carbon derives from the polymer and the carbon tape. The oxygen could be assigned to the polymer as well as from passivation of aluminium on air. The layer thickness of the deposit is 300 nm. The current collector was coated with a slurry (composition according to table 14) by doctor blade method.

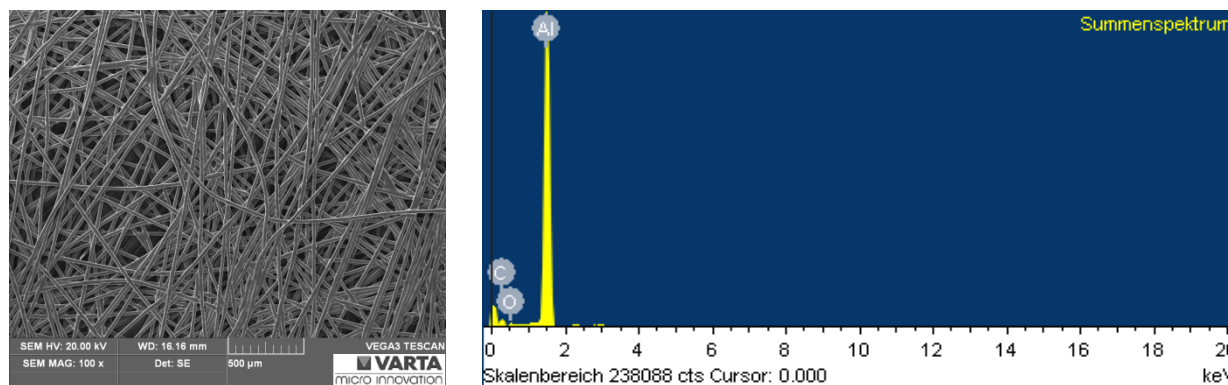


Figure 49: SEM image (left) and EDX spectrum (right) of with Al PVD plated non-woven polymer

Table 14: Electrode slurry composition

	components	composition [%]
<b>active material</b>	lithium cobalt oxide ( $\text{LiCoO}_2$ )	88
<b>binder</b>	polyvinylidene fluoride (PVDF)	7
<b>conducting additive</b>	carbon black (Super P)	5
<b>solvent</b>	n-methyl-2-pyrrolidon	

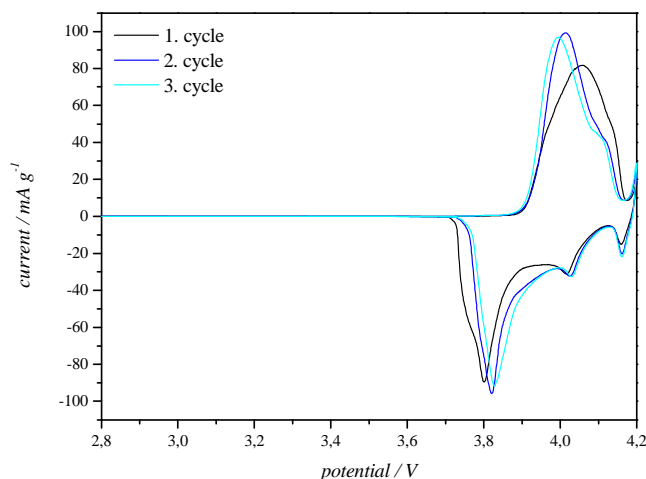


Figure 50: Cyclic voltammogram (scan rate:  $30 \mu\text{V s}^{-1}$ ) of LCO with 3D current collector

Table 15: Corresponding lithiation and delithiation capacities of CV measurement (fig. 50)

sp32_k14_LCO_1		mass active material/ mg	8.60
cycle	delith. capacity/mAh g <sup>-1</sup>	lith. capacity/mAh g <sup>-1</sup>	rev./%
1	133.2	135.5	98.2
2	134.3	135.9	98.8
3	134.3	135.8	98.9

The composition of the electrodes with the 3D current collector is comparable to that of the 2D current collector.

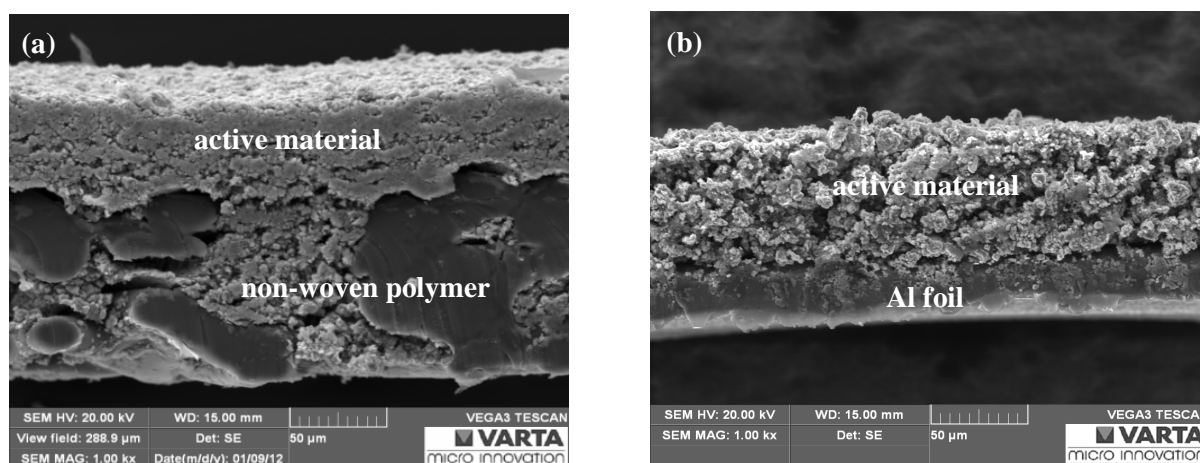


Figure 51: SEM images of the cross section of LCO electrodes with 3D current collector (a) compared to 2D current collector (b)

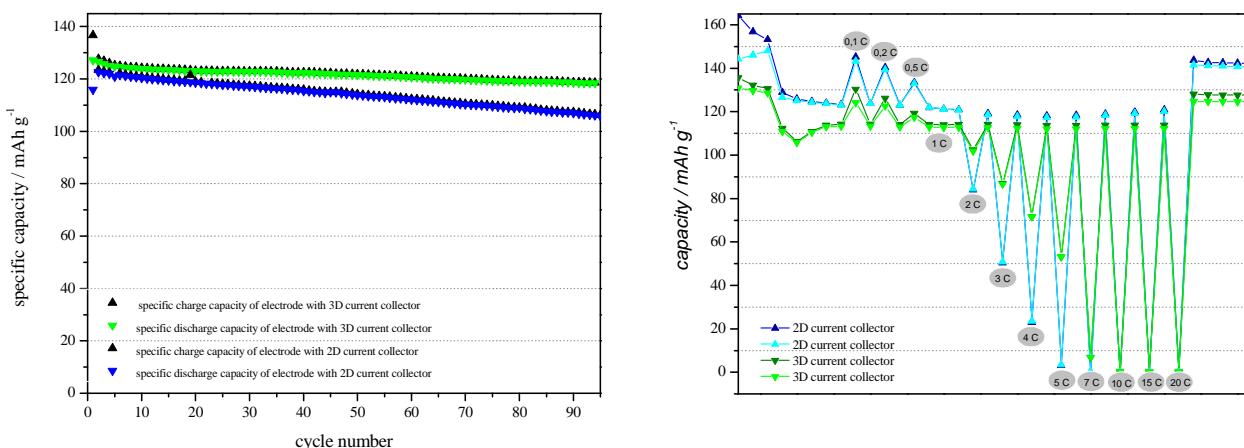


Figure 52: Comparison of constant current cycling (left, 1C) and rate capability test (right) of an electrode with 3D current collector (8.60 mg) and 2D current collector (8.50 mg)

In the SEM images of figure 51 the cross section of a LiCoO<sub>2</sub>-electrode with aluminium plated non-woven polymer and aluminium foil as current collector are compared. As shown in figure 51a, the electrode material penetrates into the pores of the 3D current collector. The higher surface area leads to higher contact area of active material and current collector. The 3D current collector could be loaded with much higher masses of active material. This leads to an improvement in capacity with a better rate capability compared to electrodes with a 2D current collector. However, the increased contact area between active material and current collector leads to an improved mechanical stability of these electrodes in contrary to electrodes with a flat 2D current collector.

Although the thickness of the 3D current collector is much larger than that of a typical aluminium foil (~150 µm compared to ~30 µm), the areal weight of the 3D aluminium plated non-woven polymer is about 20% less than that of aluminium foil (table 11). As mentioned before, the active material penetrates into the voids of the 3D current collector while it is connected on the surface of the 2D current collector. Therefore, the difference in thickness of the final electrodes is much less tremendous. This, and the possibility of higher mass loading, will contribute to a higher specific energy of the final device.

Due to the high flexibility of the conductive non-woven polymer with the embedded active material, it can be easily cut into various shapes. For comparison reasons, thick LiCoO<sub>2</sub> electrodes with aluminium foil as current collector were fabricated and treated as the electrodes with the 3D current collector. The film of the thick 2D electrodes often delaminates from the current collector and had bad final film morphologies.

Because of the inhomogeneous current collector, determination of the exact mass of the electrode and the c-rate is difficult. To evaluate the c-rate, the 2nd lithiation capacity of electrodes from the cyclic voltammetry experiment was used for the cycling study (figure 52). With both current collectors the theoretical capacity for half lithiation of LiCoO<sub>2</sub> (136 mAh g<sup>-1</sup>) could be reached in the first cycles. As seen in figure 52 (left), the electrode with the 3D current collector could reach a remaining capacity of 118 mAh g<sup>-1</sup> after 100 cycles (1C rate) with a capacity loss of 13% and reversibilities near 100%. For the electrode with aluminium foil as current collector, a capacity of just 106 mAh g<sup>-1</sup> is left with a capacity loss of 22% after 100 cycles (1C rate).



A rate capability test of a 3D electrode compared to an electrode with a metal foil as current collector is shown in figure 52 (right). The performance of the electrode with the metallised non-woven polymer as current collector is much better compared to the conventional under lab conditions produced electrode. When this electrode is charged with a rate of 5 C, the capacity drops to zero. The remaining capacity of the electrode with the 3D current collector is still above 60 mAh g<sup>-1</sup>.

The poorer reversibilities, performance and the tremendous capacity fade of the electrode with the 2D current collector could be accounted to the poorer mechanical stability and higher resistivity compared to the electrode with a 3D current collector.

#### 4.2.6.3. Electrodes with 2. generation current collector

The more homogenous non-woven polymer was plated with aluminium by physical vapour deposition (PVD) with different layer thicknesses (1  $\mu\text{m}$  resp. 2  $\mu\text{m}$ ; comparison of mass: table 10). The diameter of the fibres is less than 10  $\mu\text{m}$  and the thickness of the non-woven polymer came to around 100  $\mu\text{m}$ . Figure 53 shows a SEM image and figure 54 an EDX spectrum of Al plated non-woven polymer. The detected carbon derives from the polymer and the oxygen could be assigned to the polymer as well as to passivation of aluminium on air. An electrode slurry was prepared, as described before (table 14) and the current collector was coated by doctor blade method.

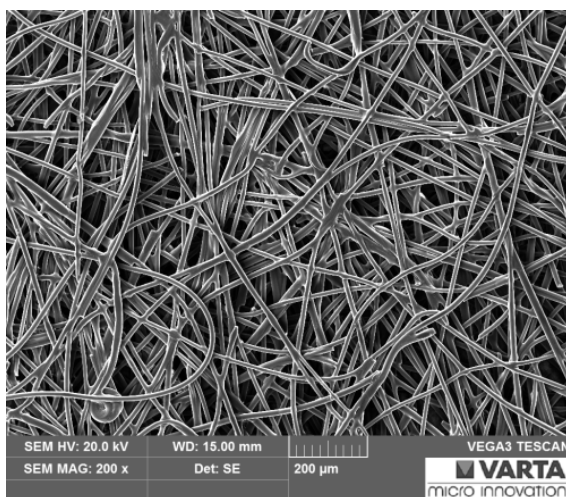


Figure 53: SEM image of with Al PVD plated non-woven polymer

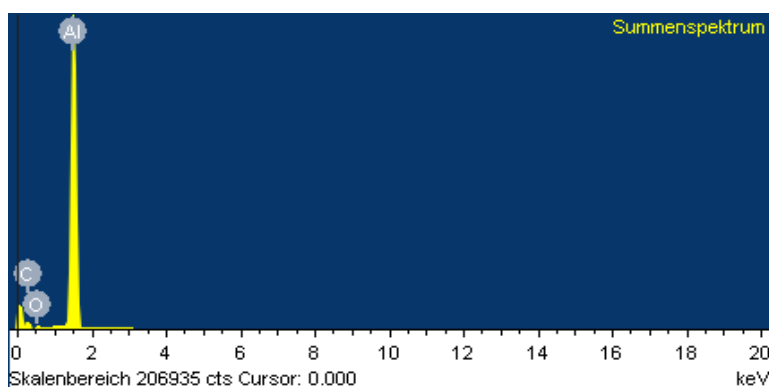


Figure 54: SEM image of with Al PVD plated non-woven polymer

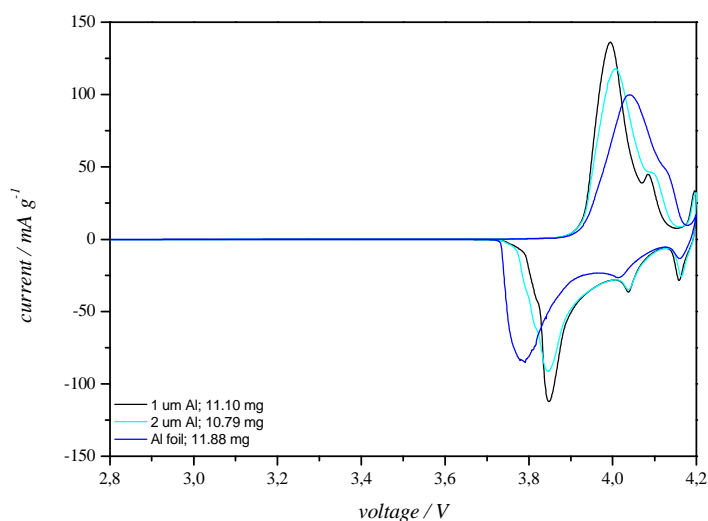


Figure 55: CV measurement (scan rate:  $30 \mu\text{V s}^{-1}$ ) of LCO electrodes with two different 3D current collectors compared to aluminium foil as current collector

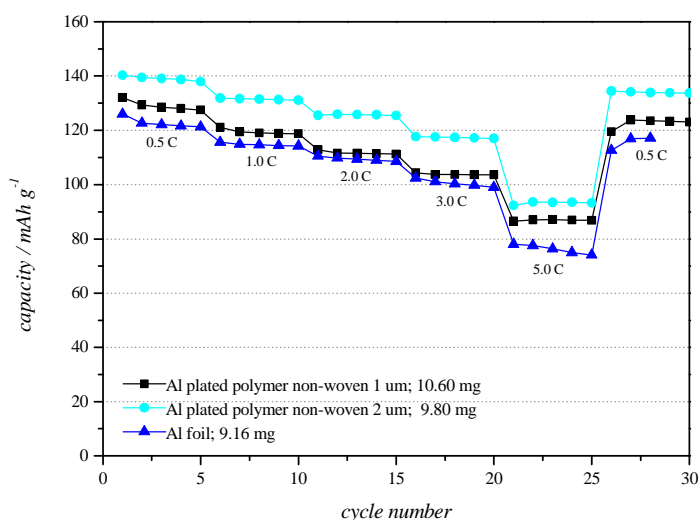


Figure 56: Rate capability tests of LCO electrodes with two different 3D current collectors compared to aluminium foil as current collector

Table 16: Capacities of electrodes with different current collectors at different c-rates from rate capability test (fig.56) and corresponding capacity losses compared to the first cycles

cycle no.	c-rate	1 μm Al layer [mAh g <sup>-1</sup> ]	capacity loss [%]	2 μm Al layer [mAh g <sup>-1</sup> ]	capacity loss [%]	Al foil [mAh g <sup>-1</sup> ]	capacity loss [%]
1.	0.5 C	132		140		126	
11.	2.0 C	113	14	126	10	111	12
16.	3.0 C	104	21	118	16	102	19
21.	5.0 C	87	34	92	34	78	38
26.	0.5 C	120	9	134	4	113	11

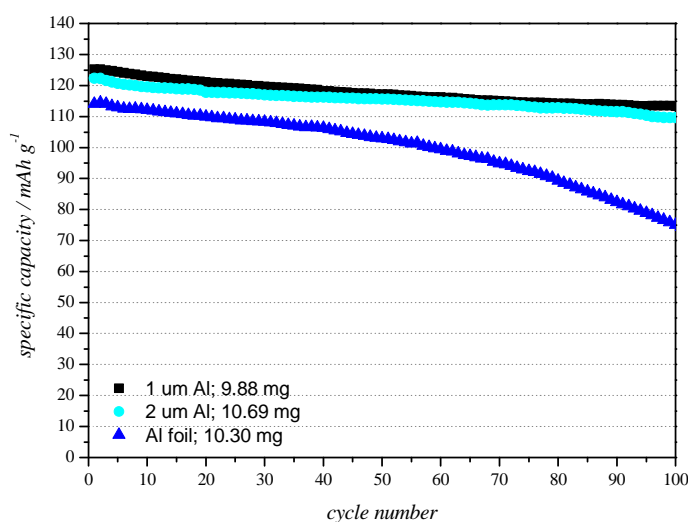
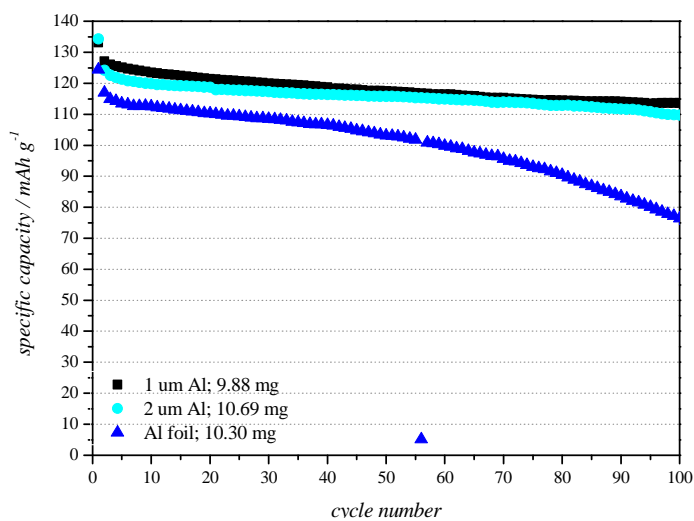


Figure 57: Lithiation capacities (above) and delithiation capacities (below) received from CCC measurement (1 C) of LCO electrodes with 3D current collectors (different Al layer thicknesses) compared to aluminium foil

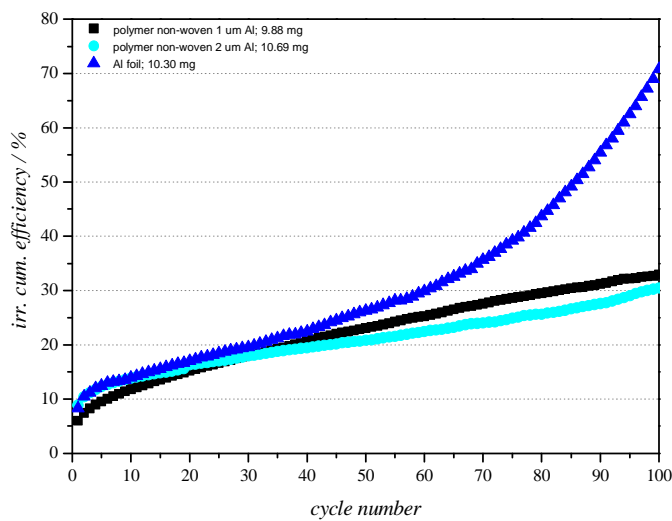


Figure 58: Irreversible cumulative efficiencies of LCO electrodes with two different 3D current collectors and aluminium foil for comparison

The second cycles of the cyclic voltammetric experiment of  $\text{LiCoO}_2$  electrodes with three dimensional current collectors compared to an electrode with aluminium foil as current collector are shown in figure 55. An improvement with 3D current collectors can be achieved as the oxidation- and reduction peaks of LCO are much sharper compared to the 2D current collector. Due to the higher surface area and thereby the better connection between active material and the 3D current collector, the lithium transport at high mass loadings is much faster. Also, an improvement in cycling stability at higher c-rates can be observed with the new current collector (rate capability test figure 56). The capacity loss of electrodes with Al foil as current collector is more tremendous when higher c-rates are applied (table 16). The rapid capacity drop at c-rates beyond 3C can be attributed to increased internal resistances due to non-ideal measurement setup for electrodes with such high masses.

Figure 57 shows a comparison of the lithiation- and delithiation capacities of electrodes with different current collectors. Because of inhomogeneous mass loading into the voids of the 3D current collector, the determination of the exact mass of the electrode and the c-rate is difficult. Therefore, the 2nd lithiation capacity from the cyclic voltammetry experiment was used for the cycling study. With both current collectors the theoretical capacity for half lithiation of  $\text{LiCoO}_2$  of around  $137 \text{ mAh g}^{-1}$  could be reached in the first cycles. As seen in figure 57, the electrodes with the 3D current collectors could reach a remaining capacity of  $110 \text{ mAh g}^{-1}$  after 100 cycles (1.0 C rate) with a capacity loss of 17% and reversibility close to 100%. The remaining capacity of the electrode with the 2D current collector after 100 lithiation- and delithiation cycles was just  $76 \text{ mAh g}^{-1}$  with a capacity loss of 39% (1.0 C rate).

The irreversible cumulative efficiencies of the cycling study are shown in figure 58. The electrode with aluminium foil as current collector had the highest irreversible cumulative efficiency and therefore the highest loss of electrochemical active lithium ions during cycling. This leads to tremendous capacity fade.

Due to limited resources of electrochemically active lithium ions especially in full cells, continuous loss has an adverse effect.

#### 4.2.6.4. Full cell assembling with electrodes composed of 3D current collectors

Graphite anodes and LCO cathodes were prepared, using copper plated (POLYMET® XII-1) and 2<sup>nd</sup> generation aluminium plated non-woven polymer as three dimensional current collectors. These electrodes had dimensions of 15 cm<sup>2</sup> and average capacities of 1.02 mA cm<sup>-2</sup> (anode) and 0.90 mA cm<sup>-2</sup> (cathode), respectively.

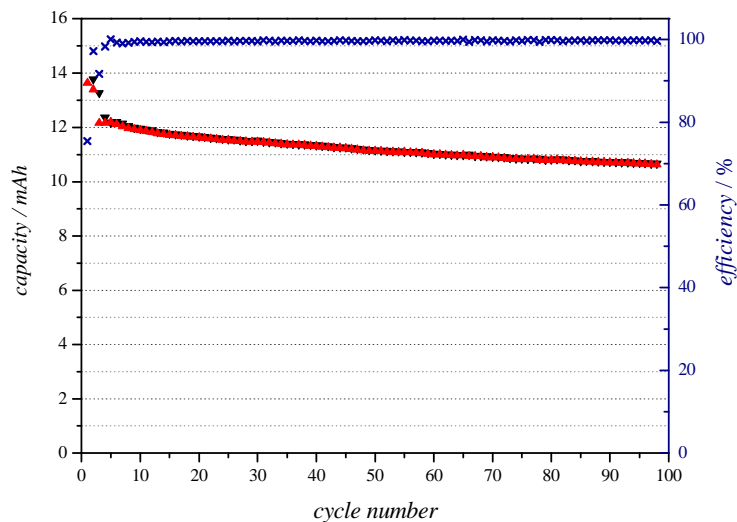


Figure 59: Lithiation- and delithiation capacities received from CCC measurement (0.5 C) of full cells with 3D current collectors. Graphite and LCO were used as active materials.

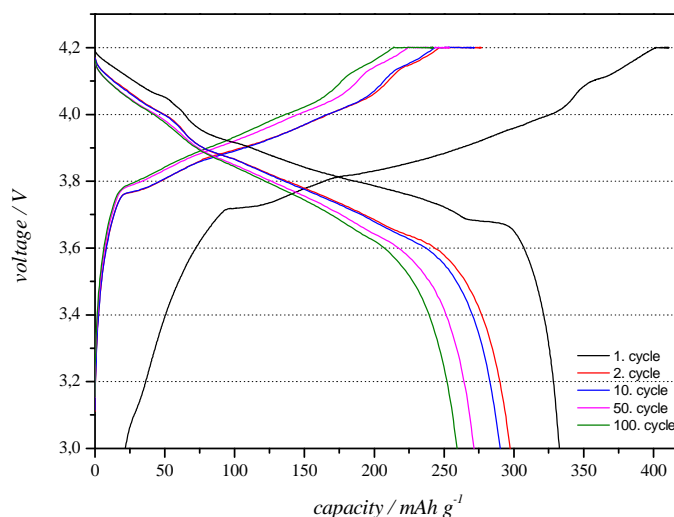


Figure 60: Voltage profiles of lithiation and delithiation received from constant current cycling of full cells with electrodes composed of 3D current collectors. Graphite and LCO were used as active materials.

Figure 59 shows the cycling study of a full cell with electrodes coated on 3D current collectors in pouch bag configuration. In the first few cycles the capacity drop is tremendous. A possible reason is the poor contact between the 3D current collector and current collector tap. The capacity drop between first and second cycle amounted 24%. In contrary, the capacity fade afterwards is 23% during 100 cycles.

The voltage profiles of charging and discharging the full cell are shown in figure 60. It illustrates the impact of lithium ion loss, especially during the first charge and discharge cycle. This vast capacity loss can be mainly attributed to SEI-formation.

Additionally, full cells were prepared by an industrial process.  $\text{LiCoO}_2$ , coated on 2<sup>nd</sup> generation aluminium-plated non-woven polymer was used as cathode and graphite coated on copper foil as anode. The characterisation was carried out in pouch bag configuration with electrode dimensions of 30 mm x 50 mm and a capacity of  $2.10 \text{ mAh cm}^{-2}$ . Figure 61 shows the constant current cycling study of the industrial prepared full cell after one cycle of formation. It depicts, that this cell reveals an excellent cycling stability.

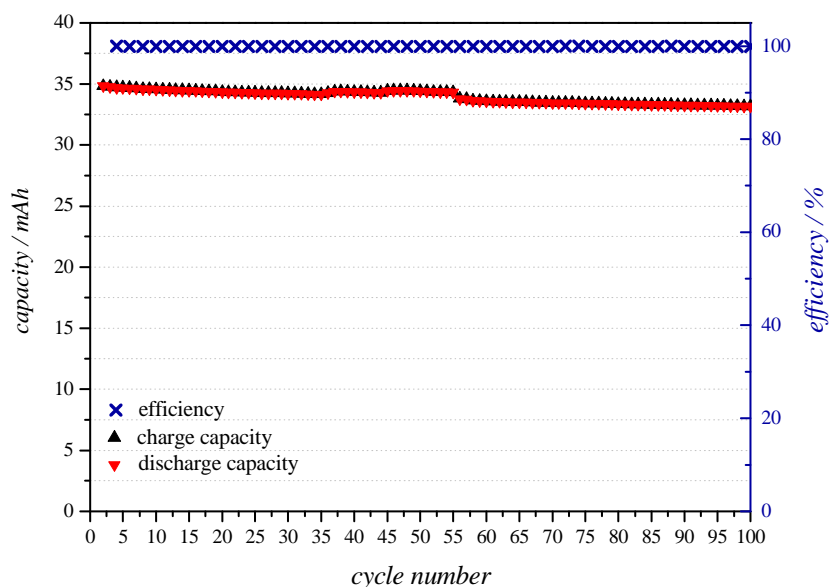


Figure 61: Lithiation- and delithiation capacities received from CCC measurement (0.1 C) of full cells, where LCO coated on the 2<sup>nd</sup> generation 3D current collector was used as cathode and graphite, coated on copper foil as anode.

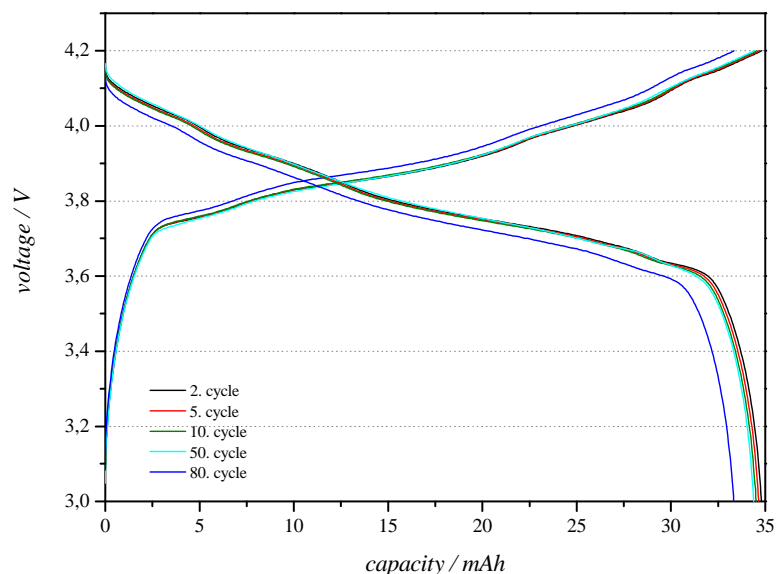


Figure 62: Voltage profiles of lithiation and delithiation received from constant current cycling of full cells, where LCO coated on the 2<sup>nd</sup> generation 3D current collector was used as cathode and graphite, coated on copper foil as anode.

The predicted capacity of the cell could be reached very well. The voltage profile (figure 62) illustrates distinguished capacity retention. After one cycle of formation the capacity fade amounts 4 %. This means, that almost the whole capacity could be retained after 80 charge and discharge cycles.

An explanation for the better performance of the industrial produced full cell compared to the under lab conditions produced full cell is on one hand the optimised production conditions in terms of reproducibility. On the other hand, the improved contact between the 3D current collector and current collector tap could be responsible for the outstanding cycle performance.



#### 4.2.7. Conclusion

Within this doctoral thesis, a novel type of flexible and lightweight three dimensional current collector for the positive electrode of LIBs was developed to replace the widely used heavier flat metal current collectors. Aluminium was successfully deposited on non-woven polymers from an ionic liquid for application as 3D current collector. Active material was embedded into the voids of the 3D current collector and it was found, that such architecture leads to much better cycling performance compared to conventional electrode architecture, with mass loadings in the same range. In addition, the gravimetric energy density of a battery could be improved, when the heavier flat metal substrate is replaced by the novel 3D current collector. However, it contains 50% of the mass of the conventional current collector. Such an aluminium plated current collector can be used with a variety of cathode materials. Another benefit is the reduced effort of metals to save resources.

During aluminium deposition from the imidazolium based ionic liquid, thermal degradation, initiated by  $\text{AlCl}_3$ , could be figured out to be the main reason for electrolyte aging. No evidence for electrochemical decomposition of this electrolyte could be found. The presented analytical approach, combining pyrolysis chromatography coupled with mass spectrometry incorporated and headspace gas chromatography-mass spectrometry enables the identification of decomposition products of ionic liquids.

Thermal degradation of  $\text{EMImCl} \cdot 1.5 \text{ AlCl}_3$  produces chloromethane, dichloromethane, hydrochloric acid, imidazole, alkylimidazole and 1-ethyl-3-methylimidazole based on the formation of a reactive carbene intermediate.  $\text{Cl}^-$  ions are irreversible consumed and the obtained data can be explained by an equilibrium, shifts from excess of reducible Al-species  $[\text{Al}_2\text{Cl}_7]^-$  to excess of the not reducible Al-compound  $[\text{AlCl}_4]^-$ . Another consideration that has to be taken into account is the potential drift to more negative potentials during electroplating, until the limit of the electrochemical stability window of IL is exceeded. All these factors will contribute to irreversible decomposition of ionic liquid and damage of the plating bath.

Physical vapour deposition of aluminium has been scaled up to meet industrial requirements and mass production of lightweight and flexible current collectors for the cathode of LIBs is potentially feasible [102].

### 4.3. SYNTHESIS OF AN ACTIVE MATERIAL FOR THE NEGATIVE ELECTRODE BASED ON SILICON AND DECOMPOSABLE POLYMERS

To meet the ever increasing demands in energy density for various applications, graphite has to be replaced by anode materials with higher theoretical capacities. Silicon is a prominent candidate as active material for the anode with a theoretical capacity of  $4200 \text{ mAh g}^{-1}$  [49]. However, this electrode material exhibits a few difficulties. During repeated alloying and de-alloying processes, silicon undergoes massive volume expansions followed by cracking and disintegration of the electrode. This leads to poor cycle performance and significant capacity loss [103] [104]. Characteristics, benefits and problems of silicon as active material for the negative electrode are discussed more in detail in chapter 3.3.2. Although numerous research groups are dedicated to this problem and many efforts have been made up to date but no commercially viable silicon anode had been attained until now [103].

Several strategies have been developed to improve the cycling performance of silicon-based anodes (chapter 3.3.2.). In this work, Si/C composites were prepared through high-temperature pyrolysis. Nano-silicon particles were embedded in a matrix of carbon, based on graphite and decomposable polymers as adhesive.

Three types of polymers were used:

#### 1. PolyHIPE

This polymer was prepared by ring opening metathesis polymerisation (ROMP) of dicyclopentadiene (DCPD) [105].

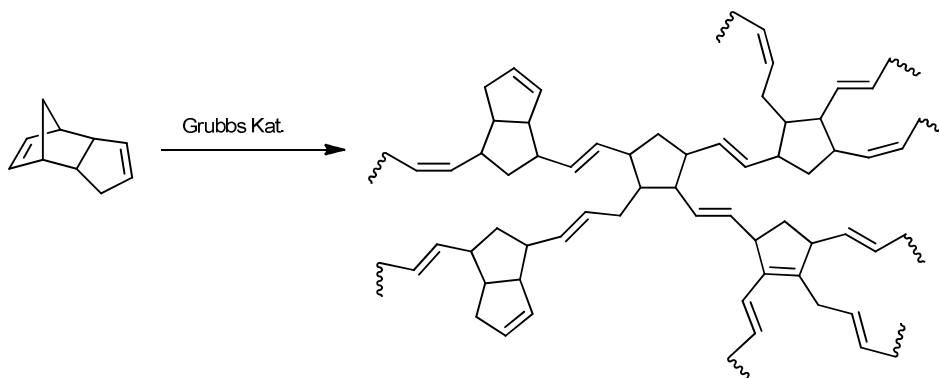


Figure 63: Reaction equation of polymerisation of DCPD via ROMP [105]

2. Polydicyclopentadiene (PDCPD)

The polymerization of PDCPD was initiated by a cationic system, using  $AlCl_3$  [106].

3. Polymethyl methacrylate / Polyethyleneglycol dimethacrylate

A crosslinked polymer was prepared by radical chain polymerisation, using benzoyl peroxide (BPO) as initiating agency [107] [108] [109].

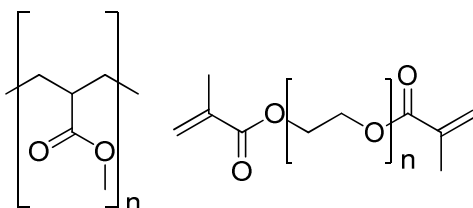


Figure 64: Structures of polymethyl methacrylate (left) [129] and polyethyleneglycol dimethacrylate [108]

4.3.1. PolyHIPE as decomposable polymer for preparation of Si/C composites

PolyHIPE, synthesised from DCPD (figure 63) exhibits a typical architecture with cavities and interconnecting pores [105]. The results from TG/DSC-MS measurement (figure 65) show, that decomposition of the polymer takes place at 773 K. At 973 K, the whole polymer is converted into carbon. When the temperature is further increased, no significant mass loss is observable. After decomposition, about 30% carbon can be obtained from PolyHIPE. According to the mass spectra, the main decomposition products are  $H_2O$ ,  $O^{2+}$ ,  $CO_2$ ,  $CH_3^+$  und  $OH^-$ .

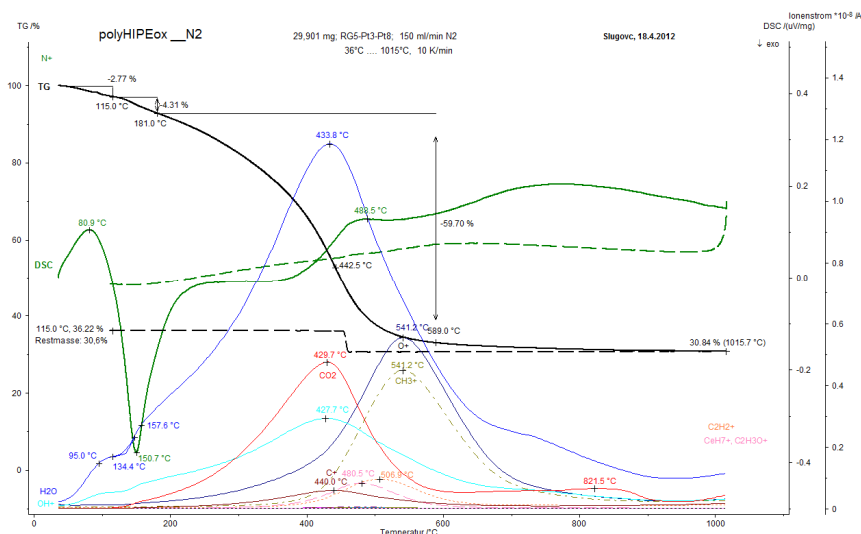


Figure 65: TG/DSC-MS curve for thermal decomposition of polyHIPE (provided by Sebastijan Kovacic)

For preparation of active material, 40% nano-silicon (Nanostructures and Amorphous Materials Inc., 50-70 nm) was encapsulated in the porous structure of the polymer during polymerisation. The raw material was provided by Sebastijan Kovacic from Institute for Chemistry and Technology of Materials at TU Graz. The polymer was dried and ball milled before it was dispersed in acetone with different ratios of graphite (Qingdao). Decomposition was carried out at 1173 K for 2 hours under argon atmosphere. The mass loss after thermal decomposition gradually increased with increasing amount of polymer (18.6 % for the ratio 30% Si/polyHIPE and 70% graphite, 24.5% for 40:60 and 31.7% for 50:50). Due to inhomogeneous distribution the determination of the real amount of silicon in the active material is critical. For electrochemical characterisation an electrode slurry was prepared (table 17) and it was coated on copper foil by doctor blade method, pre-dried at 333 K (air) and finally dried at 393 K under vacuum ( $10^{-3}$  mbar) for 24 h.

Table 17: Electrode slurry composition

	components	composition [%]
active material	Si/C	88
binder	NaCMC	7
conducting additive	carbon nano tubes	5
solvent	H <sub>2</sub> O	

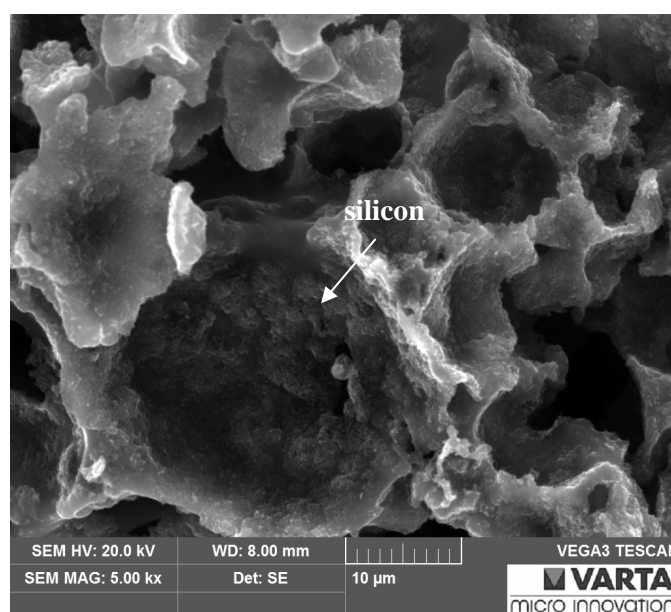


Figure 66: SEM image of the active material (polyHIPE with silicon)

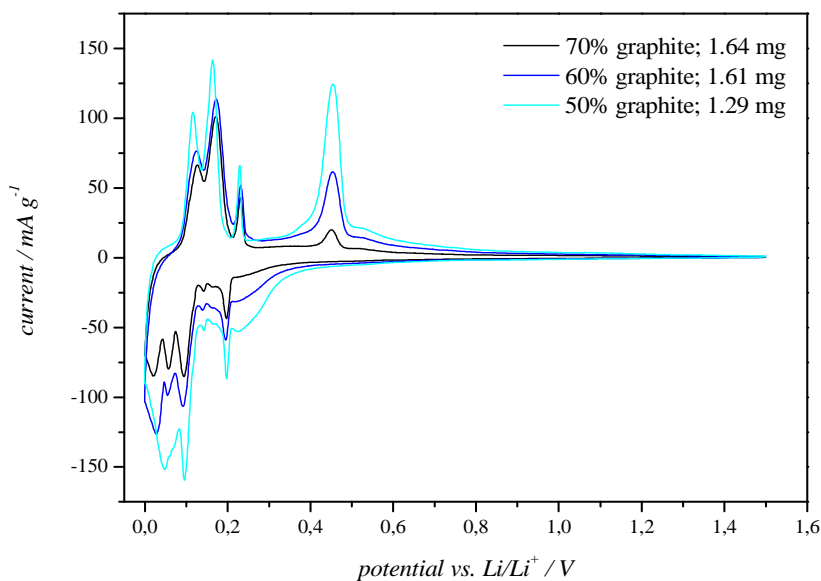


Figure 67: CV measurement (second cycles; scan rate: 10 μV s<sup>-1</sup>) of electrodes with three different graphite contributions

Table 18: Comparison of the theoretical and practical capacity of active material with different graphite contributions

graphite contribution [%]	theoretical capacity [mAh g <sup>-1</sup> ]	practical reached capacity [mAh g <sup>-1</sup> ]	[%] of theoret. capacity reached
70	981	589	60
60	1268	615	49
50	1542	814	53

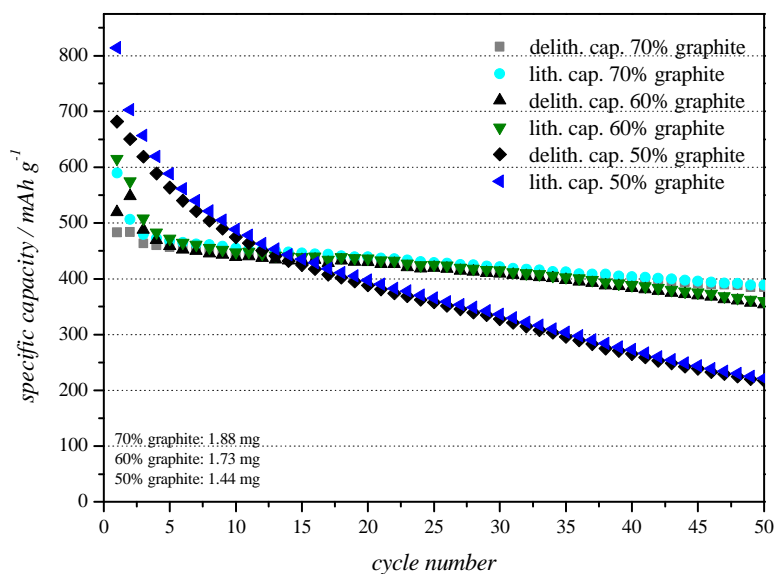


Figure 68: Comparison of CCC of active material with different graphite/silicon ratios; c-rate: 0.5 C

Figure 67 shows the second cycles from CV measurement for different graphite contributions. The reduction peaks, appearing in the potential range between 0.0-0.3 V correspond to the insertion of lithium ions into the silicon/graphite host structure. The anodic peak at around 0.4 and 0.5 V could be attributed to the de-alloying process of  $\text{Li}_x\text{Si}$  alloys [110] [111]. It is obvious that this peaks are increasing with decreasing graphite content.

Constant current cycling of active material with different graphite/silicon ratios is shown in figure 68. As expected, the higher the silicon content the more tremendous becomes the capacity fading. Table 18 shows, that the practically reached capacity is about 50-60% lower than the calculated theoretical capacity of these active materials. It is believed, that during manufacturing process of the polymer, active silicon may be turned into inactive silicon components like  $\text{SiO}_x$  or  $\text{SiC}$ . Therefore, no further investigations were carried out with Si/C composites based on polyHIPE as decomposable polymer.

#### 4.3.2. Polydicyclopentadiene as decomposable polymer for preparation of Si/C composites

DCPD was polymerised by a cationic initiating system ( $\text{AlCl}_3$  dissolved in dichloromethane). The monomer contains two polymerisable double bonds, the norbornenic and the cyclopentenic double bonds [112]. PolyHIPE is produced by ring opening polymerisation, whereas in this case the polymerisation was carried out through breaking the double bonds. Investigations have found, that structural units, produced during polymerisation, are depending on the solvent used [112] (figure 69).

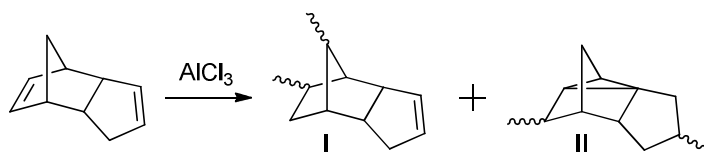


Figure 69: Predicted structural units produced during polymerisation of DCPD with  $\text{AlCl}_3$  in  $\text{CH}_2\text{Cl}_2$

The polymerisation was carried out in a glass flask under argon atmosphere. The monomer was dissolved in dichloromethane and the polymerisation was initiated by adding 0.015 M  $\text{AlCl}_3$ .

The solution was stirred for 15 min. at room temperature before a mixture of nano-silicon and graphite (Qingdao) was added. After 200 hours, PDCPD was precipitated by adding an excess of methanol and the obtained solid was washed with methanol and dried to constant weight [112]. Afterwards the polymer/Si/graphite mixture was pyrolysed under argon atmosphere at 1173 K for 2 hours with a heating rate of 5 K min<sup>-1</sup>. For characterisation, PDCPD was produced without silicon/graphite mixture according to the previous procedure.

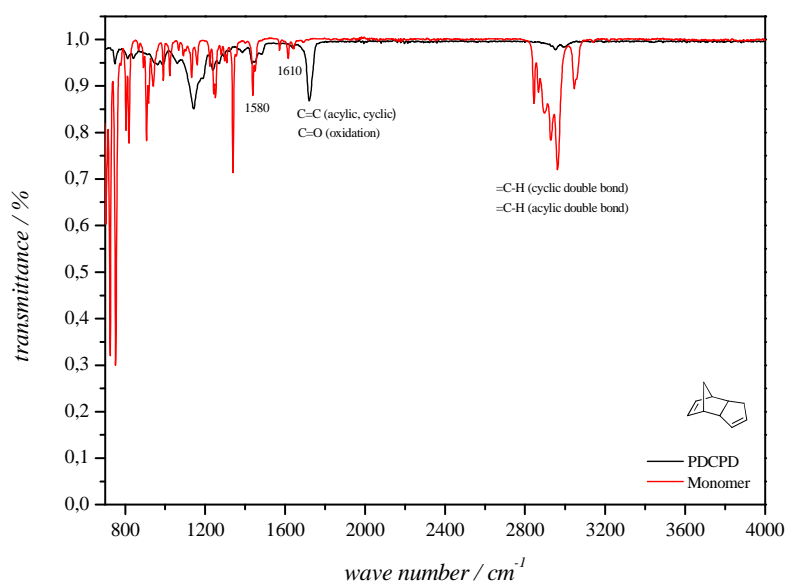


Figure 70: FTIR-ATR spectra of DCPD and PDCPD prepared in CH<sub>2</sub>Cl<sub>2</sub>

FTIR-ATR spectra of the polymer in comparison to the monomer are shown in figure 70. The signals at 1610 cm<sup>-1</sup> can be attributed to the cyclopentenic double bond and the vibration at 1580 cm<sup>-1</sup> to the norbornenic double bond [112]. The weak signal between 2800 and 3200 cm<sup>-1</sup> in the spectrum of PDCPD indicates, that most of the double bonds are broken, which is evidence for the presence of unit II (figure 69). The signal at 1700 cm<sup>-1</sup> might indicate the rapid oxidation of the polymer on air.

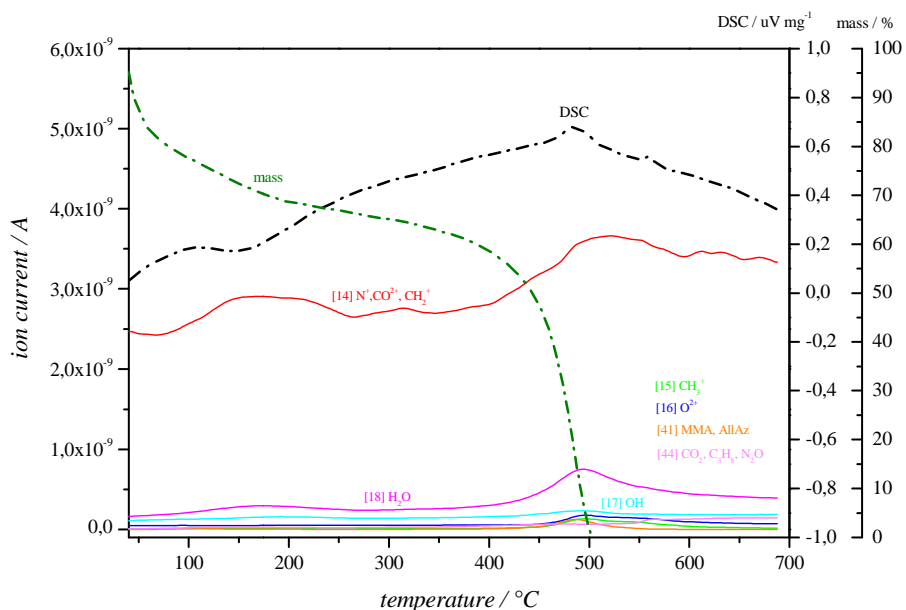


Figure 71: TG/DSC-MS curve for thermal decomposition of PDCPD

According to TG/DSG-MS measurement (figure 71), a two step reaction is occurring during thermal decomposition of PDCPD. The first step occurs at 423 K, which can be contributed to decomposition of remaining monomer. The second step at 773 K can be assigned to conversion of the polymer into carbon black. After pyrolysis, 13-17% carbon black could be obtained from the polymer. The main decomposition products are CO, H<sub>2</sub>O, OH<sup>-</sup> and CH<sup>2+</sup>.

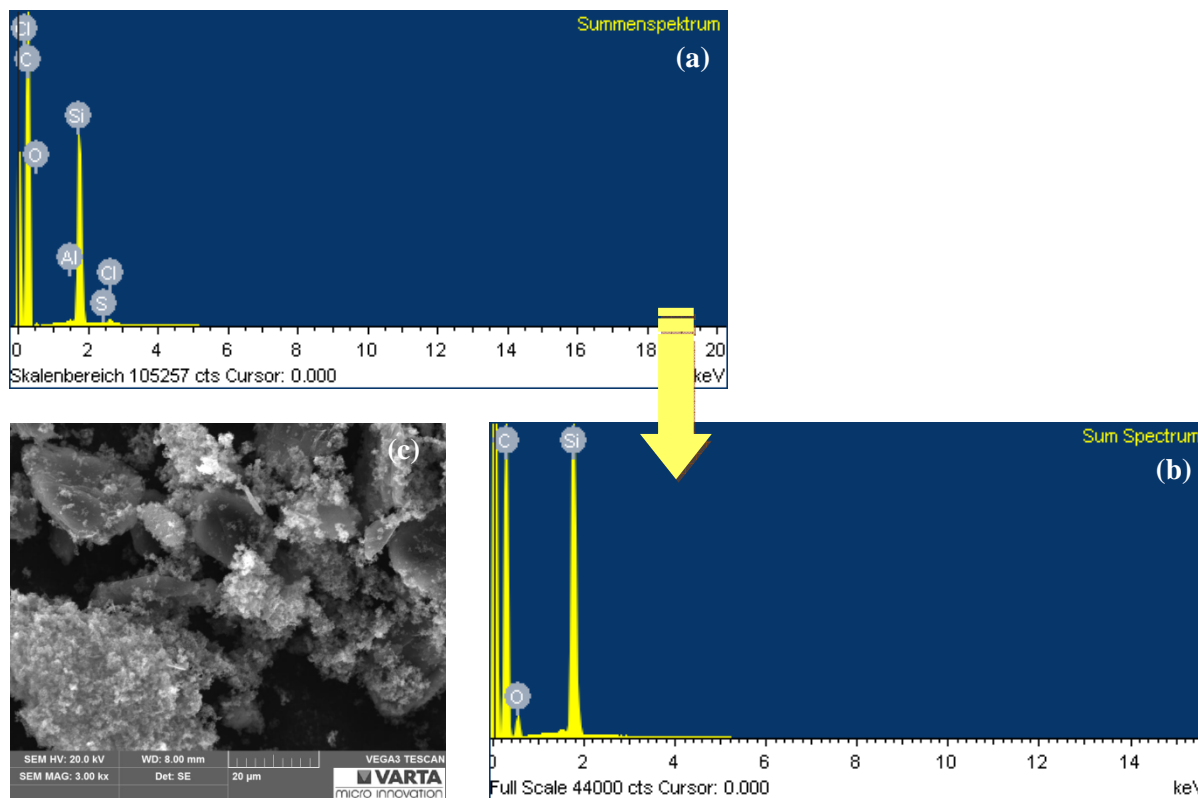


Figure 72: EDX spectra of the active material before (a) and after (b) pyrolysis and SEM image of the active material after pyrolysis (c)



The EDX analysis of the Si/C composite before pyrolysis indicates the presence of impurities (Al, Cl, S), that can be attributed to the initiating system of the polymerisation (figure 72a). As revealed in the EDX spectrum of the material after pyrolysis (figure 72b), all impurities disappear. Figure 72c shows a SEM image of the active material after decomposition of the polymer at 1173 K. Graphite particles, coated with a mixture of nano-silicon and amorphous carbon can be identified.

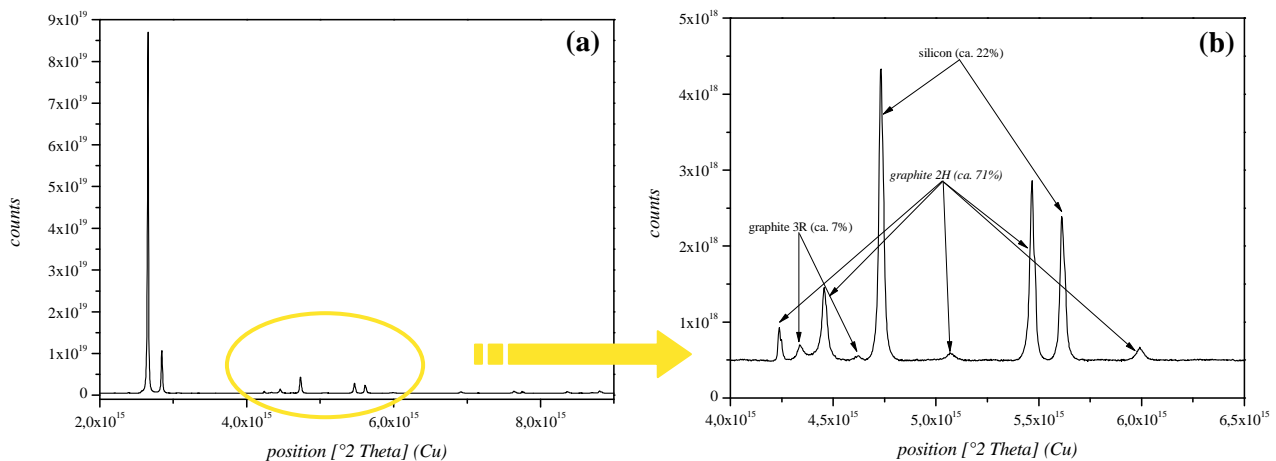


Figure 73: XRD spectra of Si/C composite with PDCPD as decomposable polymer after pyrolysis at 1173 K; full spectrum (a) and detailed view (b)

In the XRD spectra of active material after decomposition (figure 73) no indication for the formation of electrochemical inactive silicon compounds like SiC or SiO<sub>x</sub> can be found. As stated in literature, SiC formation takes place even at relative low temperatures of around 1173 K, mainly influenced by the chemical composition of the decomposable polymer [113] [114] [115] [116]. For the calculation of the specific capacity of the active material it is important to know the amount of SiC since it is an electrochemically inactive compound.

An electrode slurry was prepared (table 17), copper foil was coated with the slurry by doctor blade method, predried at 333 K (air) and finally dried at 393 K under vacuum (10<sup>-3</sup> mbar) for 24 h. Several active materials were prepared with variation of different parameters, like silicon content and particle size of the nano-silicon particles (table 19).

Table 19: Different active materials with DCPD as decomposable polymer, prepared for electrochemical characterisation

		ratio si:graphite:C	si particle size
50% DCPD	50% Si/graphite/C	20:80:0	50-70 nm
50% DCPD	50% Si/graphite/C	20:70:10	30-50 nm
50% DCPD	50% Si/graphite/C	20:80:0	30-50 nm
50% DCPD	50% Si/graphite/C	30:60:10	30-50 nm
50% DCPD	50% Si/graphite/C	30:70:0	30-50 nm

#### 4.3.2.1. Active material with a silicon:graphite ratio of 20:80 and silicon particle size of 50-70 nm

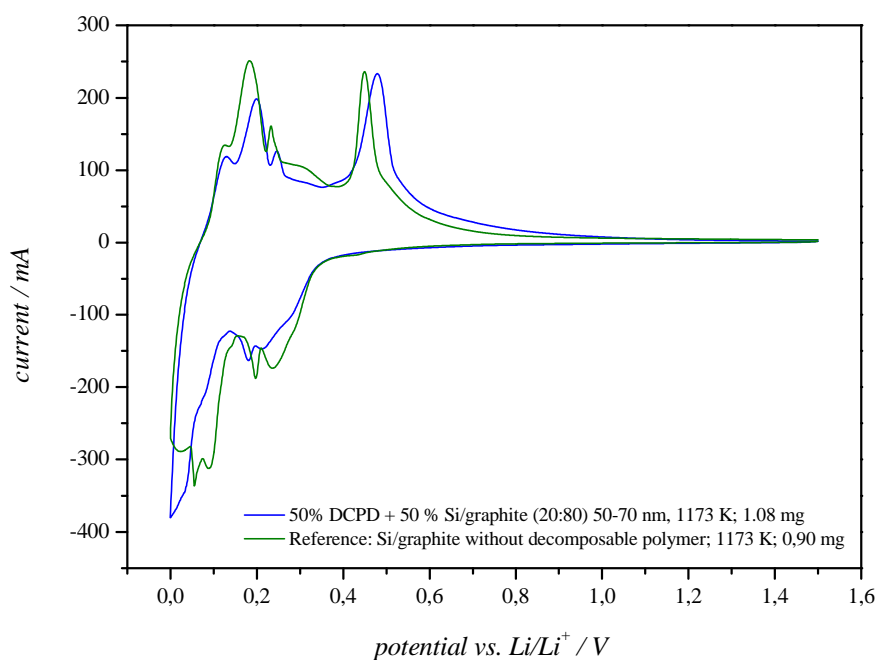
Figure 74: CV measurement (scan rate:  $30 \mu\text{V s}^{-1}$ ) of active material composed of PDCPD and silicon/graphite (20:80) with silicon particle size of 50-70 nm

Table 20: Corresponding lithiation and delithiation capacities of the second cycle of CV measurement (figure 74)

	delith. cap./mAh $\text{g}^{-1}$	lith. cap./mAh $\text{g}^{-1}$	rev/%	mass/mg
<b>Si/gra 20:80; 1173 K</b>	708.1	737.6	96.0	1.08
<b>reference</b>	694.2	773.5	89.7	0.90

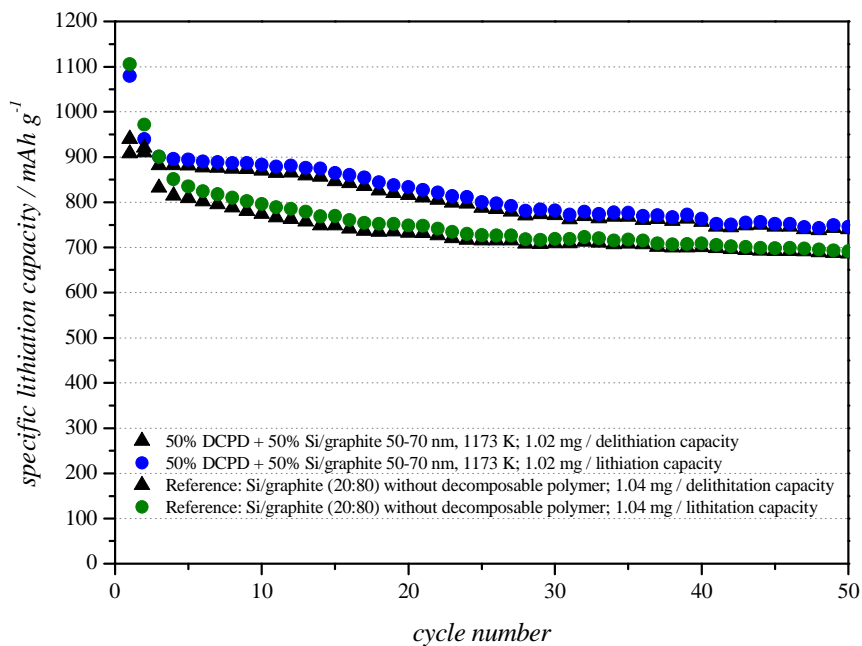


Figure 75: CCC measurement (0.5 C) of active material composed of PDCPD and silicon/graphite (20:80) with silicon particle size of 50-70 nm

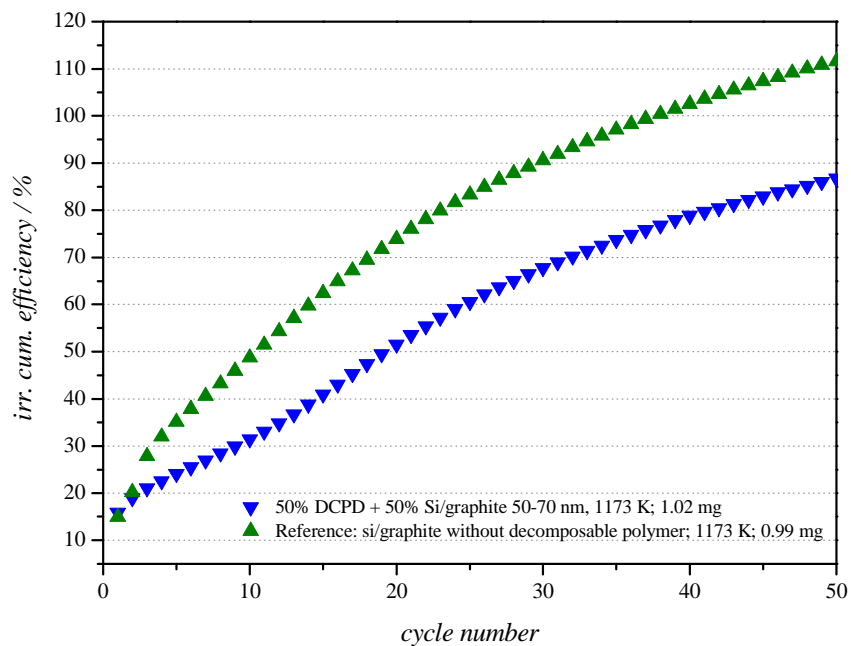


Figure 76: Irreversible cumulative efficiency of active material based on DCPD and Si/graphite (20:80) with silicon particle size of 50-70 nm

As shown in the cyclic voltammogram (figure 74), the oxidation peak of silicon (0.4 – 0.5 V vs. Li/Li<sup>+</sup>) is very distinctive after heat treatment of the active material at 1173 K. Therefore it is assumed, that no inactive silicon compounds were formed during heat treatment. The lower capacity compared to the constant current cycling study can be explained by the higher current load during the CV measurement. A reversible capacity (0.5 C) of 850 – 900 mAh g<sup>-1</sup> could be achieved with this composition during the first 25 cycles and it is slightly higher compared to the reference. A possible explanation is the improved connection between the particles when the active material is embedded in a carbonaceous matrix through decomposition of a polymer. The capacity fade during 50 cycles is 19% for the active material with decomposable polymer and 27% for the reference material. Figure 76 shows the irreversible cumulative efficiencies of the cycling studies. The lowest irreversible cumulative efficiency and therefore the best capacity retention exhibits the electrode with the new silicon/graphite composite.

The calculation of the theoretical achievable capacity is critical due to losses of silicon and graphite during different preparation steps. Therefore, the accurate amount of polymer couldn't be determined. When the polymerisation of DCPD was carried out without a mixture of silicon and graphite, about 60% of the monomer was converted into the polymer.

After decomposition of polymer without silicon and graphite, a carbon yield of about 15% could be achieved, independent of the decomposition temperature. Therefore, the real amount of polymer and the carbon content after decomposition could just be estimated. The mass loss during decomposition at 1173 K comes to 32%.

### 4.3.2.2. Active materials with a silicon:graphite:C ratio of 20:80:0 and 20:70:10 and silicon particle size of 30-50 nm

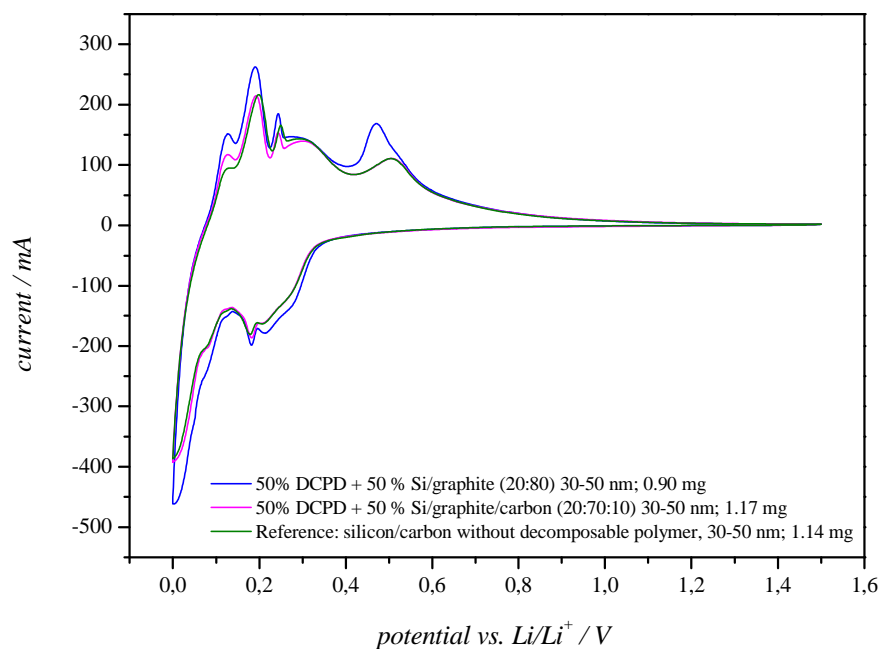


Figure 77: Second cycles of CV measurement (scan rate:  $30 \mu\text{V s}^{-1}$ ) of active materials composed of PDCPD and silicon/graphite (20:80) with silicon particle size of 30-50 nm, pyrolysed at 1173 K

Table 21: Corresponding lithiation and delithiation capacities of the second cycle of CV measurement (figure 77)

	delith. cap./mAh $\text{g}^{-1}$	lith. cap./mAh $\text{g}^{-1}$	rev./%	mass/mg
<b>Si/gra 20:80; 1173 K</b>	915.5	950.2	96.3	0.90
<b>Si/gra/C 20:70:10; 1173 K</b>	723.8	774.4	93.5	1.17
<b>Reference</b>	632.5	673.0	94.0	1.14

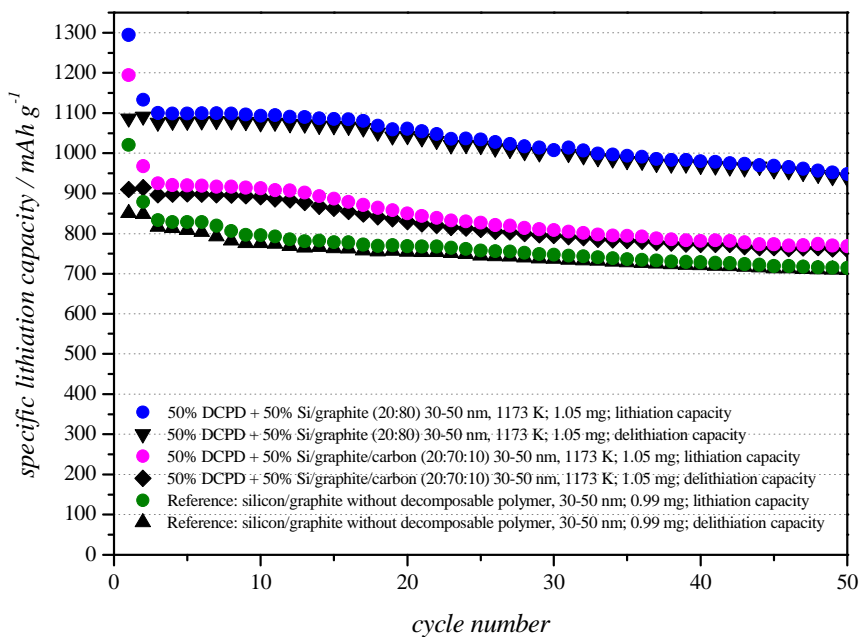


Figure 78: CCC measurement (0.5 C) of active materials composed of PDCPD and silicon/graphite (20:80) with silicon particle size of 30-50 nm, pyrolysed at 1173 K

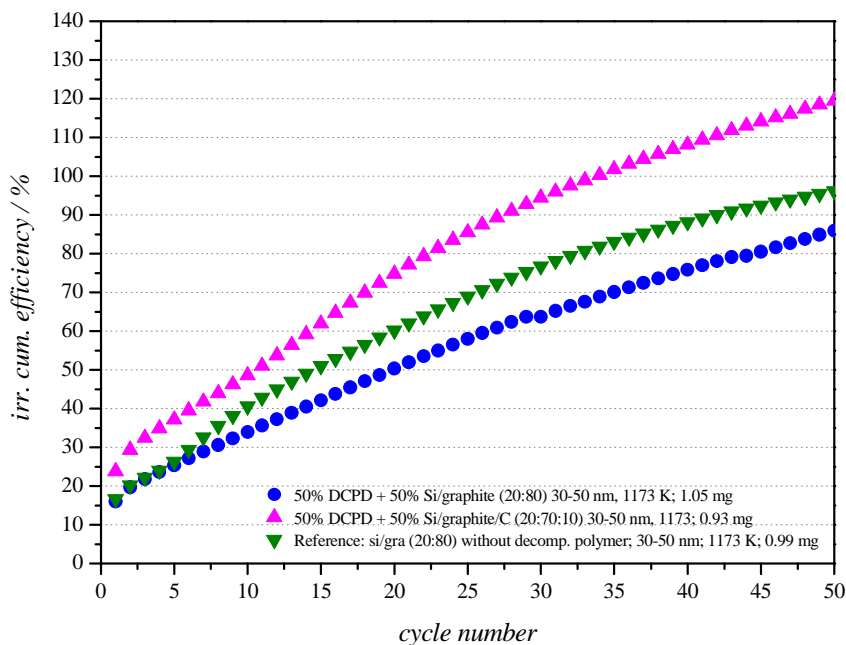


Figure 79: Irreversible cumulative efficiencies of active materials based on DCPD and Si/graphite (20:80) with silicon particle size of 30-50 nm

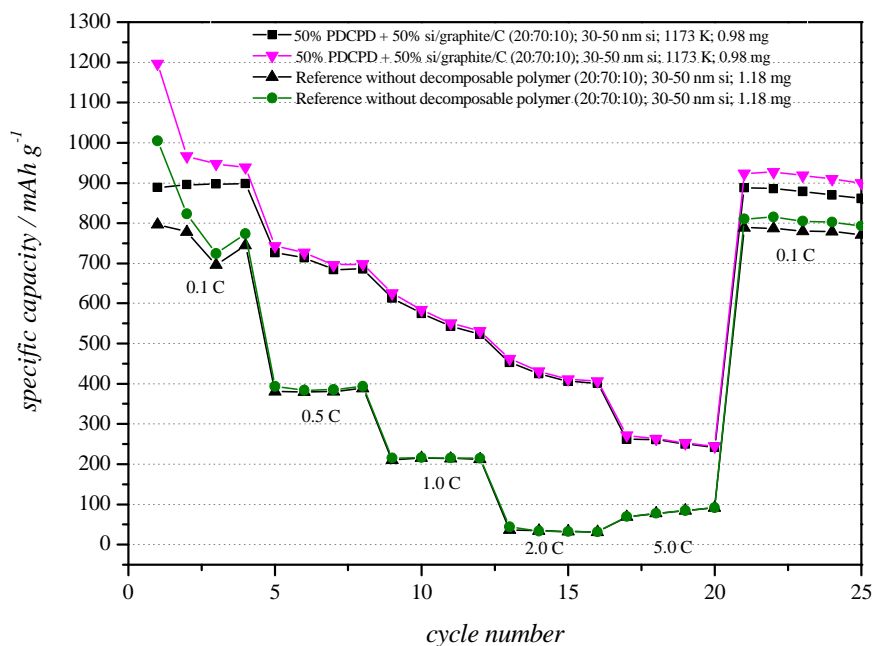


Figure 80: Rate capability test of active materials based on DCPD and Si/graphite/C (20:70:10) with silicon particle size of 30-50 nm

As stated in chapter 4.3.2.1., the calculation of the theoretical capacities of the active materials is quite complicated. The mass loss of the active material with 10% carbon content amounts 4%, whereas the mass loss of active material without addition of amorphous carbon is at least 16% after decomposition at 1173 K.

The active material composed of silicon/graphite 20:80 and pyrolysed PDCPD shows the highest reversible lithiation- and delithiation capacities with the slightest capacity fade (13% over 50 cycles) and the lowest irreversible cumulative efficiency (figure 78 and figure 79). This also applies for the rate capability test (figure 80).

The capacity fade of the other material, where amorphous carbon was added is comparable (15%). This material shows lower reversible lithiation- and delithiation capacities as well as the highest irreversible cumulative efficiencies. The results of the rate capability tests continue this trend.

The worst performance is delivered by the reference electrode. It contains no decomposable polymer for cushioning the volume expansion of silicon during lithiation. It shows the lowest capacities as revealed in the cycling study and in the rate capability test.

As the results show, smaller nano-silicon particle sizes are more favourable in terms of capacity retention and rate capability. Therefore, further active materials were prepared with nano-silicon with a particle size of 30-50 nm.

4.3.2.3. Active materials with a silicon/graphite:C ratio of 30:70:0 and 30:60:10 after heat treatment at 1173 K

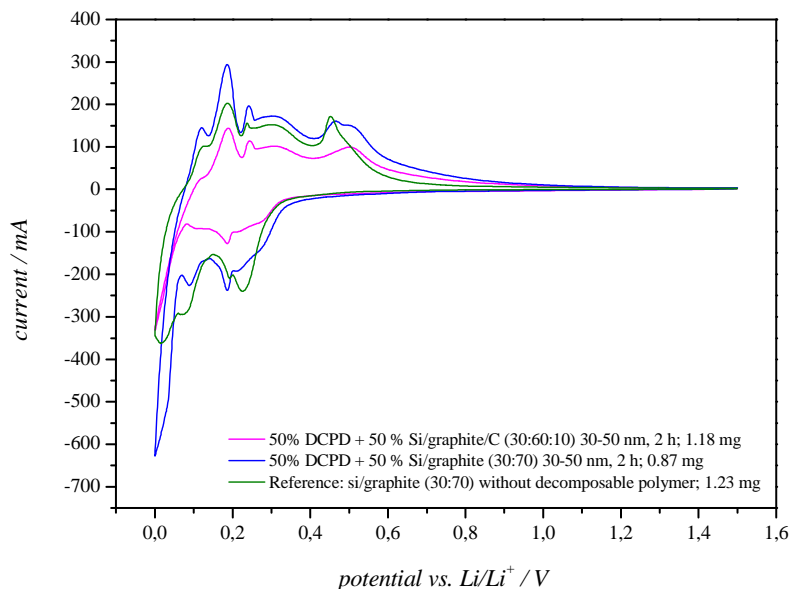


Figure 81: Second cycles of CV measurement (scan rate: 30  $\mu\text{V s}^{-1}$ ) of active materials composed of PDCP and silicon/graphite (30:70) with silicon particle size of 30-50 nm, pyrolysed at 1173 K

Table 22: Corresponding lithiation and delithiation capacities of the second cycles of CV measurement (figure 81)

	delith. cap./mAh g <sup>-1</sup>	lith. cap./mAh g <sup>-1</sup>	rev./%	mass/mg
<b>Si/gra/C (30:60:10)</b>	482.7	519.9	92.8	1.18
<b>Si/gra (30:70)</b>	843.7	897.4	94.0	0.87
<b>reference</b>	703.7	824.1	85.4	1.23

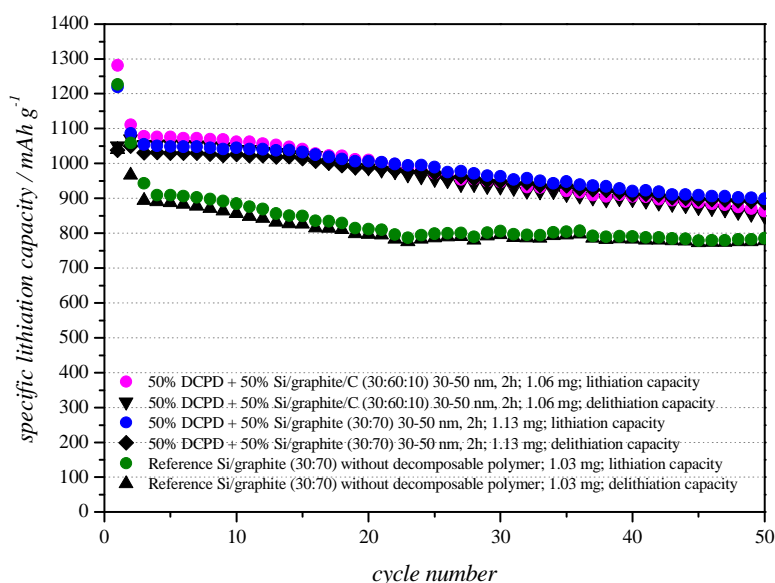


Figure 82: CCC measurement (0.5 C) of active materials composed of PDCPD and silicon/graphite (30:70) and silicon/graphite/C (30:60:10) with silicon particle size of 30-50 nm, pyrolysed at 1173 K



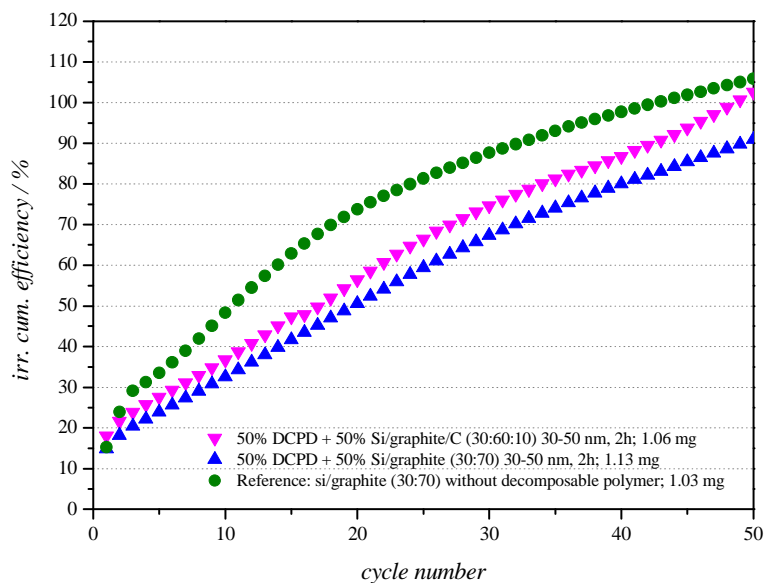


Figure 83: Irreversible cumulative efficiencies of active materials based on DCPD and Si/graphite (30:70) and Si/graphite/C (30:60:10) with silicon particle size of 30-50 nm, pyrolysed at 1173 K

As mentioned before, the determination of the capacity of this active material is difficult, due to material losses during different polymerisation steps and unknown amount of carbon, that is formed during heat treatment at 1173 K. Figure 82 reveals the reversible lithiation- and delithiation capacities of active material composed of a mixture of PDCPD and silicon/graphite/carbon 30:60:10 and silicon/graphite 30:70, respectively.

The lowest capacity fade during 50 cycles exhibits the material composed of silicon/graphite 30:70 and decomposed PDCPD with 15% followed by the carbon containing material with a capacity fade of 20%, while the capacity fade of the reference material amounts 25%. The irreversible cumulative efficiencies continue this trend (figure 83).

Comparison of the results:

According to the results the lowest irreversible cumulative efficiencies can be achieved with active material without addition of carbon black. Also reduction of nano-silicon particle size has a positive effect on cyclability and capacity retention. The best results and lowest capacity fade can be achieved with the material composed of 30-50 nm silicon particles and a silicon to graphite ratio of 20:80, pyrolysed at 1173 K for two hours. Increasing the amount of nano-silicon doesn't lead to higher capacity but raises the capacity fade and negatively influences the capacity retention at higher rates.

An advantage of this polymer is the cheap raw material and the good carbon yield after polymerisation. A disadvantage is the toxicity of the monomer.

### 4.3.3. Polymethyl methacrylate/polyethylenglycol dimethacrylate as decomposable polymer for preparation of Si/C composites

The polymer was prepared via in-situ bulk polymerisation, using a radical chain initiating system. Ethylenglycol dimethacrylate acted as cross-linking agent. The synthesis was carried out in a glass flask under argon atmosphere by mixing the monomers (50 mol% of MMA and 50 mol% of EGDMA) together with 0.1 weight% of the radical chain starter (BPO) and a nano-silicon/graphite mixture. The ratio of monomer mixture and nano-silicon/graphite mixture was 67:33 w/w. The mixture was allowed to polymerise for 3 hours at 358 K. Afterwards the polymer/silicon/graphite mixture was post-cured at room temperature for 48 hours under vacuum [117] [118]. Polymer/Si/graphite mixtures with different ratios of nano-silicon and graphite were prepared (table 23) and these mixtures were heat treated under argon atmosphere at 1173 K for 2 hours with a heating rate of 5 K min<sup>-1</sup>. For characterisation the polymer was produced without silicon/graphite mixture according to the previous procedure.

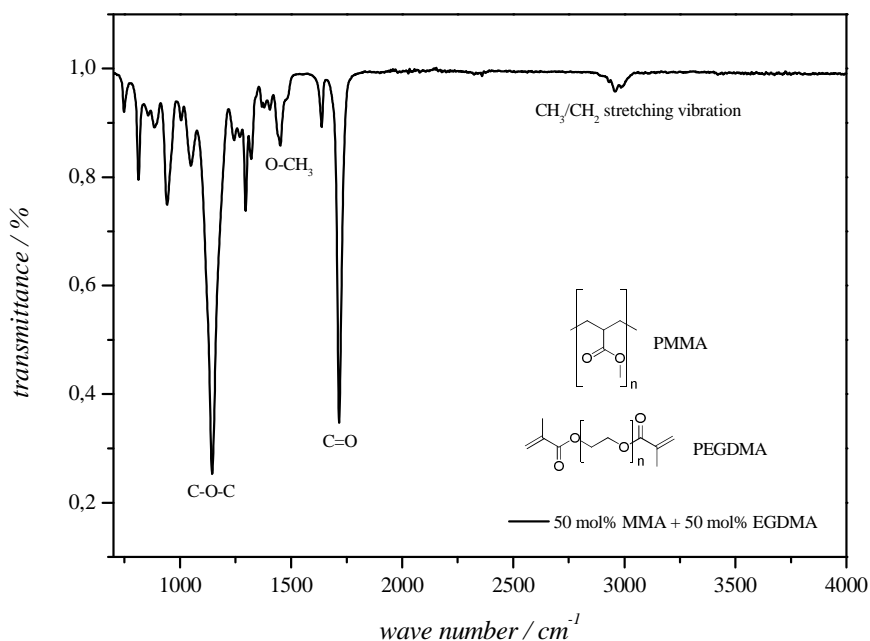


Figure 84: FTIR-ATR spectrum of 50 mol% MMA and 50 mol% EGDMA prepared via in-situ bulk polymerisation

A FTIR-ATR spectrum of the polymer without nano-silicon/graphite mixture is shown in figure 84. The range between  $3000\text{ cm}^{-1}$  –  $2800\text{ cm}^{-1}$  contains C-H-stretching vibrations of aliphatic carbon hydrates.

As reported in literature, characteristic vibration bands for PMMA are stretching vibrations of  $\text{CH}_2$  at  $2958\text{ cm}^{-1}$ ,  $2933\text{ cm}^{-1}$  and  $2860\text{ cm}^{-1}$ , alpha-methyl stretching vibrations at  $3000\text{ cm}^{-1}$ ,  $2958\text{ cm}^{-1}$  and  $2930\text{ cm}^{-1}$  and ester-methyl stretching vibrations at  $2995\text{ cm}^{-1}$  and  $2948\text{ cm}^{-1}$ . At  $1730\text{ cm}^{-1}$  a characteristic signal for vibration of the carbonyl group is occurring and in the range between  $1500\text{ cm}^{-1}$  and  $1400\text{ cm}^{-1}$ , bands indicating the appearance of  $\text{O-CH}_3$  can be observed. The signals between  $1300\text{ cm}^{-1}$  and  $1100\text{ cm}^{-1}$  can be accounted to C-O-C vibrations of the ester group [119].

According to TG/DSG-MS measurement (figure 85), a two step reaction was occurring during thermal decomposition of PMMA/PEGDMA. The first step took place at 623 K and could be attributed to decomposition of remaining monomer. The second step at 723 K could be assigned to conversion of polymer into carbon black. At 773 K, the whole polymer was decomposed. After pyrolysis, 4-7% carbon black could be obtained from the polymer. The main decomposition products were  $\text{CO}_2$ ,  $\text{H}_2\text{O}$ ,  $\text{OH}^-$ ,  $\text{CH}^{2+}$ ,  $\text{C}_3\text{H}_8$ , methyl methacrylate (monomer) and allylacetate (figure 85).

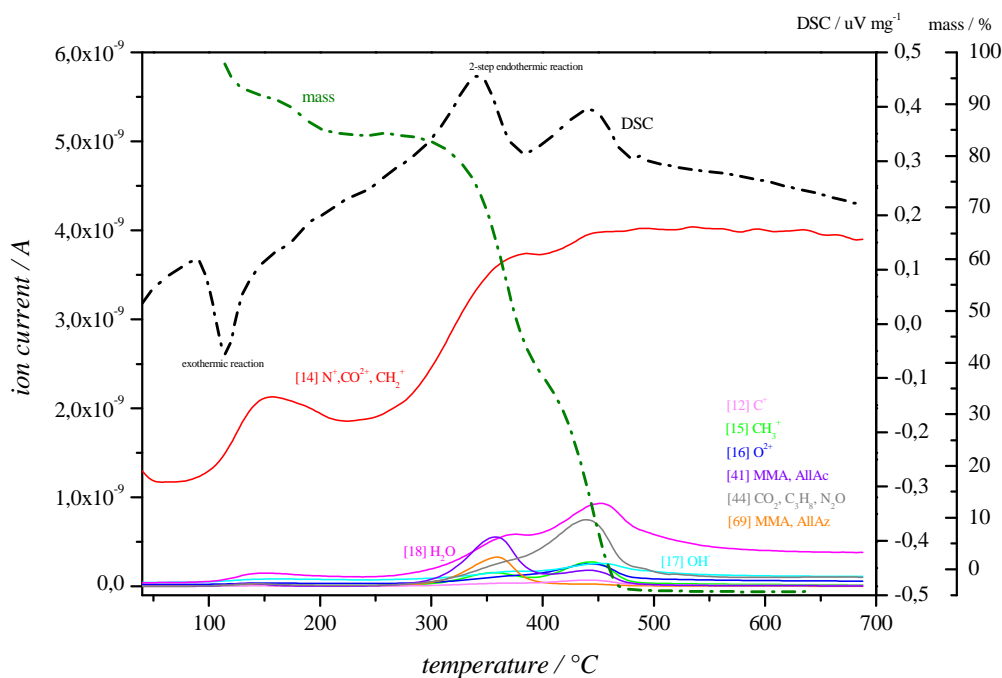


Figure 85: TG/DSC-MS curve for thermal decomposition of PMMA/PEGDMA

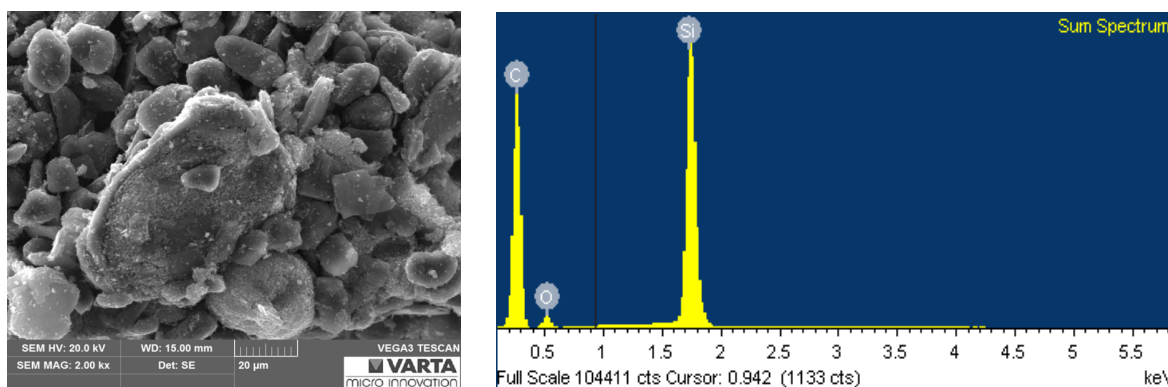


Figure 86: SEM image and EDX spectrum of the active material after pyrolysis

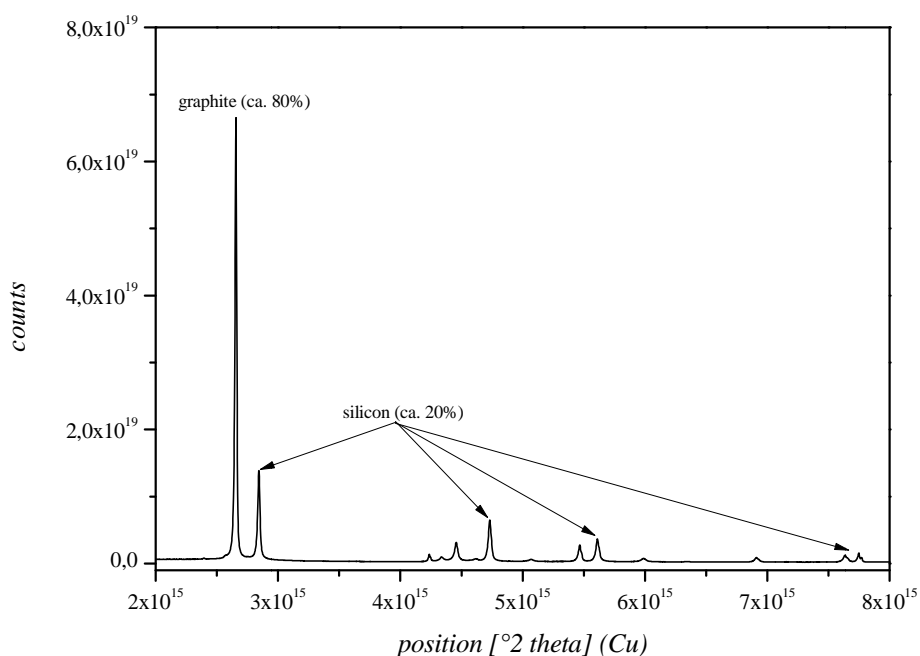


Figure 87: XRD spectrum of Si/C composite with PMMA/PEGDMA as decomposable polymer after pyrolysis at 1173 K and a composition of 80% graphite and 20% nano-silicon (50-70 nm)

Figure 87 shows a XRD spectrum of the active material after decomposition at 1173 K. There is no indication for the formation of electrochemical inactive silicon compounds like SiC or SiO<sub>x</sub> [114]. An electrode slurry was prepared (table 17), it was coated on copper foil by doctor blade method, predried at 333 K (air) and finally dried at 393 K under vacuum (10<sup>-3</sup> mbar) for 24 h. Several active materials were prepared with variation of different parameters, like nano-silicon particle size and silicon to graphite ratio (table 23).

Table 23: Different active materials prepared with MMA/EGDMA as decomposable polymer

		ratio si:graphite:C	si particle size
67% Polymer	33% Si/graphite/C	20:80:0	50-70 nm
67% Polymer	33% Si/graphite/C	20:70:10	30-50 nm
67% Polymer	33% Si/graphite/C	20:80:0	30-50 nm
67% Polymer	33% Si/graphite/C	30:60:0	50-70 nm
67% Polymer	33% Si/graphite/C	30:70:0	30-50 nm
67% Polymer	33% Si/graphite/C	40:60:0	50-70 nm

#### 4.3.3.1. Active material with a silicon/graphite ratio of 20:80 and 50-70 nm silicon particle size

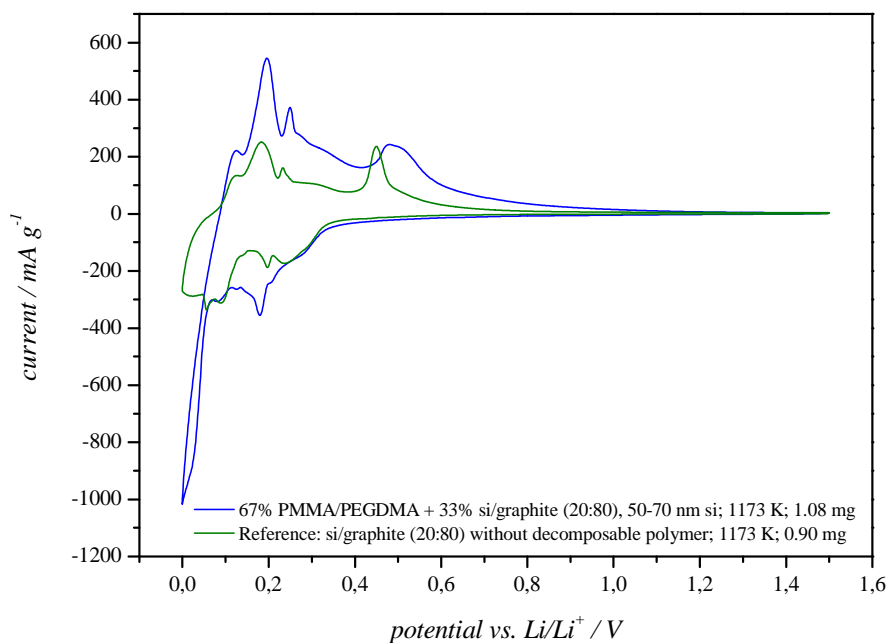


Figure 88: Second cycles of CV measurement (scan rate:  $30 \mu\text{V s}^{-1}$ ) of active material composed of PMMA/PEGDMA and silicon/graphite (20:80) with silicon particle size of 50-70 nm

Table 24: Corresponding lithiation and delithiation capacities of the second cycles of CV measurement (figure 88)

	delith. cap./mAh $\text{g}^{-1}$	lith. cap./mAh $\text{g}^{-1}$	rev./%	mass/mg
Si/gra 20:80, 1173 K	840.3	921.1	91.2	1.08
reference	694.2	773.5	89.7	0.90

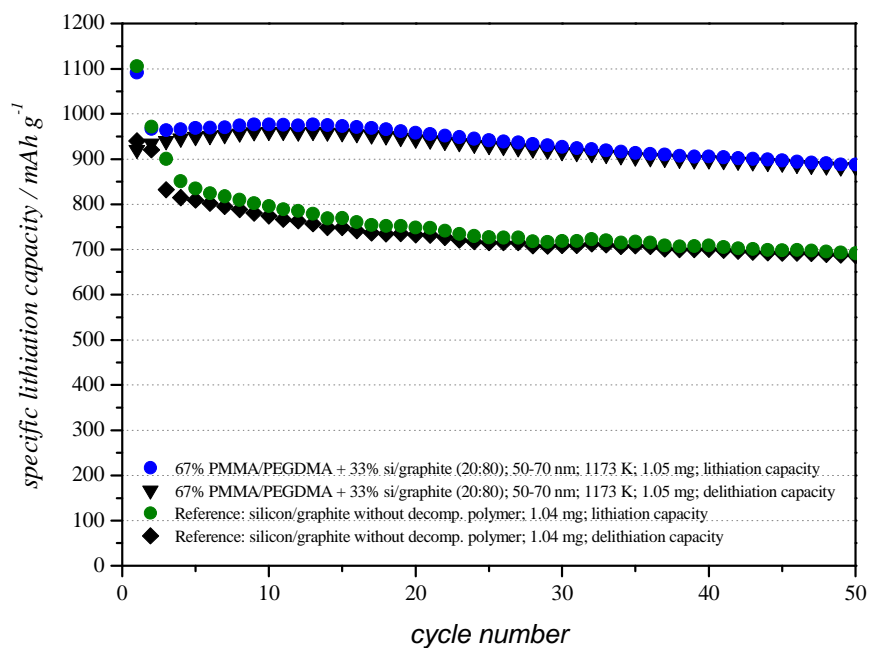


Figure 89: CCC measurement (0.5 C) of active material composed of PMMA/PEGDMA and silicon/graphite (20:80) with silicon particle size of 50-70 nm

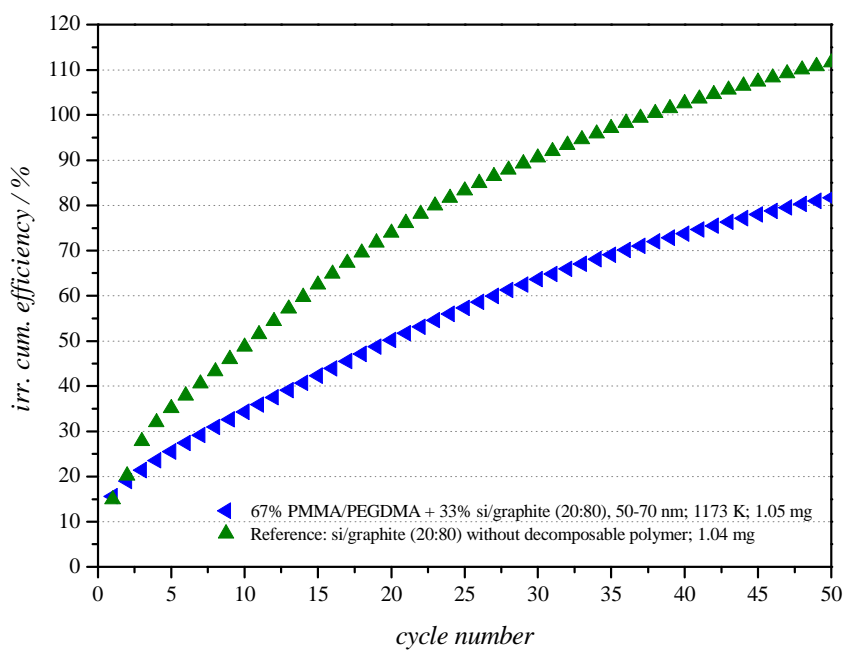


Figure 90: Irreversible cumulative efficiency of active material based on PMMA/PEGDMA and Si/graphite (20:80) with silicon particle size of 50-70 nm

The calculation of the carbon content after decomposition of this polymer/silicon/graphite mixture is easier compared to the active material in the section before. The polymerisation is carried out via bulk polymerisation and the whole mixture is transferred into the oven for decomposition. A critical factor here is the homogeneity of the material after polymerisation. Domains, containing more or less silicon and graphite are formed. Therefore, the c-rate couldn't be calculated that accurate. The mass loss after heat treatment amounts between 50% and 60%.

A capacity of  $920 \text{ mAh g}^{-1}$  could be achieved with the material after decomposition at 1173 K (figure 89). The capacity fade after 50 cycles amounts 6% for the Si/C composite with decomposed polymer and 27% for the reference material, respectively.

The lowest irreversible cumulative capacity (figure 90) exhibit the new active material. The results clearly show that an improvement in cycling stability and capacity retention could be achieved.



### 4.3.3.2. Active material with silicon/graphite ratio of 30:70 and 50-70 nm silicon particle size

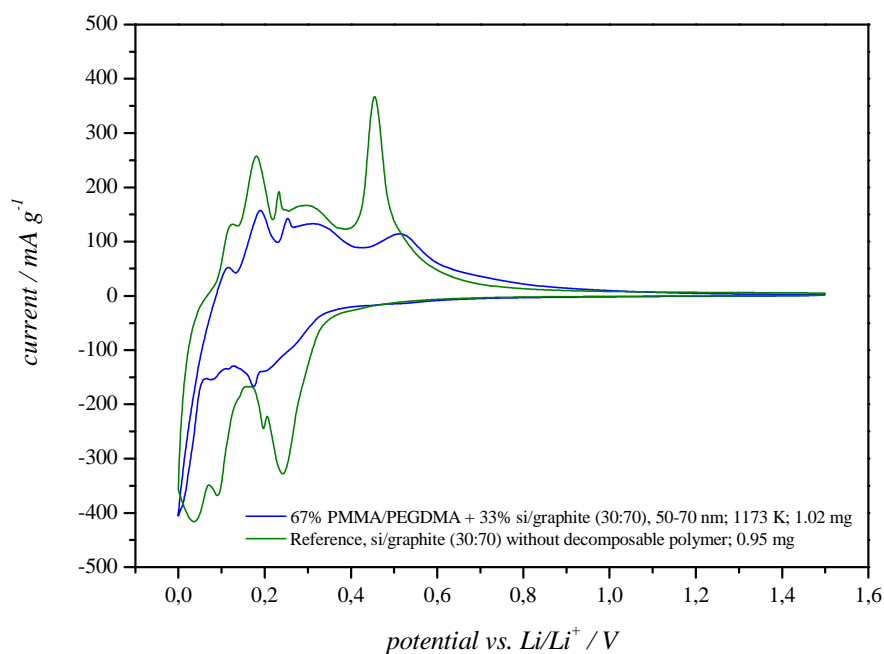


Figure 91: Second cycles of CV measurement (scan rate:  $30 \mu\text{V s}^{-1}$ ) of active material composed of PMMA/PEGDMA and silicon/graphite (30:70) with silicon particle size of 50-70 nm

Table 25: Corresponding lithiation and delithiation capacities of the second cycles of CV measurement (figure 91)

	delith. cap./mAh g <sup>-1</sup>	lith. cap./mAh g <sup>-1</sup>	rev./%	mass/mg
Si/gra 30:70, 1173 K	680.9	737.9	92.3	1.02
reference	939.0	1050.2	89.4	0.95

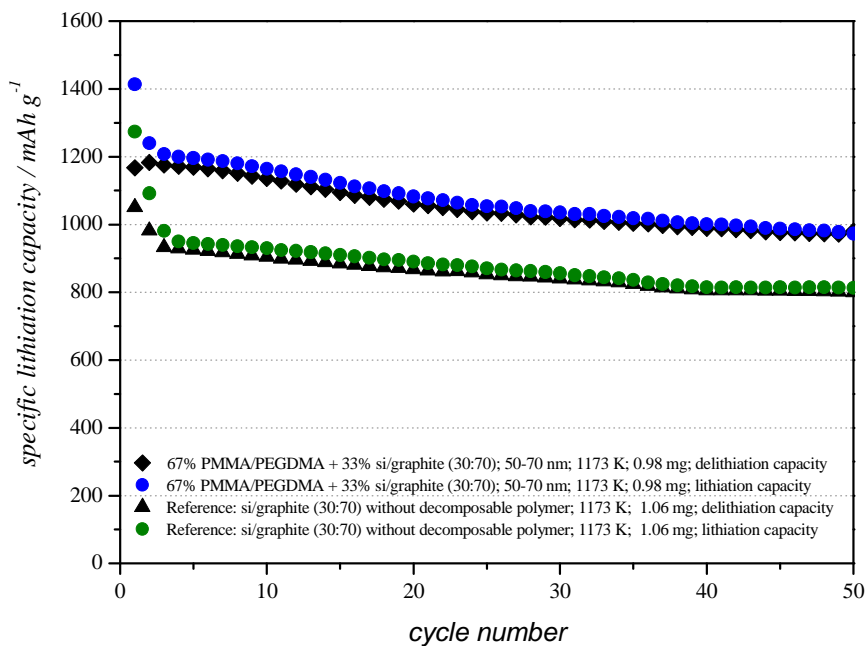


Figure 92: CCC measurement (0.5 C) of active material composed of PMMA/PEGDMA and silicon/graphite (30:70) with silicon particle size of 50-70 nm

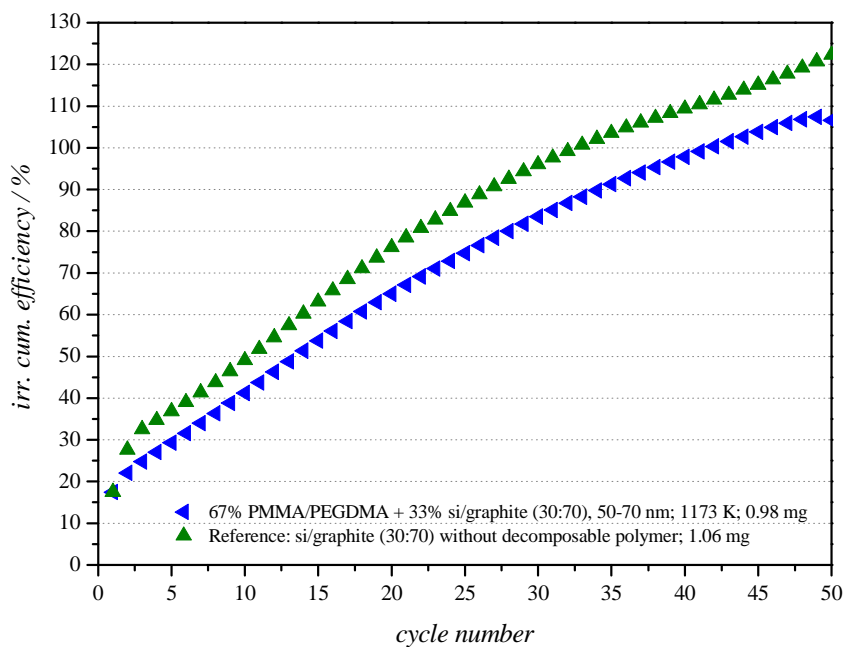


Figure 93: Irreversible cumulative efficiency of active material based on PMMA/PEGDMA and Si/graphite (30:70) with silicon particle size of 50-70 nm

The mass loss after heat treatment amounts between 50% and 60%. A delithiation capacity of about  $1170 \text{ mAh g}^{-1}$  could be achieved in the first cycle with the new active material and about  $1050 \text{ mAh g}^{-1}$  with the reference electrode (figure 92). The capacity fade after 50 cycles amounts 16% and 24%, respectively.

The lowest irreversible cumulative efficiencies (figure 93) reveals the active material with nano-silicon, embedded in a matrix of the decomposed polymer.

Again, the worst performance shows the reference material, Si/C composit without decomposable polymer.

#### 4.3.3.3. Active materials with a silicon/graphite ratio of 20:80 and silicon particle size of 30-50 nm

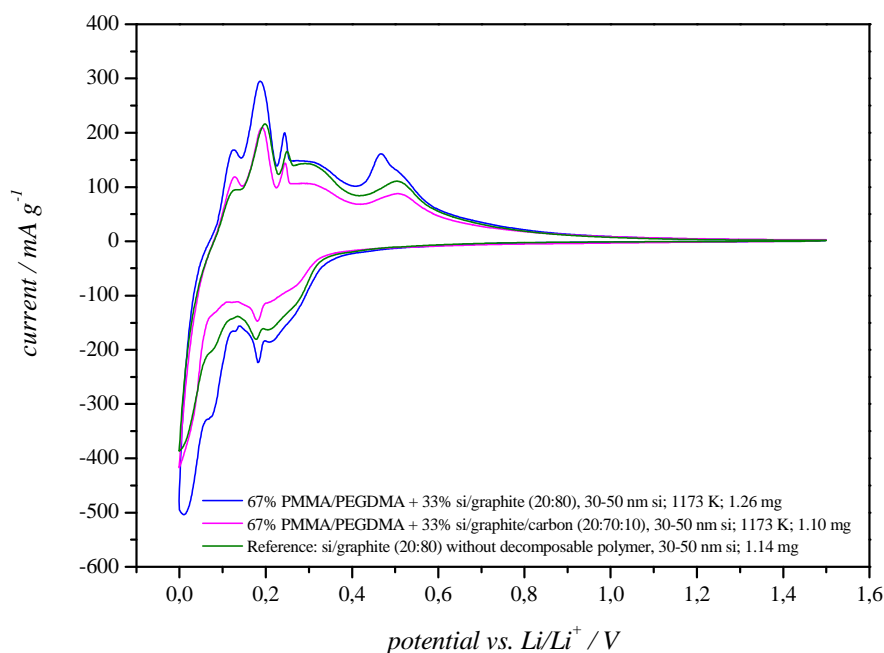


Figure 94: Second cycles of CV measurement (scan rate:  $30 \mu\text{V s}^{-1}$ ) of active materials composed of PMMA/PEGDMA and silicon/graphite (20:80) and silicon/graphite/carbon (20:70:10) respectively, silicon particle size: 30-50 nm

Table 26: Corresponding lithiation and delithiation capacities of the second cycles of CV measurement (figure 94)

	delith. cap./mAh g <sup>-1</sup>	lith. cap./mAh g <sup>-1</sup>	rev./%	mass/mg
<b>Si/gra 20:80, 1173 K</b>	781.9	732.4	93.9	1.26
<b>Si/gra/C 20:80:10, 1173 K</b>	551.7	597.0	92.4	1.10
<b>Reference</b>	632.5	673.0	94.0	1.14

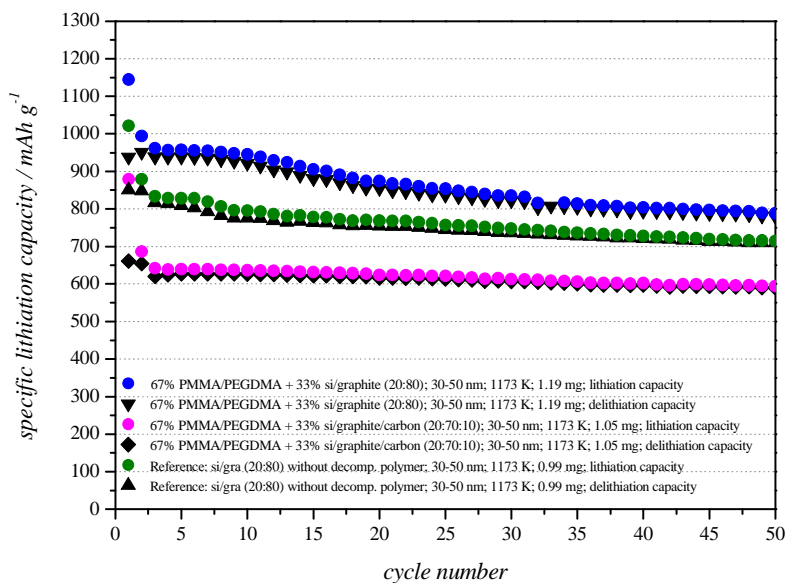


Figure 95: CCC measurement (0.5 C) of active materials composed of PMMA/PEGDMA and silicon/graphite (20:80) and silicon/graphite/carbon (20:70:10) respectively, silicon particle size: 30-50 nm

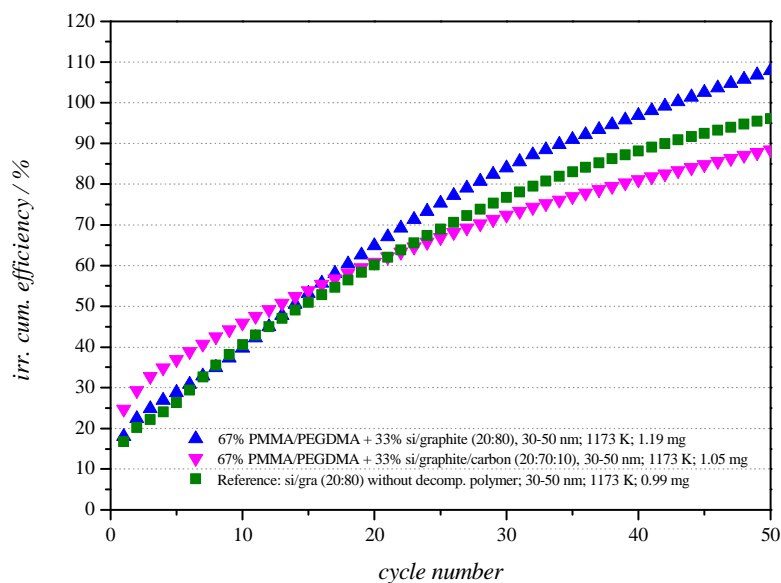


Figure 96: Irreversible cumulative efficiencies of active materials based on PMMA/PEGDMA and Si/graphite (20:80) and Si/graphite/C (20:70:10) respectively, silicon particle size: 30-50 nm

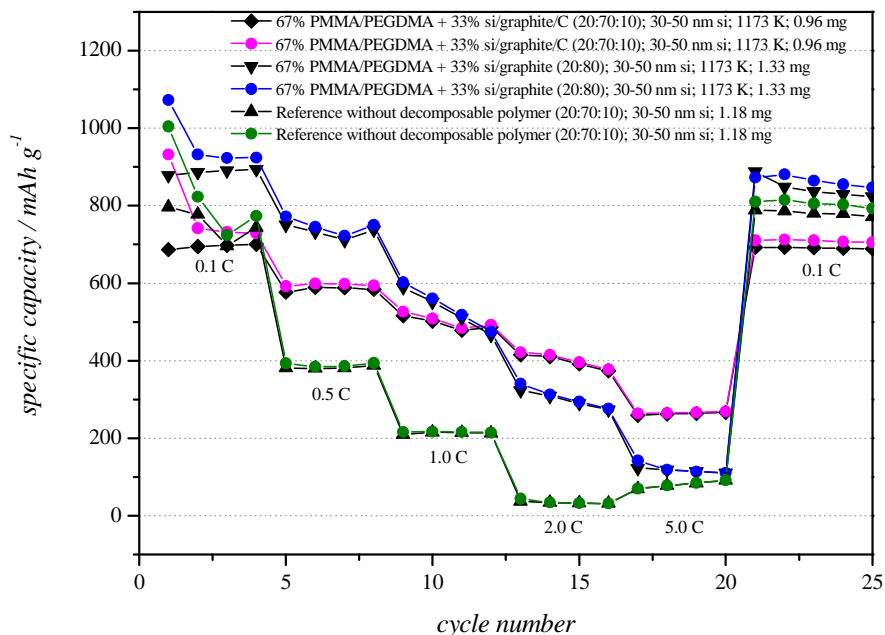


Figure 97: Rate capability test of active materials based on PMMA/PEGDMA and Si/graphite (20:80) and Si/graphite/C (20:70:10), silicon particle size: 30-50 nm

The mass loss after heat treatment for the material containing amorphous carbon amounts 60% and the mass loss of material without carbon amounts 40%.

As expected, the lowest capacities could be achieved with the carbon black containing sample. Interestingly, this Si/C composite material reveals a superior cycling stability with a capacity fade of 11% after 50 cycles (figure 95) and the lowest irreversible cumulative efficiency (figure 96). The capacity fade for the other electrodes amounts 17% for each.

Rate capability tests show (figure 97), that the capacity retention at higher c-rates could be improved by embedding silicon nano-particles into a carbonaceous matrix through decomposition of a decomposable polymer. Also, the addition of carbon black before decomposition improves the rate capability of the electrode but at the expense of capacity.

### 4.3.3.4. Active materials with a silicon/graphite ratio of 30:70 and silicon particle size of 30-50 nm

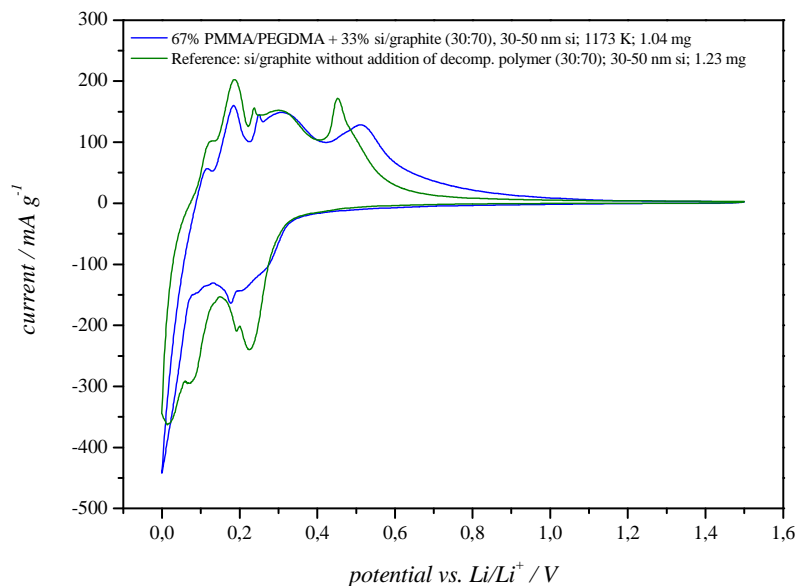


Figure 98: Second cycles of CV measurement (scan rate:  $30 \mu\text{V s}^{-1}$ ) of active materials composed of PMMA/PEGDMA and silicon/graphite (30:70) with silicon particle size of 30-50 nm

Table 27: Corresponding lithiation and delithiation capacities of the second cycles of CV measurement (figure 98)

	delith. cap./mAh g <sup>-1</sup>	lith. cap./mAh g <sup>-1</sup>	rev./%	mass/mg
Si/gra 30:70, 1173 K	778.9	825.5	94.4	1.04
reference	703.7	824.1	85.4	1.23

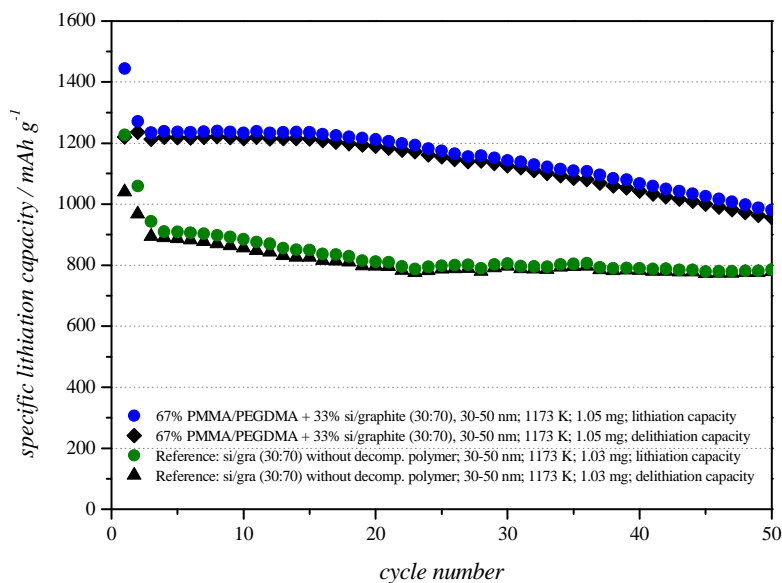


Figure 99: CCC measurement (0.5 C) of active materials composed of PMMA/PEGDMA and silicon/graphite (30:70) with silicon particle size of 30-50 nm

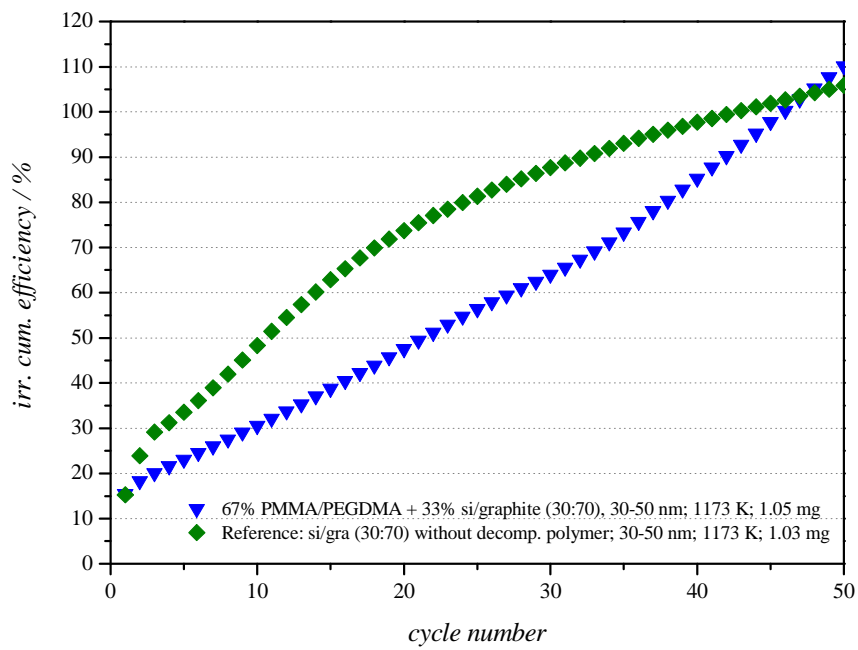


Figure 100: Irreversible cumulative efficiencies of active materials based on PMMA/PEGDMA and Si/graphite (30:70) with silicon particle size of 30-50 nm

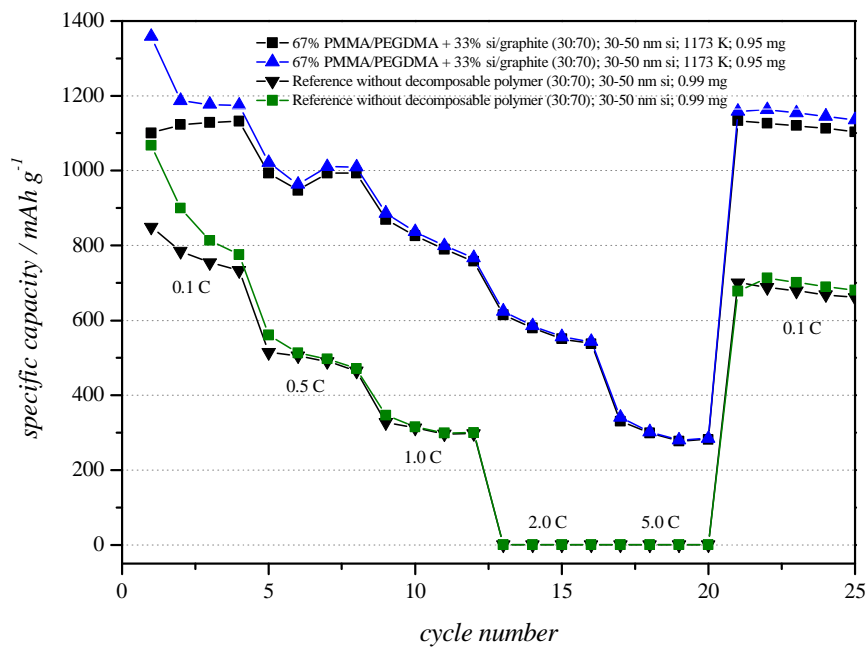


Figure 101: Rate capability test of active materials based on PMMA/PEGDMA and Si/graphite (30:70) with silicon particle size of 30-50 nm

The mass loss after heat treatment amounts about 40%. As expected, the highest capacities of 1220 mAh g<sup>-1</sup> could be achieved with the new active material after decomposition at 1173 K (figure 99). The capacity fade of this material is 22% after 50 cycles. The reference electrode could achieve a first delithiation capacity of 1040 mAh g<sup>-1</sup> and a capacity fade of 25% during 50 cycles. The rate capability of active material containing 30% nano-silicon can clearly be improved when silicon particles are embedded in a carbonaceous matrix through decomposition of polymers (figure 101). With this high silicon content the reference electrode exhibits a bad cycling stability at higher c-rates.

Comparison of the results:

In general, a tendency can be observed, that active material with silicon to graphite ratio of 20:80 and a silicon particle size of 30-50 nm shows the better electrochemical performance. A decomposition temperature of 1173 K and decomposition duration of two hours also seems to be beneficial for the electrode performance.

Nevertheless, the results clearly show that an improvement of cycling stability and rate capability could be achieved when silicon particles are embedded in a carbonaceous matrix through high temperature pyrolysis of decomposable polymers compared to conventional produced silicon/graphite composite electrodes.

Advantages of the used polymer are that it enables an easy production with cheap raw materials.



#### 4.3.4. Conclusion

In this doctoral thesis, silicon-graphite composite materials were developed, based on three different at high temperatures decomposable polymers. These active materials for the anode of LIBs consisted of graphite particles, coated with nano-silicon and embedded in a carbonaceous matrix. Such architecture serves the particular purpose to accommodate huge volume changes, silicon particles are undergoing during repeated lithiation and delithiation processes. In addition, carbon is an important dispersing agent to prevent particle-particle interactions of nano-silicon, also known as electrochemical sintering.

It was found, that pyrolysis of polydicyclopentadiene (PDCPD) and polymethyl methacrylate (PMMA) crosslinked with polyethylenglycol dimethacrylate (PEGDMA) could provide appropriate carbon matrices to prevent pulverisation of silicon during extensive cycling. However, nano-silicon encapsulated in polyHIPE structure didn't show sufficient capacities. It is believed, that inactive silicon compounds were produced during the polymerisation process.

The carbon coated silicon nanocomposite electrodes showed an improved cycle life and rate capability at higher rates compared to conventional produced Si/C composite electrodes, without implementation of decomposable polymers. It is strongly believed that the carbon layer after decomposition of the polymer is responsible for enhanced dimensional stability of the silicon particles during lithiation and delithiation processes and the improved cycle life of the electrode. Additionally, the carbon layer improves the electrical conductivity of the composite.

Nevertheless, the efforts in research and development of high capacity electrodes need to be continued to find utilisation in commercial energy storage systems.

## 5. APPENDIX

### 5.1. LIST OF CHEMICALS

chemicals	supplier	purity
Aceton	Merck	≥ 99.8 %
Aluminium wire (Ø ~ 1.5 mm)	Aldrich	99%
Aluminiumchloride	Aldrich	99.99 %
Basionics™ Al01	BASF	
Chloroform	Sigma Aldrich	≥ 99.5 %
Dichlormethane	Roth	≥ 99.0 %
Dicyclopentadiene	Aldrich	
ENPLATE Cu 872-A	Enthone Cookson Electronics	
ENPLATE Cu 872-B	Enthone Cookson Electronics	
ENPLATE Cu 872-C Improved	Enthone Cookson Electronics	
Ethylene Glycol Dimethacrylate	Sigma Aldrich	98%
Ethyl-methyl-imidazoliumchloride	Alfa Aesar	
Graphit	Nanshu graphite	high purity
Hexadecyltrimethylammoniumchloride	Aldrich	≥ 98 %
Hydrochloric acid	Merck	37%
Lithiumcobaltoxide		
Lithiumironphosphate		
Luprex® A75 Benzoyl Peroxide	Sigma Aldrich	75%
Methyl Methacrylate	Sigma Aldrich	99%
N-methyl-2-pyrrolidone	Alfa Aesar	99.5 %
Polyvinylidenfluorid		
Potassium hydroxide	Roth	≥ 85 %
Silicon nano powder, 30-50 nm	Nanostructures & Amorphous Materials Inc.	98%
Silicon nano powder, 50-70 nm	Nanostructures & Amorphous Materials Inc.	98%
Sn(II)chloride		
Sodium carboxymethylcellulose		
Sodium chloride		
Sulfuric acid	Sigma Aldrich	95-97 %
Super P™ Li		
UDIQUÉ 879 W	Enthone Cookson Electronics	
UDIQUÉ 891 Nickel concentrate	Enthone Cookson Electronics	
UDIQUÉ 892 Reducer	Enthone Cookson Electronics	
UDIQUÉ 893 Stabilizer	Enthone Cookson Electronics	

## 5.2. LIST OF DEVICES

Agilent 5975 C VLMSD mass spectrometer  
Agilent 7890 A gas chromatograph  
Agilent HP5-MS 5% phenyl methyl silox column  
Autolab PGSTAT 100 & 10 A Booster  
Biologic Potentiostat/Galvanostat VMP3 and MPG2  
Braun Labmaster sp glove box  
Frontier Laboratory PY2020iD Pyrolyzer  
Glassy carbon electrode (BAS Inc. Tokyo, 6.0 mm x 3.00 mm)  
Julabo F32 thermostat  
Knick 703 conductivity meter  
MACCOR Series 4000 battery tester  
Nabertherm RHTC 80-230/15, Controller B180 (Oven)  
Oxford Instrument INCAx-act  
Platinum electrode (BAS Inc. Tokyo, 6.00 mm x 1.6 mm)  
Tescan Vega 3 scanning electron microscope  
Varian Mercury 300 MHz NMR spectrometer

## 5.3. LIST OF ABBREVIATIONS

Al<sup>3+</sup> ..... aluminium ion  
BET ..... Brunauer, Emmet and Teller theory  
BPO ..... benzoyl peroxide  
CCC ..... constant current cycling  
CNT ..... carbon nano tubes  
CV ..... cyclic voltammetry  
DCPC ..... dicyclopentadiene  
DEC ..... diethyl carbonate  
DMC ..... dimethyl carbonate  
EC ..... ethylene carbonate  
EDX ..... energy dispersive x-ray spectroscopy  
EGA ..... evolved gas analysis

EGDMA/PEGDMA .....	ethylene glycol dimethacrylate
EV .....	electric vehicle
EMImCl.....	1-ethyl-3-methylimidazolium chloride
FTIR-ATR.....	fourier transform infrared spectroscopy - attenuated total reflectance
GC/MS .....	gas chromatography/mass spectrometry
IL .....	ionic liquid
LCO.....	lithium cobalt oxide
Li <sup>+</sup> .....	lithium ion
LIB .....	lithium ion battery
MHz.....	mega hertz
MMA/PMMA.....	methyl methacrylate
NaCMC .....	sodium carboxymethylcellulose
NHE.....	normal hydrogen electrode
NMR.....	nuclear magnetic resonance spectrometry
OCV .....	open circuit voltage
PE .....	polyester
PET.....	polyethyleneterephthalat
Pt.....	platinum
PVD.....	physical vapour deposition
PVDF.....	polyvinylidene fluoride
Py-GC/MS .....	pyrolysis gas chromatography mass spectrometry
RTIL .....	room temperature ionic liquid
SEI.....	solid electrolyte interphase
SEM.....	secondary electron microscopy
Si.....	silicon
SiC .....	silicon carbide
Si/C.....	silicon carbon composite
TG/DSC.....	thermogravimetry-differential scanning calorimetry
VC .....	vinylene carbonate
XRD .....	x-ray diffraction

## 5.4. LIST OF FIGURES

<b>Figure 1:</b> Lithium-ion battery application in dependence of the total battery capacity as function of the battery power [125] .....	1
<b>Figure 2:</b> Global lithium-ion battery market revenue forecast (redrawn from [130]) [124] .....	1
<b>Figure 3:</b> Schematic representation of a Leclanchè cell.....	4
<b>Figure 4:</b> Discharge characteristic of a battery [17] .....	7
<b>Figure 5:</b> Discharge characteristic of a LIB with different c-rates [19] .....	11
<b>Figure 6:</b> Ragone plot with current and next-generation energy storage technologies [21].....	11
<b>Figure 7:</b> Schematic representation of the bone effect in following inhomogeneous current distribution [28] .....	15
<b>Figure 8:</b> Stern model of the electric double layer [30].....	16
<b>Figure 9:</b> Some standard potentials of metal ions and water decomposition vs. NHE.....	17
<b>Figure 10:</b> Schematic representation of a lithium-ion battery .....	21
<b>Figure 11:</b> Comparison of the energy densities of different active materials for cathodes and anodes in LIBs [41] .....	23
<b>Figure 12:</b> Different types of insertion materials for the positive electrode of lithium-ion batteries [43] .....	24
<b>Figure 13:</b> Two-dimensional crystal structure of $\text{LiCoO}_2$ (a) [45], cyclic voltammogram of a $\text{LiCoO}_2$ electrode (b) and SEM image of $\text{LiCoO}_2$ powder (c).....	25
<b>Figure 14:</b> Cyclic voltammogram of a $\text{LiNi}_{1/3}\text{Mn}_{1/3}\text{Co}_{1/3}\text{O}_2$ electrode (a) and SEM image of $\text{LiNi}_{1/3}\text{Mn}_{1/3}\text{Co}_{1/3}\text{O}_2$ powder (b).....	26
<b>Figure 15:</b> Crystal structure of spinel oxide [45] (a), cyclic voltammogram of a $\text{LiMn}_2\text{O}_4$ electrode [43] (b) and SEM image of $\text{LiMn}_2\text{O}_4$ powder (c).....	26
<b>Figure 16:</b> Crystal structure of $\text{LiFePO}_4$ (a) [45], cyclic voltammogram of a $\text{LiFePO}_4$ electrode (b) and SEM image of the powder (c) .....	27
<b>Figure 17:</b> Representation of stage formation during electrochemical intercalation of lithium into graphite [43] .....	29
<b>Figure 18:</b> Schematic representation of lithium intercalation into graphene layers (redrawn from [43]) (a), cyclic voltammogram of a graphite electrode [48] (b) and SEM image of the powder (c) .....	29
<b>Figure 19:</b> Cyclic voltammogram of a $\text{Li}_4\text{Ti}_5\text{O}_{12}$ electrode (a) and SEM image of the powder (b).....	33
<b>Figure 20:</b> Forest of nanotubes grown on metal sheets (left) [55] and porous metal foam as current collector for LIBs (right) [56].....	34
<b>Figure 21:</b> Mechanism of electrochemically induced reduction of EC [63] .....	38
<b>Figure 22:</b> Schematic drawing of different films forming on an anode in organic electrolytes (SEI) (redrawn) .....	38

<b>Figure 23:</b> General equation of the mechanism of electrochemically induced polymerization of polymerisable monomer additives.....	39
<b>Figure 24:</b> Changes at the anode/electrolyte interface / aging mechanisms (redrawn from [68]).....	41
<b>Figure 25:</b> Schematic drawing of a Swagelok-T-cell (a) and a pouch bag cell (b) .....	42
<b>Figure 26:</b> Different kinds of 3 dimensional current collectors – overview.....	45
<b>Figure 27:</b> SEM images and EDX spectra of copper plated polymer non-woven (a, b) and of nickel-plated non-woven polymer (c, d).....	47
<b>Figure 28:</b> Conductivity measurement of EMImCl*1.5 AlCl <sub>3</sub> .....	48
<b>Figure 29:</b> Electrochemical stability window of EMImCl*1.5 AlCl <sub>3</sub> vs. Pt pseudo reference electrode .....	49
<b>Figure 30:</b> Current yield as function of reaction time for aluminium deposition at different reaction temperatures .....	50
<b>Figure 31:</b> Current yield as function of reaction time for aluminium plating on copper and nickel plated non-woven polymer with different current densities .....	50
<b>Figure 32:</b> Cyclic voltammograms of aluminium electrodeposition on copper plated non-woven polymer from EMImCl*1.5 AlCl <sub>3</sub> with a scan rate of 10 mV s <sup>-1</sup> at 368 K (a) and SEM image of the cross section of a plated fibre (b) .....	51
<b>Figure 33:</b> Cyclic voltammograms of aluminium electrodeposition on nickel plated non-woven polymer from EMImCl*1.5 AlCl <sub>3</sub> with a scan rate of 10 mV s <sup>-1</sup> at 368 K (a) and SEM image of the cross section of a plated fibre (b) .....	51
<b>Figure 34:</b> SEM images of deposited aluminium layers from EMImCl*1.5 AlCl <sub>3</sub> at 368 K with different current densities (10 mA cm <sup>-2</sup> (a), 20 mA cm <sup>-2</sup> (b), 30 mA cm <sup>-2</sup> (c) and 40 mA cm <sup>-2</sup> (d)).....	53
<b>Figure 35:</b> EDX spectrum of electrodeposited Al on Ni plated non-woven polymer from IL.....	53
<b>Figure 36:</b> Cyclic voltammograms of copper metal (left) and nickel metal (right) at room temperature; .....	54
<b>Figure 37:</b> SEM images of copper plated working electrode before (a) and after (b) one week at constant voltage of 4.3 V vs. Li/Li <sup>+</sup> .....	55
<b>Figure 38:</b> EDX elemental mapping of Al (a) and Cu (b) of the copper plated working electrode after one week at constant voltage of 4.3 V vs. Li/Li <sup>+</sup> .....	56
<b>Figure 39:</b> SEM images of nickel plated working electrode before (a) and after (b) one week at constant voltage of 4.3 V vs. Li/Li <sup>+</sup> .....	56
<b>Figure 40:</b> EDX elemental mapping of Ni before (a) and after (b) one week at constant voltage of 4.3 V vs. Li/Li <sup>+</sup> .....	56
<b>Figure 41:</b> Cyclic voltammogram of nickel plated non-woven polymer at room temperature; scan rate: 1 mV s <sup>-1</sup> (a) and charge as function of time (b).....	58
<b>Figure 42:</b> Cyclic voltammogram of nickel and aluminium plated non-woven polymer at room temperature; scan rate: 1 mV s <sup>-1</sup> (a) and charge as function of time (b) .....	59

<b>Figure 43:</b> Possible thermal decomposition path of 1-ethyl-3-methylimidazolium chloride [85] .....	61
<b>Figure 44:</b> Possible electrochemical decomposition mechanism of EMImCl [90] .....	62
<b>Figure 45:</b> Chromatogram of volatile decomposition products of EMImCl*1.5 AlCl <sub>3</sub> (a) and accompanied mass spectra of hydrochloric acid (b), chloromethane (c) and dichloromethane (d) .....	64
<b>Figure 46:</b> Extracted ion thermograms of chloromethane (a), hydrochloric acid (b), methylimidazole (c), ethylimidazole (d) and ethyl-methylimidazole (e) and the accompanied mass spectra (f) .....	65
<b>Figure 47:</b> Surface of current collector (a) and cross section of a LiFePO <sub>4</sub> -electrode (b) .....	68
<b>Figure 48:</b> Cyclic voltammogram ((a), scan rate: 30 μV s <sup>-1</sup> ) and constant current cycling ((b), rate: 1 C) of LFP with 3D current collector .....	69
<b>Figure 49:</b> SEM image (left) and EDX spectrum (right) of with Al PVD plated non-woven polymer	71
<b>Figure 50:</b> Cyclic voltammogram (scan rate: 30 μV s <sup>-1</sup> ) of LCO with 3D current collector .....	71
<b>Figure 51:</b> SEM images of the cross section of LCO electrodes with 3D current collector (a) compared to 2D current collector (b) .....	72
<b>Figure 52:</b> Comparison of constant current cycling (left, 1C) and rate capability test (right) of an electrode with 3D current collector (8.60 mg) and 2D current collector (8.50 mg) .....	72
<b>Figure 53:</b> SEM image of with Al PVD plated non-woven polymer .....	75
<b>Figure 54:</b> SEM image of with Al PVD plated non-woven polymer .....	75
<b>Figure 55:</b> CV measurement (scan rate: 30 μV s <sup>-1</sup> ) of LCO electrodes with two different 3D current collectors compared to aluminium foil as current collector .....	76
<b>Figure 56:</b> Rate capability tests of LCO electrodes with two different 3D current collectors compared to aluminium foil as current collector .....	76
<b>Figure 57:</b> Lithiation capacities (above) and delithiation capacities (below) received from CCC measurement (1 C) of LCO electrodes with 3D current collectors (different Al layer thicknesses) compared to aluminium foil .....	77
<b>Figure 58:</b> Irreversible cumulative efficiencies of LCO electrodes with two different 3D current collectors and aluminium foil for comparison .....	77
<b>Figure 59:</b> Lithiation- and delithiation capacities received from CCC measurement (0.5 C) of full cells with 3D current collectors. Graphite and LCO were used as active materials .....	79
<b>Figure 60:</b> Voltage profiles of lithiation and delithiation received from constant current cycling of full cells with electrodes composed of 3D current collectors. Graphite and LCO were used as active materials .....	79
<b>Figure 61:</b> Lithiation- and delithiation capacities received from CCC measurement (0.1 C) of full cells, where LCO coated on the 2 <sup>nd</sup> generation 3D current collector was used as cathode and graphite, coated on copper foil as anode .....	80
<b>Figure 62:</b> Voltage profiles of lithiation and delithiation received from constant current cycling of full cells, where LCO coated on the 2 <sup>nd</sup> generation 3D current collector was used as cathode and graphite, coated on copper foil as anode .....	81

<b>Figure 63:</b> Reaction equation of polymerisation of DCPD via ROMP [105] .....	83
<b>Figure 64:</b> Structures of polymethyl methacrylate (left) [129] and polyethyleneglycol dimethacrylate [108] .....	84
<b>Figure 65:</b> TG/DSC-MS curve for thermal decomposition of polyHIPE (provided by Sebastijan Kovacic) .....	84
<b>Figure 66:</b> SEM image of the active material (polyHIPE with silicon) .....	85
<b>Figure 67:</b> CV measurement (second cycles; scan rate: $10 \mu\text{V s}^{-1}$ ) of electrodes with three different graphite contributions .....	86
<b>Figure 68:</b> Comparison of CCC of active material with different graphite/silicon ratios; c-rate: 0.5 C .....	86
<b>Figure 69:</b> Predicted structural units produced during polymerisation of DCPD with $\text{AlCl}_3$ in $\text{CH}_2\text{Cl}_2$ .....	87
<b>Figure 70:</b> FTIR-ATR spectra of DCPD and PDCPD prepared in $\text{CH}_2\text{Cl}_2$ .....	88
<b>Figure 71:</b> TG/DSC-MS curve for thermal decomposition of PDCPD.....	89
<b>Figure 72:</b> EDX spectra of the active material before (a) and after (b) pyrolysis and SEM image of the active material after pyrolysis (c).....	89
<b>Figure 73:</b> XRD spectra of Si/C composite with PDCPD as decomposable polymer after pyrolysis at 1173 K; full spectrum (a) and detailed view (b).....	90
<b>Figure 74:</b> CV measurement (scan rate: $30 \mu\text{V s}^{-1}$ ) of active material composed of PDCPD and silicon/graphite (20:80) with silicon particle size of 50-70 nm.....	91
<b>Figure 75:</b> CCC measurement (0.5 C) of active material composed of PDCPD and silicon/graphite (20:80) with silicon particle size of 50-70 nm.....	92
<b>Figure 76:</b> Irreversible cumulative efficiency of active material based on DCPD and Si/graphite (20:80) with silicon particle size of 50-70 nm.....	92
<b>Figure 77:</b> Second cycles of CV measurement (scan rate: $30 \mu\text{V s}^{-1}$ ) of active materials composed of PDCPD and silicon/graphite (20:80) with silicon particle size of 30-50 nm, pyrolysed at 1173 K.....	94
<b>Figure 78:</b> CCC measurement (0.5 C) of active materials composed of PDCPD and silicon/graphite (20:80) with silicon particle size of 30-50 nm, pyrolysed at 1173 K.....	95
<b>Figure 79:</b> Irreversible cumulative efficiencies of active materials based on DCPD and Si/graphite (20:80) with silicon particle size of 30-50 nm.....	95
<b>Figure 80:</b> Rate capability test of active materials based on DCPD and Si/graphite (20:80) with silicon particle size of 30-50 nm .....	96
<b>Figure 81:</b> Second cycles of CV measurement (scan rate: $30 \mu\text{V s}^{-1}$ ) of active materials composed of PDCPD and silicon/graphite (30:70) with silicon particle size of 30-50 nm, pyrolysed at 1173 K.....	97
<b>Figure 82:</b> CCC measurement (0.5 C) of active materials composed of PDCPD and silicon/graphite (30:70) and silicon/graphite/C (30:60:10) with silicon particle size of 30-50 nm, pyrolysed at 1173 K .....	97



<b>Figure 83:</b> Irreversible cumulative efficiencies of active materials based on DCPD and Si/graphite (30:70) and Si/graphite/C (30:60:10) with silicon particle size of 30-50 nm, pyrolysed at 1173 K .....	98
<b>Figure 84:</b> FTIR-ATR spectrum of 50 mol% MMA and 50 mol% EGDMA prepared via in-situ bulk polymerisation .....	100
<b>Figure 85:</b> TG/DSC-MS curve for thermal decomposition of PMMA/PEGDMA .....	101
<b>Figure 86:</b> SEM image and EDX spectrum of the active material after pyrolysis .....	102
<b>Figure 87:</b> XRD spectrum of Si/C composite with PMMA/PEGDMA as decomposable polymer after pyrolysis at 1173 K and a composition of 80% graphite and 20% nano-silicon (50-70 nm) .....	102
<b>Figure 88:</b> Second cycles of CV measurement (scan rate: $30 \mu\text{V s}^{-1}$ ) of active material composed of PMMA/PEGDMA and silicon/graphite (20:80) with silicon particle size of 50-70 nm .....	103
<b>Figure 89:</b> CCC measurement (0.5 C) of active material composed of PMMA/PEGDMA and silicon/graphite (20:80) with silicon particle size of 50-70 nm .....	104
<b>Figure 90:</b> Irreversible cumulative efficiency of active material based on PMMA/PEGDMA and Si/graphite (20:80) with silicon particle size of 50-70 nm .....	104
<b>Figure 91:</b> Second cycles of CV measurement (scan rate: $30 \mu\text{V s}^{-1}$ ) of active material composed of PMMA/PEGDMA and silicon/graphite (30:70) with silicon particle size of 50-70 nm .....	106
<b>Figure 92:</b> CCC measurement (0.5 C) of active material composed of PMMA/PEGDMA and silicon/graphite (30:70) with silicon particle size of 50-70 nm .....	107
<b>Figure 93:</b> Irreversible cumulative efficiency of active material based on PMMA/PEGDMA and Si/graphite (30:70) with silicon particle size of 50-70 nm .....	107
<b>Figure 94:</b> Second cycles of CV measurement (scan rate: $30 \mu\text{V s}^{-1}$ ) of active materials composed of PMMA/PEGDMA and silicon/graphite (20:80) and silicon/graphite/carbon (20:70:10) respectively, silicon particle size: 30-50 nm .....	108
<b>Figure 95:</b> CCC measurement (0.5 C) of active materials composed of PMMA/PEGDMA and silicon/graphite (20:80) and silicon/graphite/carbon (20:70:10) respectively, silicon particle size: 30-50 nm .....	109
<b>Figure 96:</b> Irreversible cumulative efficiencies of active materials based on PMMA/PEGDMA and Si/graphite (20:80) and Si/graphite/C (20:70:10) respectively, silicon particle size: 30-50 nm .....	109
<b>Figure 97:</b> Rate capability test of active materials based on PMMA/PEGDMA and Si/graphite/C (20:70:10), silicon particle size: 30-50 nm .....	110
<b>Figure 98:</b> Second cycles of CV measurement (scan rate: $30 \mu\text{V s}^{-1}$ ) of active materials composed of PMMA/PEGDMA and silicon/graphite (30:70) with silicon particle size of 30-50 nm .....	111
<b>Figure 99:</b> CCC measurement (0.5 C) of active materials composed of PMMA/PEGDMA and silicon/graphite (30:70) with silicon particle size of 30-50 nm .....	111
<b>Figure 100:</b> Irreversible cumulative efficiencies of active materials based on PMMA/PEGDMA and Si/graphite (30:70) with silicon particle size of 30-50 nm .....	112

<b>Figure 101:</b> Rate capability test of active materials based on PMMA/PEGDMA and Si/graphite (30:70) with silicon particle size of 30-50 nm.....	112
--	-----

## 5.5. LIST OF TABLES

<b>Table 1:</b> Standard potential of some metals against NHE (V) [14].....	6
<b>Table 2:</b> Advantages and disadvantages of LIBs compared to other rechargeable battery systems [36] .....	19
<b>Table 3:</b> Characterisation of the main three types of EVs in terms of performance and battery properties [4] [37].....	20
<b>Table 4:</b> Overview over possible active materials for the positive electrode [43] .....	24
<b>Table 5:</b> Properties of different lithiated silicon phases [49] [53] .....	31
<b>Table 6:</b> Organic electrolyte solvents for LIBs and their properties [57].....	36
<b>Table 7:</b> Common lithium salts for electrolytes in LIBs and some of their properties [57].....	36
<b>Table 8:</b> Steps of electroless metal deposition process with related temperature and time for each step .....	46
<b>Table 9:</b> Average values of the charge flow of different 3D current collectors during chronoamperometric measurement (for 240 hours) .....	60
<b>Table 10:</b> <sup>1</sup> H NMR data (300 MHz, D <sub>2</sub> O) for EMImCl*1.5 AlCl <sub>3</sub> and EMImCl (300 MHz, CDCl <sub>3</sub> ) before and after electrochemical and/or thermal treatment [93] [94].....	63
<b>Table 11:</b> Comparison of mass and conductivity of various current collectors.....	67
<b>Table 12:</b> Electrode slurry composition.....	68
<b>Table 13:</b> Corresponding lithiation and delithiation capacities of CV measurement (fig. 48 above) ..	69
<b>Table 14:</b> Electrode slurry composition.....	71
<b>Table 15:</b> Corresponding lithiation and delithiation capacities of CV measurement (fig. 50).....	72
<b>Table 16:</b> Capacities of electrodes with different current collectors at different c-rates from rate capability test (fig.56) and corresponding capacity losses compared to the first cycles .....	76
<b>Table 17:</b> Electrode slurry composition.....	85
<b>Table 18:</b> Comparison of the theoretical and practical capacity of active material with different graphite contributions .....	86
<b>Table 19:</b> Different active materials with DCPD as decomposable polymer, prepared for electrochemical characterisation .....	91
<b>Table 20:</b> Corresponding lithiation and delithiation capacities of the second cycle of CV measurement (figure 74).....	91

<b>Table 21:</b> Corresponding lithiation and delithiation capacities of the second cycle of CV measurement (figure 77).....	94
<b>Table 22:</b> Corresponding lithiation and delithiation capacities of the second cycles of CV measurement (figure 81) .....	97
<b>Table 23:</b> Different active materials prepared with MMA/EGDMA as decomposable polymer .....	103
<b>Table 24:</b> Corresponding lithiation and delithiation capacities of the second cycles of CV measurement (figure 88) .....	103
<b>Table 25:</b> Corresponding lithiation and delithiation capacities of the second cycles of CV measurement (figure 91) .....	106
<b>Table 26:</b> Corresponding lithiation and delithiation capacities of the second cycles of CV measurement (figure 94) .....	109
<b>Table 27:</b> Corresponding lithiation and delithiation capacities of the second cycles of CV measurement (figure 98) .....	111

## 5.6. LITERATURE

- [1]. **Jean-Marie Tarascon, Michelle Armand.** Issues and challenges facing rechargeable lithium batteries. *Nature*. November 2001, 414, S. 359-367.
- [2]. **Seung-Taek Myung, Yashiro Hitoshi, Yang-Kook Sun.** Electrochemical behaviour and passivation of current collectors in lithium-ion batteries. *Journal of Materials Chemistry*. 2011, 21, S. 9891-991.
- [3]. **Bruno G. Pollet, Iain Staffell, Jin Lei Shang.** Current status of hybrid, battery and fuel cell electric vehicles: From electrochemistry to market prospects. *Electrochimica Acta*. 2012, 84, S. 235-249.
- [4]. **X. Chen, W. Shen, T. Tu Vo, Z. Cao, A. Kapoor.** An overview of lithium-ion batteries for electric vehicles. *IPEC 2012*. 2012, S. 230-235.
- [5]. **John S. Wang, Ping Liu, Elena Sherman, Mark Verbrugge, Harshad Tataria.** Formulation and characterization of ultra-thick electrodes for high energy lithium-ion batteries employing tailored metal foams. *Journal of Power Sources*. 2011, 196, S. 8714-8718.
- [6]. **Liangbing Hu, Fabio La Mantia, Hui Wu, Xing Xie, James McDonough, Mauro Pasta, Yi Cui.** Lithium-Ion Textile Batteries with Large Areal Mass Loading. *Advanced Energy Materials*. 2011, 1, S. 1012-1017.
- [7]. **Emilie Perre, Leif Nyholm, Torbjörn Gustafsson, Pierre-Louis Taberna, Patrice Simon, Kristina Edström.** Direct electrodeposition of aluminium nano-rods. *Electrochemistry Communications*. 2008, 10, S. 1467-1470.
- [8]. **Wang QM, Wand DL, Wang B.** Preparation and Electrochemical Performance of LiFePO<sub>4</sub>-based Electrode Using Three-Dimensional Porous Current Collector. *International Journal of Electrochemical Science*. 2012, 7, S. 8753-8760.
- [9]. **Qina Sa, Yan Wang.** Ni foam as the current collector for high capacity Si-C composite electrode. *Journal of Power Sources*. 2012, 208, S. 46-51.
- [10]. **Chiwon Kang, Indranil Lahiri, Rangasamy Baskaran, Won-Gi Kim, Yang-Kook Sun, Wonbong Choi.** 3-dimensional carbon nanotube for lithium-ion battery anode. *Journal of Power Sources*. 2012, 219, S. 364-370.
- [11]. **R.M. Dell, D.A.J. Rand.** *Understanding Batteries*. Cambridge UK : The Royal Society of Chemistry, 2001. 0-85404-605-4.
- [12]. **Madalina Ciobanu, Jeremy P. Wilburn, Morgan L. Krim, David E. Cliffel.** Fundamentals. [Buchverf.] Cynthia G. Zosky. *Handbook of Electrochemistry*. Oxford, UK : Elsevier, 2007 .
- [13]. **David Linden, Thomas B. Reddy.** Chapter 1: Basic concepts. [Buchverf.] Thomas B. Reddy. *Linden's Handbook of Batteries*. USA : Mc Graw Hill, 2011.
- [14]. utexas. [Online] 2013. [Zitat vom: 24. Juni 2013.] <http://ch302.cm.utexas.edu/echem/echem-cells/selector.php?name=std-red-potentials>.

- [15]. **Salomon, Mark.** Electrochemical principles and reactions. [Buchverf.] Thomas B. Reddy. *Linden's Handbook of Batteries*. USA : Mc Graw Hill, 2011.
- [16]. **G. Hambitzer, K. Pinkwart, C. Ripp, C. Schiller.** Fundamentals and General Aspects of Electrochemical Power Sources. [Buchverf.] Jürgen O. Besenhard. *Handbook of Battery Materials*. Germany : WILEY-VCH, 1999.
- [17]. **M. Winter, R.J. Brodd.** What are batteries, fuel cells and supercapacitors? *Chemical Reviews*. 2004, 104, S. 4245-4269.
- [18]. **W. Menz, J. Mohr, O. Paul.** *Microsystem Technology*. Weinheim, Germany : WILEY-VCH, 2001. 3-527-29634-4.
- [19]. **Baldwin, Richard S.** NASA. [Online] 31.. October 2008. [Zitat vom: 03.. July 2013.] [http://www.google.de/imgres?start=83&biw=1680&bih=896&tbm=isch&tbnid=ZdMoADPLh-X4\\_M:&imgrefurl=http://www.grc.nasa.gov/WWW/RT/2007/PS-Prop/10-RPC-baldwin.html&docid=3z3llrgzzPhi1M&imgurl=http://www.grc.nasa.gov/WWW/RT/2007/images/10-RPC-baldwin.jpg&w=400&](http://www.google.de/imgres?start=83&biw=1680&bih=896&tbm=isch&tbnid=ZdMoADPLh-X4_M:&imgrefurl=http://www.grc.nasa.gov/WWW/RT/2007/PS-Prop/10-RPC-baldwin.html&docid=3z3llrgzzPhi1M&imgurl=http://www.grc.nasa.gov/WWW/RT/2007/images/10-RPC-baldwin.jpg&w=400&).
- [20]. **Husein, Iqbal.** *Electric and Hybrid Vehicles - Design Fundamentals*. USA : CRC Press Taylor & Francis Group, 2011. 978-1-4398-1178-8.
- [21]. SAE International. [Online] 2013. [Zitat vom: 02.. Juli 2013.] [http://www.sae.org/dlymagazineimages/12010\\_16223\\_ART.png](http://www.sae.org/dlymagazineimages/12010_16223_ART.png).
- [22]. **Jopp, K.** Aluminimabscheidung mit ionischen Flüssigkeiten. *Galvanotechnik*. 2009, 10, S. 22238-2241.
- [23]. **Zhao Yuguang, VanderNoot T.J.** Electrodeposition of aluminium from nonaqueous organic electrolytic systems an room temperature molten salts. *Electrochimica Acta*. 1997, 42, S. 3-13.
- [24]. **Yuliy D. Gamburg, Giovanni Zangari.** *Theory and Practice of Metal Electrodeposition*. London : Springer, 2011. 978-1-4419-9669-5.
- [25]. **Frederick W. Schneble, John F. McCormack, Rudolph J. Zeblicky.** *Electroless Metal Deposition*. 3,635,758 USA, 18.. January 1972.
- [26]. **Mallory, Glenn O.** The Fundamental Aspects of Electroless Nickel Plating. [Buchverf.] Juan B. Hajdu Glenn O. Mallory. *Electroless Plating, Fundamentals & Applications*. USA : American Electroplaters and Surface Finishers Society, Inc., 1990.
- [27]. **Atkins, P.W.** *Physikalische Chemie*. Weinheim : WILEY-VCH, 2001. 3-527-30236-0.
- [28]. **Kanani, Nasser.** *Electroplating*. Oxford : Elsevier, 2004. 18561 74514.
- [29]. **Hans-Jürgen Butt, Karlheinz Graf, Michael Kappl.** *Physics and Chemistry of Interfaces*. Weinheim : WILEY-VCH, 2003. 3-527-40413-9.
- [30]. **Rieger, Philip H.** *Electrochemistry*. New York : Chapman & Hall, Inc., 1994. 0-412-04391-2.

- [31]. **W. Simka, D. Puszczuk, G. Nawrat.** Electrodeposition of metals from non-aqueous solutions. *Electrochimica Acta*. 2009, 54, S. 5307-5319.
- [32]. **Conway, M.C. Lefebvre. B.E.** Elementary steps and mechanism of electrodeposition of Al from complex hydride ions in tetrahydrofuran baths. *Journal of Electroanalytical Chemistry*. 2000, 480, S. 34-45.
- [33]. **K. Ziegler, H. Lehmkuhl.** Herstellung von Aluminiumalkylen und Dialuminiumhydriden. *Angewandte Chemie*. 1955, 67, S. 424.
- [34]. **Welton, Thomas.** Room-Temperature Ionic Liquids. Solvents for Synthesis and Catalysis. *Chemical Reviews*. 1999, 99, S. 2071-2083.
- [35]. **S.Z. El Abedin, E.M. Moustafa, R. Hempelmann, H. Natter, F. Endres.** Additive free electrodeposition of nanocrystalline aluminium in a water and air stable ionic liquid. *Electrochemistry Communications*. 2005, 7, S. 1111-1116.
- [36]. **Zhengming (John) Zhang, Premanand Ramadass.** Lithium-Ion Battery Systems and Technology. [Buchverf.] Robert A. Meyers. *Encyclopedia of Sustainability Science*. New York : Springer Science + Business Media, 2013.
- [37]. **Vinodkumar Etacheri, Rotem Marom, Ran Elazari, Gregory Salitra, Doron Aurbach.** Challenges in the development of advanced Li-ion batteries: a review. *Energy & Environmental Science*. 2011, 4, S. 3243-3262.
- [38]. **Michael M. Thackeray, Christopher Wolverton, Eric D. Isaacs.** Electrical energy storage for transportation - approaching the limits of, and going beyond, lithium-ion batteries. *Energy & Environmental Science*. 2012, 5, S. 7854-7863.
- [39]. **Goodenough, J.** General Concepts . [Buchverf.] O. Yamamoto M. Wakihara. *Lithium Ion Batteries*. Tokio : WILEY-VCH, 1998.
- [40]. **Gholam-Abbas Nazri, Gianfranco Pistoia.** *Lithium Batteries, Science and Technology*. Massachusetts : KAP, 2004. 1-4020-7628-2.
- [41]. **Koller, Stefan.** Lithium Batteries / Batteries and Super Capacitor. Graz : s.n.
- [42]. **Masaki Yoshio, Hideyuki Noguchi.** A Review of Positive Electrode Materials for Lithium-Ion Batteries. [Buchverf.] Ralph J. Brodd, Akiya Kozawa Masaki Yoshio. *Lithium-Ion Batteries*. New York : Springer Science + Business Media, 2009.
- [43]. **Martin Winter, Jürgen O. Besenhard, Michael E. Spahr, Petr Novák.** Insertion Electrode Materials for Rechargeable Lithium Batteries. *Adv. Mater.* 1998, 10, S. 725-763.
- [44]. **Whittingham, M. Stanley.** Lithium Batteries and Cathode Materials. *Chem. Rev.* 2004, 104, S. 4271-4301.
- [45]. **Ying Shirley Meng, M. Elena Arroyo-de Dompablo.** First principle computational materials for energy storage materials in lithium-ion batteries. *Energy Environ. Sci.* 2009, 2, S. 589-609.

- [46]. **L.F. Nazar, O. Crosnier.** Anodes and composite anodes: An overview. [Buchverf.] Gianfranco Pistoia Gholam-Abba Nazri. *Lithium Batteries, Science and Technology*. USA : KAP, 2004.
- [47]. **D. Aurbach, B. Markovsky, I. Weissman, E. Levi, Y. Ein-Eli.** On the correlation between surface chemistry and performance of graphite negative electrodes for Li ion batteries. *Electrochimica Acta*. 1999, 45, S. 67-86.
- [48]. **Kren, H.** About the Continuous Growth of the Solid Electrolyte Interphase in Lithium Ion Batteries. *Doctoral Thesis*. Graz : s.n., 2011.
- [49]. **U. Kasavajjula, C. Wang, A.J. Appleby.** Nano- and bulk-silicon-based insertion anodes for lithium-ion secondary cells. *Journal of Power Sources*. 2007, 163, S. 1003-1039.
- [50]. **Zhang, W.-J.** A review of the electrochemical performance of alloy anodes for lithium-ion batteries. *Journal of Power Sources*. 2011, 196, S. 13-24.
- [51]. **M.N. Obrovac, L. Christensen, D. Ba Le, J.R. Dahn.** Alloy design for lithium-ion battery anodes. *Journal of The Electrochemical Society*. 2007, 154, S. A849-A855.
- [52]. **M.N. Obrovac, L.J. Krause.** Reversible cycling of crystalline silicon powder. *Journal of The Electrochemical Society*. 2007, 154, S. A103-A108.
- [53]. **C.J. Wen, R.A. Huggins.** Chemical Diffusion in Intermediate Phases in the Lithium-Silicon System. *Journal of Solid State Chemistry*. 1981, 37, S. 271-278.
- [54]. **H.-C. Shin, J. Dong, M. Liu.** Nanoporous structures prepared by an electrochemical deposition process. *Advanced Materials*. 2003, 15, S. 1610-1614.
- [55]. **Stewart, Mark.** NPL. [Online] 12. March 2013. [Zitat vom: 12. August 2013.] <http://www.npl.co.uk/science-technology/functional-materials/research/vibrational-energy-harvesting>.
- [56]. **Kim, Ji Young.** Metalfoam.net. [Online] 08. October 2012. [Zitat vom: 12. August 2013.] <http://www.metalfoam.net/>.
- [57]. **Xu, K.** Nonaqueous liquid electrolytes for lithium-based rechargeable batteries. *Chemical Reviews*. 2004, 104, S. 4303-4417.
- [58]. **R. Fong, U. von Sacken, J.R. Dahn.** Studies of lithium intercalation into carbons using nonaqueous electrochemical cells. *Journal of The Electrochemical Society*. 1990, 137, S. 2009-2013.
- [59]. **D. Aurbach, B. Markovsky, A. Shechter, Y. Ein-Eli.** A comparative study of synthetic graphite and Li electrodes in electrolyte solutions based on ethylene carbonate-dimethyl carbonate mixtures. *Journal of The Electrochemical Society*. 1996, 143, S. 3809-3820.
- [60]. **Peled, E.** The electrochemical behavior of alkali and alkaline earth metals in nonaqueous battery systems - the solid electrolyte interphase model. *Journal of The Electrochemical Society*. 1979, 126, S. 2047-2051.
- [61]. **S.H. Kang, D.P. Abraham, A. Xiao, B.L. Lucht.** Investigating the solid electrolyte interphase using binder-free graphite electrodes. *Journal of Power Sources*. 2008, 175, S. 526-532.

- [62]. **S. Bhattacharya, A.T. Alpas.** Micromechanisms of solid electrolyte interphase formation on electrochemically cycled graphite electrodes in lithium-ion cells. *Carbon* 50. 2012, S. 5359-5371.
- [63]. **Zhang, S.S.** A review on electrolyte additives for lithium-ion batteries. *Journal of Power Sources*. 2006, 162, S. 1379-1394.
- [64]. **S.S. Zhang, K. Xu, T.R. Jow.** EIS study on the formation of solid electrolyte interface in Li-ion batteries. *Electrochimica Acta*. 2006, 51, S. 1636-1640.
- [65]. **P. Verma, P. Maire, P. Novàk.** A review of the features and analyses of the solid electrolyte interphase using binder-free graphite electrodes. *Electrochimica Acta*. 2010, 55, S. 6332-6341.
- [66]. **M. Broussely, S. Herreyre, P. Biensan, P. Kasztejna, K. Nechev, R.J. Staniewicz.** Aging mechanisms in li ion cells and calendar life predictions. *Journal of Power Sources*. 201, 97, S. 13-21.
- [67]. **V. Agubra, J. Fergus.** Lithium ion battery anode aging mechanisms. *Materials*. 2013, 6, S. 1310-1325.
- [68]. **J. Vetter, P. Novàk, M.R. Wagner, C. Veit, K.-C. Möller, J.O. Besenhard, M. Winter, M. Wohlfahrt-Mehrens, C. Vogler, A. Hammouche.** Ageing mechanisms in lithium-ion batteries. *Journal of Power Sources*. 2005, 147, S. 269-281.
- [69]. **I. Bloom, B.W. Cole, J.J. Sohn, S.A. Jones, E.G. Polzin, V.S. Battaglia, G.L. Henriksen, C. Motloch, R. Richardson, T. Unkelhaeuser, D. Ingersoll, H.L. Case.** An accerlerated calendar and cycle life study of li-ion cells. *Journal of Power Sources*. 2001, 101, S. 238-247.
- [70]. **L.L. Shreir, R.A. Jarman, G.T. Burstein.** *Corrosion*. UK : Butterworth-Heinemann, 1994.
- [71]. **P.C. Hidber, W. Helbig, E. Kim, G.M. Whitesides.** Microcontact printing of palladium colloids: micron-scale patterning by electroless deposition of copper. *Langmuir*. 1996, 12, S. 1375-1380.
- [72]. **Schlesinger, M.** *Modern Electroplating*. New Jersey : WILEY, 2010. 978-0-470-16778-6.
- [73]. **Davis, Joseph R.** *Copper and copper alloys*. USA : ASM International, 2001. 0-87170-726-8.
- [74]. **J.R. Davis.** *Nickel, cobalt and their alloys*. USA : ASM International, 2000. 0-87170-685-7.
- [75]. **BASF.** *Electrolyte and surface-active additives for the galvanic deposition of smooth, dense aluminum layers from ionic liquids*. WO/2010/106072 Ludwigshafen/Germany, 23.. Spetember 2010.
- [76]. **Mojtaba Shamsipur, Ali Akbar Miran Beigi, Mohammed Teymouri, Sayed Mahdi Pourmortazavi, Mohsen Irandoust.** Physical and electrochemical properties of ionic liquid 1-ethyl-3-methylimidazoliumtetrafluoroborate, 1-butyl-3-methylimidazolium trifluoromethanesulfonate and 1-butyl-1-methylpyrrolidinium bis(trifluoromethylsulfonyl)imide. *Journal of Molecular Liquids*. 2010, Bd. 157, S. 43-50.
- [77]. **A. Lewandowski, L. Waligora, M. Galinski.** Ferrocene as a reference redox couple for aprotic ionic liquids. *Electroanalysis*. 2009, 21, S. 2221-2227.



- [78]. **C. Wessells, R. Ruffo, R.A. Huggins, Y. Cui.** Investigations of the electrochemical stability of aqueous electrolytes for lithium battery applications. *Electrochemical and Solid-State Letters*. 2010, 13, S. A59-A61.
- [79]. **S.Z. El Abedin, P. Giridhar, P. Schwab, F. Endres.** Electrodeposition of nanocrystalline aluminium from a chloroaluminate ionic liquid. *Electrochemistry Communications*. 2010, 12, S. 1084-1086.
- [80]. **S. Zein El Abedin, F. Endres.** Ionic liquids: The link to high-temperature molten salts? *Acc. Chem. Res.* 2007, 40, S. 1106-1113.
- [81]. **L.H.S. Gasparotto, A. Prowald, N. Borisenko, S.Z. El Abedin, A. Garsuch, F. Endres.** Electrochemical synthesis of macroporous aluminium films and their behavior towards lithium deposition/stripping. *Journal of Power Sources*. 2011, 196, S. 2879-2883.
- [82]. **S-T. Myung, Y. Sasaki, S. Sakurada, Y-K. Sun, H. Yashiro.** Electrochemical behavior of current collectors for lithium batteries in non-aqueous alkyl carbonate solution and surface analysis by ToF-SIMS. *Electrochimica Acta*. 2009, 55, S. 288-297.
- [83]. **I. Geoffroy, P. Willmann, K. Mesfar, B. Carrè, D. Lemordant.** Electrolytic characteristics of ethylene carbonate-diglyme-based electrolytes for lithium batteries. *Electrochimica Acta*. 2000, 45, S. 2019-2027.
- [84]. **A. H. Whitehead, M. Schreiber.** Current collectors for positive electrodes of lithium-based batteries. *Journal of The Electrochemical Society*. 2005, Bd. 152, 11, S. A2105-A2113.
- [85]. **Philipp Keil, Matthias Kick, Axel König.** Long-Term Stability, Regeneration and Recycling of Imidazolium-based Ionic Liquids. *Chemie Ingenieur Technik*. 2012, 84, S. 859-866.
- [86]. **Yan Hao, Jing Peng, Shaowen Hu, Jiuqiang Li, Maolin Zhai.** Thermal decomposition of allyl-imidazolium-based ionic liquid studied by TGA-MS analysis and DFT calculations. *Thermochimica Acta*. 2010, 501, S. 78-83.
- [87]. **Niklas Meine, Flavio Benedito, Roberto Rinaldi.** Thermal stability of ionic liquids assessed by potentiometric titration. *Green Chemistry*. 2010, Bd. 12, S. 1711-1714.
- [88]. **Anthony J. Arduengo, Roland Krafczyk.** Auf der Suche nach stabilen Carbenen. *Chemie in unserer Zeit*. 1998, Bd. 32, S. 6-14.
- [89]. **Pierre Bonhôte, Ana-Paula Dias, Nicholas Papageorgiou, Kuppuswamy Kalyanasundaram, Michael Grätzel.** Hydrophobic, Highly Conductive Ambient-Temperature Molten Salts. *Inorganic Chemistry*. 1996, Bd. 35, S. 1168-1178.
- [90]. **Maaïke C. Kroon, Wim Buijs, Cor J. Peters, Geert-Jan Witkamp.** Decomposition of ionic liquids in electrochemical processing. *Green Chemistry*. 2006, Bd. 8, S. 241-245.
- [91]. **Ala`a K. Abdul Sada, Anthony M. Greenway, Kenneth R. Seddon, Thomas Welton.** A Fast Atom Bombardment Mass Spectrometric Study of Room-temperature 1-Ethyl-3-methylimidazolium Chloroaluminate (III) Ionic Liquids. Evidence for the Existence of the Decachlorotrialuminate (III) Anion. *Organic Mass Spectrometry*. 1993, Bd. 28, S. 759-765.

- [92]. **Hajime Ohtani, Shinji Ishimura, Miyuki Kumai.** Thermal Decomposition Behaviors of Imidazolium-type Ionic Liquids Studied by Pyrolysis-Gas Chromatography. *Analytical Sciences*. 2008, 24, S. 1335-1340.
- [93]. **A.A. Fannin, L.A. King, J.A. Levisky, J.S. Wilkes.** Properties of 1,3-dialkylimidazolium chloride-aluminium chloride ionic liquids. 1. ion interactions by nuclear magnetic resonance spectroscopy. *Journal of Physical Chemistry*. 1984, 88, S. 2609-2614.
- [94]. **F. Liebner, I. Patel, G. Ebner, E. Becker, M. Horix, A. Potthast, T. Rosenau.** Thermal aging of 1-alkyl-3-methylimidazolium ionic liquids and its effect on dissolved cellulose. *Holzforschung*. 2010, 64, S. 161-166.
- [95]. **Alberto Sala, Francesco Ferrario, Emanuele Rizzi.** Electron Ionization Mass Spectrometry of some 1- and 2-Alkylimidazoles and 1,3-Dialkylimidazole Iodides. *Rapid Communication in Mass Spectrometry*. 1992, 6, S. 388-393.
- [96]. **M. Ohashi, N. Ohno, H. Kakisawa.** The mass spectra of some alkyl and aryl imidazolines. *Organic Mass Spectrometry*. 1968, 1, S. 703-712.
- [97]. **Arindrajit Chowdhury, Stefan T. Thynell.** Confined rapid thermolysis/FTIR/ToF studies of imidazolium-based ionic liquids. *Thermochimica Acta*. 443, 2006, S. 159-172.
- [98]. **S. Poetz, P. Handel, G. Fauler, B. Fuchsbichler, M. Schmuck, S. Koller.** Evaluation of the decomposition products of EMImCl\*1,5 AlCl<sub>3</sub> during electroplating by different analytical methods. *RSC Advances*. 2014, Bd. 4, 13, S. 6685-6690.
- [99]. International Consulting Bureaux. *International Consulting Bureaux*. [Online] 2002. [Zitat vom: 27.. September 2013.] [http://www.icrjena.de/equip04\\_e.html](http://www.icrjena.de/equip04_e.html).
- [100]. Easy elox. *Easy elox*. [Online] Eloxal Service & more. [Zitat vom: 27.. September 2013.] <http://www.easyelox.de/eloxieren.html>.
- [101]. **Y. Wang, J. Wang, J. Yang, Y. Nuli.** High-rate LiFePO<sub>4</sub> electrode material synthesized by a novel route from FePO<sub>4</sub>\*4H<sub>2</sub>O. *Advanced Functional Materials*. 2006, 16, S. 2135-2140.
- [102]. **K.E. Steube, L.E. McCrary.** Thick ion-vapour-deposited aluminum coatings for irregularly shaped aircraft and spacecraft parts. *J. Vac. Sci. Technol.* 1974, 11, S. 362-365.
- [103]. **J.-G. Zhang, W. Wang, J. Xiao, W. Xu, G.L. Graff, G. Yang, D. Choi, D. Wang, X. Li, J. Liu.** Silicon-based anodes for Li-ion batteries. [Buchverf.] R.J. Brodd. *Batteries for Sustainability: Selected Entries from the Encyclopedia of Sustainability Science and Technology*. New York : Springer Science+Business Media, 2013.
- [104]. **L. Gan, H. Guo, Z. Wang, X. Li, W. Peng, J. Wang, S. Huang, M. Su.** A facile synthesis of graphite/silicon/graphene spherical composite anode for lithium-ion batteries. *Electrochimica Acta*. 2013, 104, S. 117-123.
- [105]. **S. Kovacic, P. Kranjc, C. Slugovc.** Inherently reactive polyHIPE material from dicyclopentadiene. *Chemical Communication*. 2010, 46, S. 7504-7506.

- [106]. **S. Cesca, A. Priola, G. Santi.** The cationic polymerization of "endo"-dicyclopentadiene, 1,2-dihydro-"endo"-dicyclopentadiene and 9,10-dihydro-"endo"-dicyclopentadiene. *Polymer Letters*. 1970, 8, S. 573-584.
- [107]. **S.-Y. Lee, Y.-L. Lai, T.-S. Hsu.** Influence of polymerization conditions on monomer elution and microhardness of autopolymerized polymethyl methacrylate resin. *European Journal of Oral Sciences*. 2002, 110, S. 179-183.
- [108]. **S. Deb, B. Vazquez, W. Bonfield.** Effect of crosslinking agents on acrylic bone cements based on poly(methylmethacrylate). *Journal of Biomedical Materials Research*. 1997, 37, S. 465-473.
- [109]. **T. Chen, R.P. Kusy.** Effect of methacrylic acid: methyl methacrylate monomer ratios on polymerization rates. *Journal of Biomedical Materials Research*. 1997, 36, S. 190-199.
- [110]. **X. Xing, X. Yao, Y. Zhang, Z. Liu, X. Xu.** Si/C nanocomposite anode materials by freeze-drying with enhanced electrochemical performance in lithium-ion batteries. *Journal of Solid State Electrochemistry*. 2012, 16, S. 2733-2738.
- [111]. **Y. Yao, M.T. McDowell, I. Ryu, H. Wu, N. Liu, L. Hu, W.D. Nix, Y. Cui.** Interconnected silicon hollow nanospheres for lithium-ion battery anodes with long cycle life. *Nano Letters*. 2011, 11, S. 2949-2954.
- [112]. **Y.X. Peng, J.L. Liu, L.F. Cun.** Microstructure of polymers obtained by cationic polymerization of endo-dicyclopentadiene. *Journal of Polymer Science: Part A: Polymer Chemistry*. 1996, 34, S. 3527-3530.
- [113]. **Y. Liu, Z.Y. Wen, X.Y. Wang, A. Hirano, N. Imanishi, Y. Takeda.** Electrochemical behaviours of Si/C composite synthesized from F-containing precursors. *Journal of Power Sources*. 2009, 189, S. 733-737.
- [114]. **A. Timmons, A.D.W. Todd, S.D. Mead, G.H. Carey, R.J. Sanderson, R.E. Mar, J.R. Dahn.** Studies of Si<sub>1-x</sub>C<sub>x</sub> electrode materials prepared by high-energy mechanical milling and combinatorial sputter deposition. *Journal of The Electrochemical Society*. 2007, 154, S. A865-A874.
- [115]. **S.Z. Wen, J. Yang, B.F. Wang, K. Wang, Y. Liu.** High capacity silicon/carbon composite anode materials for lithium ion batteries. *Electrochemistry Communications*. 2003, 5, S. 165-168.
- [116]. **X. Zhang, P.K. Patil, C. Wang, A.J. Appleby, F.E. Little, D.L. Cocke.** Electrochemical performance of lithium ion battery, nano-silicon based, disordered carbon composite anodes with different microstructures. *Journal of Power Sources*. 2004, 125, S. 206-213.
- [117]. **C. Zeng, L.J. Lee.** Poly(methyl methacrylate) and polystyrene/clay nanocomposites prepared by in-situ polymerization. *Macromolecules*. 2001, 34, S. 4098-4103.
- [118]. **M. Okamoto, S. Morita, H. Taguchi, Y.H. Kim, T. Kotaka, H. Tateyama.** Synthesis and structure of smectic clay/poly(methyl methacrylate) and clay/polystyrene nanocomposites via in situ intercalative polymerization. *Polymer*. 2000, 41, S. 3887-3890.
- [119]. **Socrates, G.** *Infrared characteristic group frequencies. Tables and charts.* London : WILEY, 1980. 0 471 94230 8.

- [120]. **Jonathan G. Huddleston, Ann E. Visser, W. Matthew Reichert, Heather D. Willauer, Grant A. Broker, Robin D. Rogers.** Characterization and comparison of hydrophilic and hydrophobic room temperature ionic liquids incorporating the imidazolium cation. *Green Chemistry*. 2001, 3, S. 156-164.
- [121]. **Marek Kosmulski, Jan Gustafsson, Jarl B. Rosenholm.** Thermal stability of low temperature ionic liquids revisited. *Thermochimica Acta*. 2004, 412, S. 47-53.
- [122]. **Li Xiao, Keith E. Johnson.** Electrochemistry of 1-Butyl-3-methyl-1H-imidazolium Tetrafluoroborate Ionic Liquid. *Journal of the Electrochemical Society*. 2003, 150, S. E307-E311.
- [123]. **A.G. Advent, P.A. Chaloner, M.P. Day, K.R. Seddon, T. Welton.** Evidence for hydrogen bonding in solutions of 1-ethyl-3-methylimidazolium halides, and its implications for room-temperature halogenaluminates (III) ionic liquids. *Journal of the Chemical Society, Dalton Transactions*. 1994, S. 3405-3413.
- [124]. **Oyama, Satoru.** IHS Electronics & Media. [Online] 15.. August 2011. [Zitat vom: 12.. Juni 2013.] <http://www.isuppli.com/semiconductor-value-chain/news/pages/lithium-ion-battery-market-set-for-boom-courtesy-of-hybrid-and-electric-vehicles.aspx>.
- [125]. Panasonic. [Online] 2013. [Zitat vom: 13.. Juni 2013.] [http://panasonic.net/energy/storage\\_battery/battery-business/index.html](http://panasonic.net/energy/storage_battery/battery-business/index.html).
- [126]. **M. Wohlfahrt-Mehrens, C. Vogler, J. Garche.** Ageing mechanisms of lithium cathode materials. *Journal of Power Sources*. 2004, 127, S. 58-64.
- [127]. **L. Lu, X. Han, J. Li, J. Hua, M. Ouyang.** A review on the key issues for lithium-ion battery management in electric vehicles. *Journal of Power Sources*. 2013, 226, S. 272-288.
- [128]. **L. Barchi, U. Bardi, S. Caporali, M. Fantini, A. Scrivani, A. Scrivani.** Electroplated bright aluminium coatings for anticorrosion and decorative purposes. *Progress in Organic Coatings*. 2010, 67, S. 146-151.
- [129]. **Aldrich, Sigma.** Sigma-Aldrich. *Sigma-Aldrich*. [Online] 2013. [Zitat vom: 09.. October 2013.] <http://www.sigmaaldrich.com/catalog/product/aldrich/445746?lang=de&region=AT>.
- [130]. IHS. *IHS*. [Online] 15.. August 2011. [Zitat vom: 11.. November 2013.] <http://press.ihs.com/press-release/design-supply-chain-media/lithium-ion-battery-market-set-boom-courtesy-hybrid-and-elec>.
- [131]. **Pradhan D., Mantha D., Reddy R.G.** The effect of electrode surface modification and cathode overpotential on deposit characteristics in aluminum electrorefining using EMIC-AlCl<sub>3</sub> ionic liquid electrolyte. *Electrochimica Acta*. 2009, Bd. 54, S. 6661-6667.
- [132]. **Y. Liu, K. Hanai, J. Yang, N. Imanishi, A. Hirano, Y. Takeda.** Silicon/carbon composites as anode materials for li-ion batteries. *Electrochemical and Solid State Letters*. 2004, 7, S. A369-A372.